

# Learning mutational graphs of individual tumour evolution from single-cell and multi-region sequencing data

Daniele Ramazzotti<sup>1</sup>, Alex Graudenzi<sup>\*2,3</sup>, Luca De Sano<sup>2</sup>, Marco Antoniotti<sup>2,4</sup>, and Giulio Caravagna<sup>5</sup>

<sup>1</sup>Department of Pathology, Stanford University, Stanford, CA 94305, USA

<sup>2</sup>Dipartimento di Informatica, Sistemistica e Comunicazione, Università degli Studi di Milano-Bicocca, 20126 Milan, Italy

<sup>3</sup>Institute of Molecular Bioimaging and Physiology of the Italian National Research Council (IBFM-CNR), Viale F.lli Cervi 93, 20090 Segrate, Milan, Italy

<sup>4</sup>Milan Center for Neuroscience, Università degli Studi di Milano-Bicocca, Via Pergolesi 33, 20052 Monza, Italy

<sup>5</sup>Centre for Evolution and Cancer, The Institute of Cancer Research, 15 Cotswold Road, SM2 5NG London, United Kingdom

## Abstract

**Background.** A large number of algorithms is being developed to reconstruct evolutionary models of individual tumours from genome sequencing data. Most methods can analyze multiple samples collected either through bulk multi-region sequencing experiments or the sequencing of individual cancer cells. However, rarely the same method can support both data types.

**Results.** We introduce TRaIT, a computational framework to infer mutational graphs that model the accumulation of multiple types of somatic alterations driving tumour evolution. Compared to other tools, TRaIT supports multi-region and single-cell sequencing data within the same statistical framework, and delivers expressive models that capture many complex evolutionary phenomena. TRaIT improves accuracy, robustness to data-specific errors and computational complexity compared to competing methods.

**Conclusions.** We show that the application of TRaIT to single-cell and multi-region cancer datasets can produce accurate and reliable models of single-tumour evolution, quantify the extent of intra-tumour heterogeneity and generate new testable experimental hypotheses.

## Background

Sequencing data from multiple samples of single tumours can be used to investigate Intra-Tumor Heterogeneity (ITH) in light of evolution [1–3]. Motivated by this observation, several new methods have been developed to infer the “evolutionary history” of a tumour from sequencing data. According to Davis and Navin, there are three orthogonal ways to depict such history [4]: *(i)* with a phylogenetic tree that displays input samples as leaves [5], *(ii)* with a clonal tree of parental relations between putative cancer clones [6–9], and *(iii)* with the order of mutations that accumulated during cancer growth [10–12]. Ideally, the order of accumulating mutations should match the clonal lineage tree in order to reconcile these inferences.

---

\*To whom correspondence should be addressed.

Consistently with earlier works of us [13–18], we here approach the third problem (“mutational ordering”) from two types of data: multi-region bulk and single-cell sequencing.

Bulk sequencing of multiple spatially-separated tumour biopsies returns a noisy mixture of admixed lineages [19–23]. We can analyse these data by first retrieving clonal prevalences in bulk samples (subclonal deconvolution), and then by computing their evolutionary relations [24–31]. Subclonal deconvolution is usually computationally challenging, and can be avoided if we can read genotypes of individual cells via single-cell sequencing (SCS). Despite this theoretical advantage, however, current technical challenges in cell isolation and genome amplification are major bottlenecks to scale SCS to whole-exome or whole-genome assays, and the available targeted data harbours high levels of allelic dropouts, missing data and doublets [32–35]. Thus, the direct application of standard phylogenetic methods to SCS data is not straightforward, despite being theoretically viable [36].

Notice that a common feature of most methods for cancer evolution reconstruction is the employment of the Infinite Sites Assumption (ISA), together with the assumption of no back mutation [24–35], even though recent attempts (e.g., [9]) have been proposed to relax such assumption in order to model relevant phenomena, such as convergent evolutionary trajectories [37].

In this expanding field, we here introduce TRaIT (Temporal oRder of Individual Tumors – Figures 1 and 2), a new framework for the inference of models of single-tumour evolution, which can analyse, separately, multi-region bulk and single-cell sequencing data, and which allows to capture many complex evolutionary phenomena underlying cancer development.

Compared to other approaches that might scale poorly for increasing sample sizes, our methods show excellent computational performance and scalability, rendering them suitable to anticipate the large amount of genomic data that is becoming increasingly available.

## Results

TRaIT is a computational framework that combines Suppes’ probabilistic causation [38] with information theory to infer the temporal ordering of mutations that accumulate during tumour growth, as an extension of our previous work [13–18]. The framework comprises 4 algorithms (EDMONDS, GABOW, CHOW-LIU and PRIM) designed to model different types of progressions (expressivity) and integrate various types of data, still maintaining a low burden of computational complexity (Figures 1 and 2 – see Methods for the algorithmic details).

In TRaIT we estimate the statistical association between a set of genomic events (i.e., mutations, copy number, etc.) annotated in sequencing data by combining optimal graph-based algorithms with bootstrap, hypothesis testing and information theory (Figure 2). TRaIT can reconstruct trees and forests – in general, *mutational graphs* – which in specific cases can include confluences, to account for the uncertainty on the precedence relation among certain events. Forest models (i.e., disconnected trees), in particular, can stem for possible polyclonal tumour initiation (i.e., tumours with multiple cells of origin [39]), or the presence of tumour-triggering events that are not annotated in the input data (e.g., epigenetic events) (Figure 1D).

Inputs data in TRaIT is represent as binary vectors, which is the standard representation for SCS sequencing and is hereby used to define a unique framework for both multi-region bulk and SCS data (Figure 1A–C). For a set of cells or regions sequenced, the input reports the presence/absence of  $n$  genomic events, for which TRaIT will layout a temporal ordering. A binary representation allows to include several types of somatic lesions in the analysis, such as somatic mutations (e.g., single-nucleotide, indels, etc.), copy number alterations, epigenetic states (e.g., methylations, chromatin modifications), etc. (see the Conclusions for a discussion on the issue of data resolution).

## Performance evaluation with synthetic simulations

We assessed the performance of TRaIT with both SCS and multi-region data simulated from different types of generative models.

**Synthetic data generation.** Synthetic single-cell datasets were sampled from a large number of randomly generated topologies (trees or forests) to reflect TRaIT’s generative model. For each generative topology, binary datasets were generated starting from the root, with a recursive procedure which we describe for the simpler case of a tree: (i) for the root node  $x$ , the corresponding variable is assigned 1 with a randomly sampled probability  $p(x = 1) = r$ , with  $r \sim U[0, 1]$ ; (ii) given a branching node  $y$  with children  $y_1, y_2, \dots, y_n$ , we sample values for the  $n$  variables  $y_1, y_2, \dots, y_n$  so that at most one randomly selected child contains 1, and the others are all 0. The recursion proceeds from the root to the leaves, and stops whenever a 0 is sampled or a leaf is reached. Note that we are simulating exclusive branching lineages, as one expects from the accumulation of mutations in single cells under the ISA.

As bulk samples usually include intermixed tumour sub-populations, we simulated bulk datasets by pooling single-cell genotypes generated as described above, and setting simulated variables (i.e., mutations) to 1 (= present) in each bulk sample if they appear in the sampled single-cell genotypes more than a certain threshold. More details on these procedures are reported in Section 2 of the Supplementary Material.

Consistently with previous studies, we also introduced noise in the true genotypes via inflated false positives and false negatives, which are assumed to have highly asymmetric rates for SCS data. For SCS data we also included missing data in a proportion of the simulated variables [11]. Notice that TRaIT can be provided with input noise rates, prior to the inference: therefore, in each reconstruction experiment we provided the algorithm with the noise rates used to generate the datasets, even though mild variations in such input values appear not to affect the inference accuracy – as shown in the noise robustness test presented below and in Figure 3D.

With a total of  $\sim 140,000$  distinct simulations, we could reliably estimate the ability to infer true edges (sensitivity) and discriminate false ones (specificity); further details on parameter settings are available in Section 6 of the Supplementary Material.

In particular, we compared TRaIT’s algorithms to SCITE, the state-of-the-art to infer mutational trees from SCS data [11]. We could not include OncoNEM [7] – the benchmark tool for clonal deconvolution – in the comparison, as its computational performance did not scale well with our large number of tests.

In the Main Text we show results for the Edmonds and Chow-Liu algorithms, included in TRaIT, and SCITE, in a selected number of relevant experimental scenarios. To improve readability of the manuscript, we leave to the Supplementary Material a comprehensive presentation of the results for Gabow, Prim and other approaches [13, 14].

**Results from scenario (i), branching evolution.** To simulate branching evolution [19], we generated a large number of independent datasets from single-rooted tree structures. In particular, we employed three control polyclonal topologies taken from [6] (Supplementary Figure 7) and 100 randomly generated topologies, with a variable number of nodes (i.e., alterations) in the range  $n \in [5; 20]$ . Such generative models were first used to sample datasets with different number of sequenced cells ( $m = 10, 50, 100$ ). In addition to the noise-free setting, we perturbed data by introducing plausible and highly asymmetric noise rates (i.e.,  $\epsilon_+ = \epsilon_- = 0$  (*noise-free*);  $\epsilon_+ = 0.005, \epsilon_- = 0.05$ ;  $\epsilon_+ = 0.02, \epsilon_- = 0.2$ ). The same generative topologies were then used to sample multi-region datasets with different number of regions ( $m = 5, 10, 20$ ), and symmetric noise rates ( $\epsilon_+ = \epsilon_- = 0, 0.05, 0.2$ ).

In Figure 3A we show two selected experimental settings, which are characteristic of the general trends observed on all tests. In particular, one can notice that all the techniques achieve high sensitivity and specificity with SCS data, and significantly lower scores with multi-region

data from the same topology; Edmonds displays in general the best results with SCS data (medians  $\sim 0.8$  and  $\sim 1$ ).

From the results in all simulation settings (Supplementary Figures 8 and 9 for the SCS case; Supplementary Figures 13 and 14 for the multi-region case), we observe that the overall performance significantly improves for lower noise levels and larger datasets across for all the algorithms, a general result that is confirmed in the other experimental scenarios. In particular, with SCS data, Edmonds and SCITE display similar sensitivity, even though the latter presents (on average) lower specificity, which might point to a mild-tendency to overfit. Results on multi-region data display similar trends, with Edmonds showing the overall best performance and SCITE showing slightly lower performance, especially with small datasets and/or low noise levels.

We also specify that, as TRaIT’s algorithms share the same constraints in the search space and several algorithmic properties, the reduced variance observed across settings is expected.

**Results from scenario (ii), confounding factors.** To investigate the impact of possible confounding factors on inference accuracy, we introduced in the datasets from scenario (i) a number of random binary variables totally unrelated to the progression. More in detail, we inserted around  $n \times 10\%$  additional random columns in all datasets with  $n$  input variables; each additional column is a repeated sampling of a biased coin, with bias uniformly sampled among the marginals of all events.

The performance of TRaIT and SCITE in a selected setting for the multi-region case is shown in Figure 3B. Surprisingly, the introduction of confounding factors does not impact the performance significantly. In fact, despite two extra variables annotated in the data that are unrelated to the progression, most algorithms still discriminate the true generative model. Similar results are achieved in the SCS case (Supplementary Figure 10).

**Results from scenario (iii), forest models.** Forest topologies can be employed as generative models of tumours initiated by multiple cells, or of tumours whose initiation is triggered by events that are not annotated in the input data. In this test we randomly generated forests with a variable number of distinct disconnected trees, thus assuming that no mutations are shared across the trees. In detail, we generated 100 random forest topologies, with  $n = 20$  nodes and  $q < 5$  distinct roots (i.e., disconnected trees), both in the SCS and the multi-region case.

The performance of the tested algorithms in a selected experimental scenario with SCS is shown in Figure 3C. All algorithms display a clear decrease in sensitivity, with respect to the single-rooted case with similar values of noise and sample size. In the SCS case the performance remarkably increases with larger datasets (median values  $\sim 0.75$  with  $m = 100$  samples in the noise-free case; Supplementary Figure 11). Edmonds shows the best tradeoff between sensitivity and specificity, whereas SCITE confirms a mild tendency to overfit for small datasets, yet being very robust against noise. Results from multi-region analysis show an overall decrease in performance (Supplementary Figure 16).

**Robustness to variations in noise input values.** Similarly to other tools, e.g., [7,11], our algorithms can receive rates of false positives and negatives in the data ( $\epsilon_+$  and  $\epsilon_-$ ) as input. Thus, we analyzed the effect of miscalled rates on the overall performance. More in detail, we analyzed the variation of the performance of Gabow and SCITE, on a dataset generated from a generative tree with intermediate complexity (“*Medium*” topology in Supplementary Figure 7), with  $n = 11$  nodes and  $m = 75$  samples,  $\epsilon_+ = 5 \times 10^{-3}$  and  $\epsilon_- = 5 \times 10^{-2}$ . We scanned 25 possible combinations of input  $\epsilon_+$  and  $\epsilon_-$  in the following ranges:  $\epsilon_+ = (3, 4, 5, 6, 7) \times 10^{-3}$  and  $\epsilon_- = (3, 4, 5, 6, 7) \times 10^{-2}$ . Results in Figure 3D and Supplementary Tables 4 and 5 show no significant variations of the performance with different combinations of input values for  $\epsilon_+$  and  $\epsilon_-$ , for both algorithms. This proves that the accuracy of the inference is robust to variations in the noise input values, as long as they are reasonably close to the real value. This evidence

also supports our algorithmic design choice which avoids sophisticated noise-learning strategies in TRaIT, a further reason that speeds up computations.

**Missing data.** Significant rates of missing data are still quite common in SCS datasets, mainly due to amplification biases during library preparation. We evaluated the impact of missing data by using 20 benchmark single-cell datasets which were generated from a tree with  $n = 11$  nodes (Supplementary Figure 7). For every dataset we simulated the calling of mutations from  $m = 75$  single sequenced cells, and in half of the cases (i.e., 10 datasets) we also imputed extra error rates in the data to model sequencing errors. In particular, we introduced false positives and false negative calls with rates  $\epsilon_+ = 0.005$  and  $\epsilon_- = 0.05$ . On top of this, for each of the 20 datasets we generated 5 configurations of missing data (uniformly distributed), using as measure the percentage  $r$  of missing data over the total number of observations. A total of 100 distinct datasets have been obtained using  $r = 0, 0.1, 0.2, 0.3, 0.4$  (i.e., up to 40% missing data). As SCITE can explicitly learn parameters from missing data, we run the tool with no further parameters. Instead, for TRaIT’s algorithms, we performed the following procedure: for each dataset  $D$  with missing data, we imputed the missing entries via a standard Expectation-Maximization (EM) algorithm, repeating the procedure to generate 100 complete datasets ( $D_1, \dots, D_{100}$ ). To assess the performance of each algorithm, we computed the fit to all the 100 datasets, and selected the solution that maximised the likelihood of the model.

We present in Figure 4 the results of this analysis for Edmonds and Chow-Liu algorithms included in TRaIT, and for SCITE; results for Gabow and Prim algorithms are presented in Supplementary Figure 12. In general, missing data profoundly affect the performance of all methods. SCITE shows overall more robust sensitivity, in spite of slightly worse specificity. The performance is always significantly improved when data do not harbour noise and, in general, is reasonably robust up to 30% missing data.

**Computational time.** One of the major computational advantages of TRaIT is its scalability, which will be essential in anticipation of the increasingly larger SCS datasets expected in the near future. In this respect, we have observed across all tests a  $3\times$  speedup of TRaIT’s algorithms on standard CPUs with respect to SCITE, and a  $40\times$  speedup with respect to OncoNEM (Supplementary Table 6).

## Analysis of patient-derived multi-region data for a MSI-high colorectal cancer

We applied TRaIT to 47 nonsynonymous point mutations and 11 indels detected via targeted sequencing in patient P3 of [40]. This patient has been diagnosed with a moderately-differentiated MSI-high colorectal cancer, for which 3 samples are collected from the primary tumour (P3-1, P3-2, and P3-3) and two from a right hepatic lobe metastasis L-1 and L-2 (Figure 5A). To prepare the data for our analyses, we first grouped mutations occurring in the same regions. We obtained: (a) a clonal group of 34 mutations detected in all samples (b) a subclonal group of 3 mutations private to the metastatic regions, and (c) 8 mutations with distinct mutational profiles. The clonal group contains mutations in key colorectal driver genes such as APC, KRAS, PIK3CA and TP53 [15],

Edmonds’s model predicts branching evolution and high levels of ITH among the subclonal populations, consistently with the original phylogenetic analysis by Lu et al. [40] (Figure 5B). In particular, the subclonal trajectory that characterizes the primary regions is initiated by a stopgain SNV in the DNA damage repair gene ATM, whereas the subclonal metastatic expansion seems to originate by a stopgain SNV in GNAQ, a gene responsible for diffusion in many tumour types [41]. The model also pictures two distinct trajectories with different mutations in SMAD4: a nonsynonymous SNV in group L, and a stopgain SNV in two regions of the primary.

Interestingly, *SMAD4* regulates cell proliferation, differentiation and apoptosis [42], and its loss is correlated with colorectal metastases [43].

We applied SCITE to the same data (Supplementary Figure S22), and compared it to Edmonds. Both models depict the same history for the metastatic branch, but different tumour initiation: SCITE places the *ATM* mutation on top of the clonal mutations, which appear ordered in a linear chain of 34 events. However, this ordering is uncertain because SCITE’s posterior is multi-modal (i.e., several orderings have the same likelihood; Supplementary Figure 22). Further comments on the results, and outputs from other algorithms are available Supplementary Material (Supplementary Figure 21).

## Analysis of patient-derived SCS data for a triple-negative breast cancer

We applied TRaIT to the triple-negative breast cancer patient TNBC of [34]. The input data consists of single-nucleus exome sequencing of 32 cells: 8 aneuploid (A) cells, 8 hypodiploid (H) cells and 16 normal cells (N) (Figure 6A). Wang et al considered clonal all mutations detected in a control bulk sample and in the majority of the single cells, and as subclonal those undetected in the bulk [34]; all mutations were then used to manually curate a phylogenetic tree (Figure 6B).

We run TRaIT on all single cells, with nonsynonymous point mutations annotated in 22 genes, and set  $\epsilon_+ = 1.24 \times 10^{-6}$  and  $\epsilon_- = 9.73 \times 10^{-2}$  as suggested in [34]. All TRaIT’s algorithms return tree topologies (Supplementary Figures 17–18) ; Figure 6C shows the model obtained with Edmonds. We integrate the analysis by applying SCITE to the same data, and by computing prevalence and evolutionary relations of putative clones with OncoNEM as well (Figure 6D).

TRaIT provides a finer resolution to the original analysis by Wang et al [34], and retrieves gradual accumulation of point mutations thorough tumour evolution, which highlight progressive DNA repair and replication deregulation. The model also predicts high-confidence branching evolution patterns consistent with subclones A<sub>1</sub> (PPP2R1A, SYNE2 and AURKA), A<sub>2</sub> (ECM2, CHRM5 and TGFB2), and H (NRRK1, AFF4, ECM1, CBX4), and provides an explicit ordering among clonal mutations in PTEN, TBX3 and NOTCH2, which trigger tumour initiation. Interestingly, TRaIT also allows to formulate new hypotheses about a possibly undetected subclone with private mutations in JAK1, SETBP1 and CDH6. Finally, we note that that temporal ordering among mutations in ARAF, AKAP9, NOTCH3 and JAK1 cannot be retrieved, since these events have the same marginal probability in these data.

By applying SCITE to these data with the same noise rates, we retrieved 10.000 equivalently optimal trees. The overlap between the first of the returned trees (Supplementary Figure S19) and ours is poor (8 out of 19 edges), and SCITE’s models contain a long linear chain of 13 truncal mutations. Clonal deconvolution analysis via OncoNEM allowed us to detect 10 clones, their lineages and evolutionary relations. This analysis is in stronger agreement with ours, and the estimated mutational ordering obtained by assigning mutations to clones (via maximum a posteriori, as suggested in [7]) largely overlaps with TRaIT’s predictions. This is particularly evident for early events, and for most of the late subclonal ones, exception made for subclone H, which is not detected by OncoNEM. These results prove that concerted application of tools for mutational and clonal trees inference can provide a picture of ITH at an unprecedented resolution.

## Discussion

In this paper we have introduced TRaIT, a computational approach for the inference of cancer evolution models in single tumours. TRaIT’s expressive framework allows to reconstruct models beyond standard trees, such as forests, which capture different modalities of tumour initiation (e.g., by multiple cells of origin, or by events missing in available genomic data, such

as epigenetic states) and, under certain conditions of data and parameters, confluences. Future works will exploit this latter feature to define a comprehensive modelling framework that accounts for explicit violations of the ISA, in order to model further evolutionary phenomena, such as convergent (parallel) evolution and back mutations [37].

TRaIT is based on a binary representation of input data, for both multi-region and single-cell sequencing data. We comment on this design choice concerning the case of multi-region bulk data, because most methods that process bulk data use allelic frequencies and cancer cell fractions to deconvolve the clonal composition of a tumor (see, e.g., [29,30,44]). In this respect, allele frequency-derived inputs provide higher-resolution estimates of the temporal orderings among samples. In fact, if two mutations co-occur in the same set of samples, their relative temporal ordering cannot be determined from a binary input, while this might be possible from their cancer cell fractions. However, despite the lower resolution, a binary representation is still a viable option in multi-region analyses.

First, binary data can describe the presence or absence of a wide range of covariates, which otherwise might be difficult or impossible to represent with allele-frequencies or cancer cell fractions. These include, for instance, complex structural re-arrangements, structural variants, epigenetic modifications, over/under gene expression states and high-level pathway information. The integration of such heterogeneous data types and measurements will be essential to deliver an effective multi-level representation of the life history of individual tumours. Methods that strictly rely on allelic frequencies might need to be extended to accommodate such data types.

Second, binary inputs can be used to promptly analyse targeted sequencing panels, whereas the estimation of subclonal clusters from allele frequencies (i.e., via subclonal deconvolution) requires at least high-depth whole-exome sequencing data to produce reliable results. While it is true that whole-exome and whole-genome assays are becoming increasingly common, many large-scale genomic studies are still relying on targeted sequencing (see, e.g., [45,46]), especially in the clinical setting. A prominent example are assays for longitudinal sampling of circulating tumour DNA during therapy monitoring, which often consist of deep-sequencing target panels derived from the composition of a primary tumour (see, e.g., [47]).

Finally, binary inputs can be obtained for both bulk and single-cell sequencing data, and this in turn allows to use the same framework to study cancer evolution from both data types. This is innovative, and in the future integrative methods might draw inspiration from our approach.

## Conclusions

Intra-tumour heterogeneity is a product of the interplay arising from competition, selection and neutral evolution of cancer subpopulations, and is one of the major causes of drug resistance, therapy failure and relapse [48–52]. For this reason, the choice of the appropriate statistical approach to take full advantage of the increasing resolution of genomic data is key to produce predictive models of tumour evolution with translational relevance.

We have here introduced TRaIT, a framework for the efficient reconstruction of single tumour evolution from multiple-sample sequencing data. Thanks to the simplicity of the underlying theoretical framework, TRaIT displays significant advancements in terms of robustness, expressivity, data integration and computational complexity. TRaIT can process both multi-region and SCS data (separately), and its optimal algorithms maintain a low computational burden compare to alternative tools. TRaIT’s assumptions to model accumulation phenomena lead to accurate and robust estimate of temporal orderings, also in presence of noisy data.

We position TRaIT in a very precise niche in the landscape of tools for cancer evolution reconstruction, i.e., that of methods for the inference of mutational trees/graphs (not clonal or phylogenetic trees), from binary data (alteration present/absent), and supporting both multi-region bulk and single-cell sequencing data. We advocate the use of TRaIT as complementary to tools for clonal tree inference, in a joint effort to quantify the extent of ITH, as shown in the case study on triple negative breast cancer.

# Methods

## Input Data and Data Types

TRaIT processes an input binary matrix  $D$  with  $n$  columns and  $m$  rows.  $D$  stores  $n$  binary variables (somatic mutations, CNAs, epigenetic states, etc.) detected across  $m$  samples (single cells or multi-region samples) (Figure 2A). One can annotate data at different resolutions: for instance, one can distinguish mutations by type (missense vs truncating), position, or context (G>T vs G>A), or can just annotate a general “mutation” status. The same applies for copy numbers, which can be annotated at the focal, cytoband or arm-level. In general, if an entry in  $D$  is 1, then the associated variable is detected in the sample.

In our framework we cannot disentangle the temporal ordering between events that occur in the same set of samples. These will be grouped by TRaIT in a new “aggregate” node, prior to the inference (Figure 2B). TRaIT does not explicitly account for back mutations due to loss of heterozygosity. Yet, the information on these events can be used to prepare input data if one matches the copy number state to the presence of mutations. By merging these events we can retrieve their temporal position in the output graph (Supplementary Figure S23).

TRaIT supports both multi-region and SCS data. As we expect  $D$  to contain noisy observations of the unknown true genotypes, the algorithms can be informed of false positives and negatives rates ( $\epsilon_+ \geq 0$  and  $\epsilon_- \geq 0$ ). TRaIT does not implement noise learning strategies, similarly to OncoNEM [11]. This choice is sensitive if the algorithms show stable performance for slight variations in the input noise rates, especially when reasonable estimates of  $\epsilon_+$  and  $\epsilon_-$  can be known a priori. This feature allows TRaIT to be computationally more efficient, as it avoids to include a noise learning routine in the fit. Missing data, instead, are handled by a standard Expectation Maximisation approach to impute missing values: for every complete dataset obtained, the fit is repeated and the model that maximises the likelihood across all runs is returned.

## TRaIT’s Procedure

All TRaIT’s algorithms can be summarised with a three-steps skeleton, where the first two steps are the same across all algorithms. Each algorithm will return a unique output model, whose post hoc confidence can be assessed via cross-validation and bootstrap [15].

### Step 1: assessment of statistical association – Figure 2C

We estimate the statistical association between events by assessing two conditions inspired to Suppes’ theory of probabilistic causation, which is particularly sound in modelling cumulative phenomena [38].

Let  $p(\cdot)$  be an empirical probability (marginal, joint, conditional etc.) estimated from dataset  $D$ . Conditions on (i) temporal direction and (ii) association’s strength are assessed as follows: for every pair of variables  $x$  and  $y$  in  $D$ ,  $x$  is a plausible temporally antecedent event of  $y$  if

$$p(x) > p(y) \quad \wedge \quad p(y | x) > p(y | \neg x). \quad (1)$$

The former condition acts as the Infinite Sites Assumption (ISA), as we assume that alterations are inherited across cell divisions (i.e., somatic): thus, the comparison of marginal frequencies is a proxy to compute the relative ordering among events. The latter condition, instead, implies statistical dependence:  $p(x, y) > p(x)p(y)$  [13].

Both conditions are assessed among all variables pairs via non-parametric bootstrap and a one-tailed Mann-Whitney test: only if both conditions are statistically significant at some



$\alpha$ -level (e.g., 0.05), the edge connecting the variable pair will be included in a prima-facie direct graph  $G_{\text{pf}}$ . Edges in  $G_{\text{pf}}$  are candidate to be selected in the final output model, and thus we are reducing the search space via the the above conditions, which are necessary but not sufficient. These conditions have been previously used to define causal approaches for cancer progression [14, 15]; see further discussion in Supplementary Material. This step has asymptotic complexity  $\mathcal{O}((nm)^2 \times B)$  where  $B$  is the cost of bootstrap and hypothesis testing on each entry in  $D$ . Notice that this procedure can create disconnected components.

### Step 2: loop removal – Figure 2D

$G_{\text{PF}}$  can contain loops, which we have to remove to model an accumulation process. Loops may arise when an arc between a pair of nodes cannot be unequivocally directed, e.g., due to small sample size which leads to uncertain bootstrap estimations. TRaIT renders acyclic  $G_{\text{PF}}$  by using heuristic strategies that remove less confident edges (see [14]); the output produced is a new graph  $G_{\text{NL}}$ .

### Step 3: reconstruction of the output model – Figure 2E–F

We render  $G_{\text{NL}}$  a weighted graph by annotating its edges via information-theoretic measures such as point-wise mutual information and the like. Then, we can exploit 4 different off-the-shelf algorithms to reconstruct an output model  $G_{\text{MO}}$  from  $G_{\text{NL}}$ .  $G_{\text{MO}}$  will be either a tree or a forest with multiple roots, and the complexity of this step depends on the adopted algorithm. Notably, all algorithms currently incorporated in TRaIT have theoretically-optimal worst-case polynomial complexity. We describe two of them (Edmonds and Chow-Liu), and leave the description of the other techniques (Gabow and Prim) to the Supplementary Material.

- Edmonds is an algorithm for the inference of weighted directed minimum spanning trees [53]: it scan  $G_{\text{NL}}$  to identify the tree that maximises the edges' weights. Spanning trees have been previously applied to cancer [54, 55]. Yet, TRaIT is the only framework to constraint spanning trees by condition (1);
- Chow-Liu's algorithm is a method to compute a factorisation of a joint distribution over the input variables [56]. Chow-Liu reconstructs undirected trees by definition; we assign the direction to each edge so that the event with higher marginal probability is on top, mirroring condition (1). Confluences in  $G_{\text{MO}}$  can emerge under certain conditions of the observed probabilities, which account for the uncertainty on the temporal precedence among events (technically, in such cases we reconstruct direct acyclic graphs, DAGs – see the Supplementary Material for details).

In all TRaIT's algorithms, if  $G_{\text{NL}}$  includes  $k$  disconnected components, then the output model  $G_{\text{MO}}$  will include  $k$  disconnected trees .

In term of complexity, we note that all TRaIT's algorithms are optimal polynomial-time algorithmic solutions to each of their corresponding combinatorial problems. Thus, they scale well with sample size, a problem sometimes observed with Bayesian approaches that cannot compute a full posterior on the model parameters. Quantitative assessment of TRaIT's scalability with large datasets is provided as Supplementary Material (Supplementary Table 7), where we show that many thousands of cells can be processed in a few seconds.

## Tumour evolution scenarios

TRaIT can infer mutational graphs in the following scenarios (see Figure 1D):

1. Branching evolution (including linear evolution as subcase): in this case TRaIT will return a tree with one root and zero disconnected components.
2. Presence of confounding factors in  $D$  (e.g., miscalled mutations): TRaIT will reconstruct a model with disconnected individual nodes.

3. Polyclonal origin due to multiple cells of tumour origin, or to upstream events triggering tumour development that missing in  $D$  (e.g., epigenetic events): TRaIT will return models with disconnected components (i.e., forests).

In general, we recommend to apply all TRaIT's algorithms and to compare the output models; the creation of a consensus model is an option to rank the edges detected across several methods, as we show in the case studies.

## Abbreviations

CNA: Copy-Number Alteration  
CT: Clonal Tree  
ISA: Infinite Sites Assumption  
ITH: Intra-Tumour Heterogeneity  
MSI: Micro-Satellite Instable  
SCS: Single-Cell Sequencing  
SNV: Single-Nucleotide Variant

## Availability of data and materials

TRaIT is included in the TRONCO R suite for TRanslational ONCOlogy, available at its webpage <http://troncopackage.org> and mirrored at Bioconductor. All data used in this paper are available from the supplementary material of [34] and [40]. We provide the source code and the input data to reproduce the case studies at: BIMIB-DISCo/TRaIT.

## Competing interests

The authors declare that they have no competing interests.

## Funding

This work was partially supported by the Elixir Italian Chapter and the SysBioNet project, a Ministero dell'Istruzione, dell'Università e della Ricerca initiative for the Italian Roadmap of European Strategy Forum on Research Infrastructures.

The funding body did not play any role in the design of the study and collection, analysis, and interpretation of data and in writing the manuscript.

## Author's contributions

DR, AG and GC designed the algorithmic framework. DR, LDS and GC implemented the tool. LDS carried out the simulations on synthetic data. Data gathering was performed by DR, AG, LDS and GC. All the authors analyzed the results and interpreted the models. DR, AG, MA and GC wrote the draft of the paper, which all authors reviewed and revised.

## Acknowledgements

We thank Bud Mishra for valuable insights on the effects of parallel evolution to our framework. We also thank Guido Sanguinetti and Yuanhua Huang for useful discussions on the preliminary version of this manuscript.

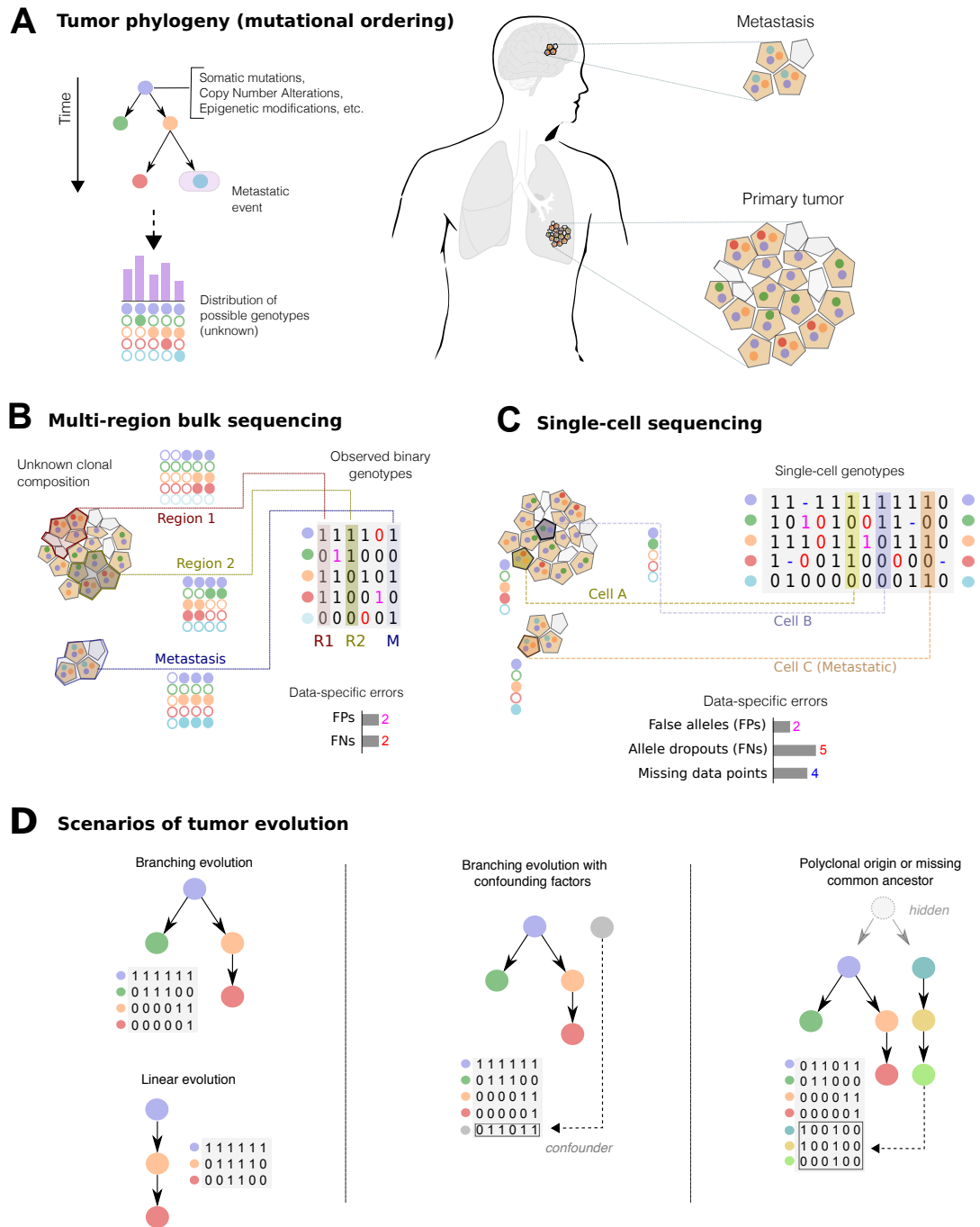


Figure 1: **A.** A tumour phylogeny describes the order of accumulation of somatic mutations, CNAs, epigenetic modifications, etc. in a single tumour. The model generates a set of possible genotypes, which are observed with an unknown spatial and density distribution in a tumour (primary and metastases). **B.** Multi-region bulk sequencing returns a mixed signal from different tumour subpopulations, with potential contamination of non-tumour cells (not shown) and symmetric rates of false positives and negatives in the calling. Thus, a sample will harbour lesions from different tumour lineages, creating spurious correlations in the data. **C.** If we sequence genomes of single cells we can, in principle, have a precise signal from each subpopulation. However, the inference with these data is made harder by high levels of asymmetric noise, errors in the calling and missing data. **D.** Different scenarios of tumour evolution can be investigated via TRaIT. (i) Branching evolution (which includes linear evolution), (ii) Branching evolution with confounding factors annotated in the data, (iii) Models with multiple progressions due to polyclonal tumour origination, or to the presence tumour initiating event missing from input data .

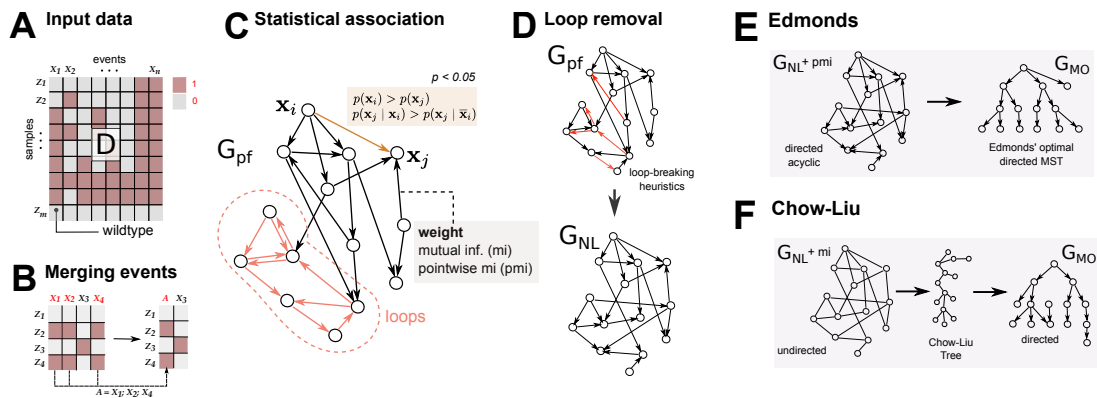


Figure 2: **A.** TRaIT processes a binary matrix  $D$  that stores the presence or absence of a variable in a sample (e.g., a mutation, a CNA, or a persistent epigenetic states). **B.** TRaIT merges the events occurring in the same samples ( $\mathbf{x}_1$ ,  $\mathbf{x}_2$  and  $\mathbf{x}_4$ , merged to  $A$ ), as the statistical signal for their temporal ordering is undistinguishable. The final model include such aggregate events. **C.** We estimate via bootstrap the *prima facie* ordering relation that satisfies Suppes' conditions (1) for statistical association. This induces a graph  $G_{PF}$  over variables  $\mathbf{x}_i$ , which is weighted by information-theoretic measures for variables' association such as mutual information or pointwise mutual information. **D.** TRaIT employs heuristic strategies to remove loops from  $G_{PF}$  and produce a new graph  $G_{NL}$  [14]. **E.** Edmonds's algorithm can be used to reconstruct the optimal minimum spanning tree  $G_{MO}$  that minimises the weights in  $G_{NL}$ ; here we use point-wise mutual information (pmi). **F.** Chow-Liu is a Bayesian mode-selection strategy that computes an undirected tree as a model of a joint distribution on the annotated variable. Then, we provide edge direction (temporal priority), with Suppes' condition (1) on marginal probabilities. Therefore, confluences are possible in the output model  $G_{MO}$  in certain conditions

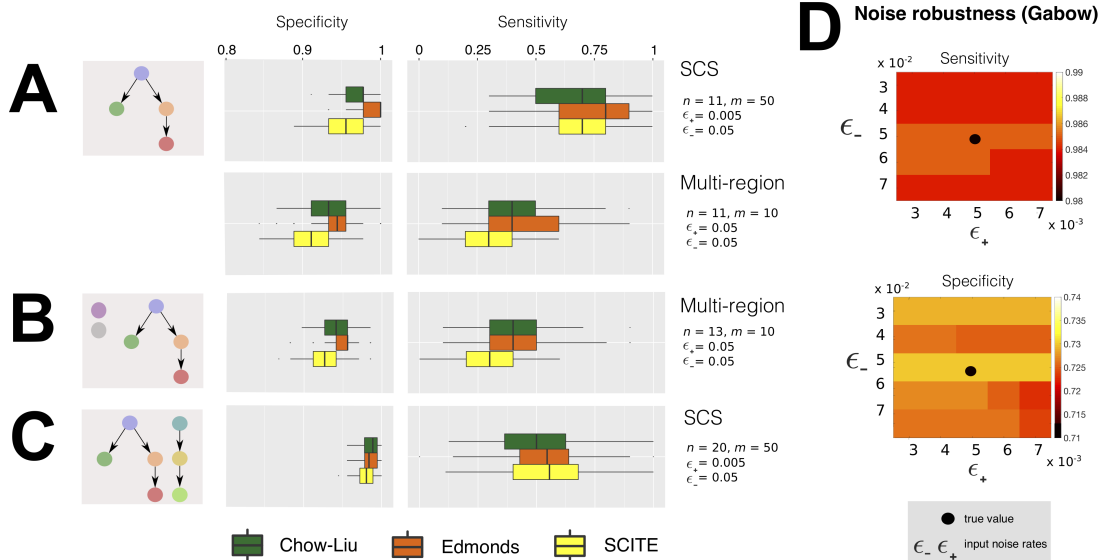


Figure 3: We estimate from simulations the rate of detection of true positives (sensitivity) and negatives (specificity), visualised as *box-plots* from 100 independent points each. We compare TRaIT’s algorithms Edmonds and Chow-Liu with SCITE, the state-of-the-art for mutational trees inference in a setting of mild noise in the data, and canonical sample size. In SCS data noise is  $\epsilon_+ = 5 \times 10^{-3}$ ;  $\epsilon_- = 5 \times 10^{-2}$ , in multi-region  $\epsilon_- = 5 \times 10^{-2}$ . Extensive results for different models, data type, noise and sample size are in Supplementary Figures S3–S16. **A**. Here we use a generative model from [6] (Supplementary Figure S7-B). (left) SCS datasets with  $m = 50$  single cells, for a tumour with  $n = 11$  mutations. (right) Multi-region datasets with  $m = 10$  spatially separated regions, for a tumour with  $n = 11$  mutations. **B**. We augment the setting in A-right with 2 random variables (with random marginal probability) to model confounding factors, and generated SCS data. **C**. We generated multi-region data from a tumour with  $n = 21$  mutations, and a random number of 2 or 3 distinct cells of origin to model polyclonal tumour origination. **D**. Spectrum of average sensitivity and specificity for Gabow algorithm included in TRaIT (see SM) estimated from 100 independent SCS datasets sampled from the generative model in Supplementary Figure S7-B ( $m = 75, n = 11$ ). The true noise rates are  $\epsilon_+ = 5 \times 10^{-3}$ ;  $\epsilon_- = 5 \times 10^{-2}$ ; we scan input  $\epsilon_+$  and  $\epsilon_-$  in the ranges:  $\epsilon_+ = (3, 4, 5, 6, 7) \times 10^{-3}$  and  $3 \times 10^{-2} \leq \epsilon_- \leq 7 \times 10^{-2}$ .

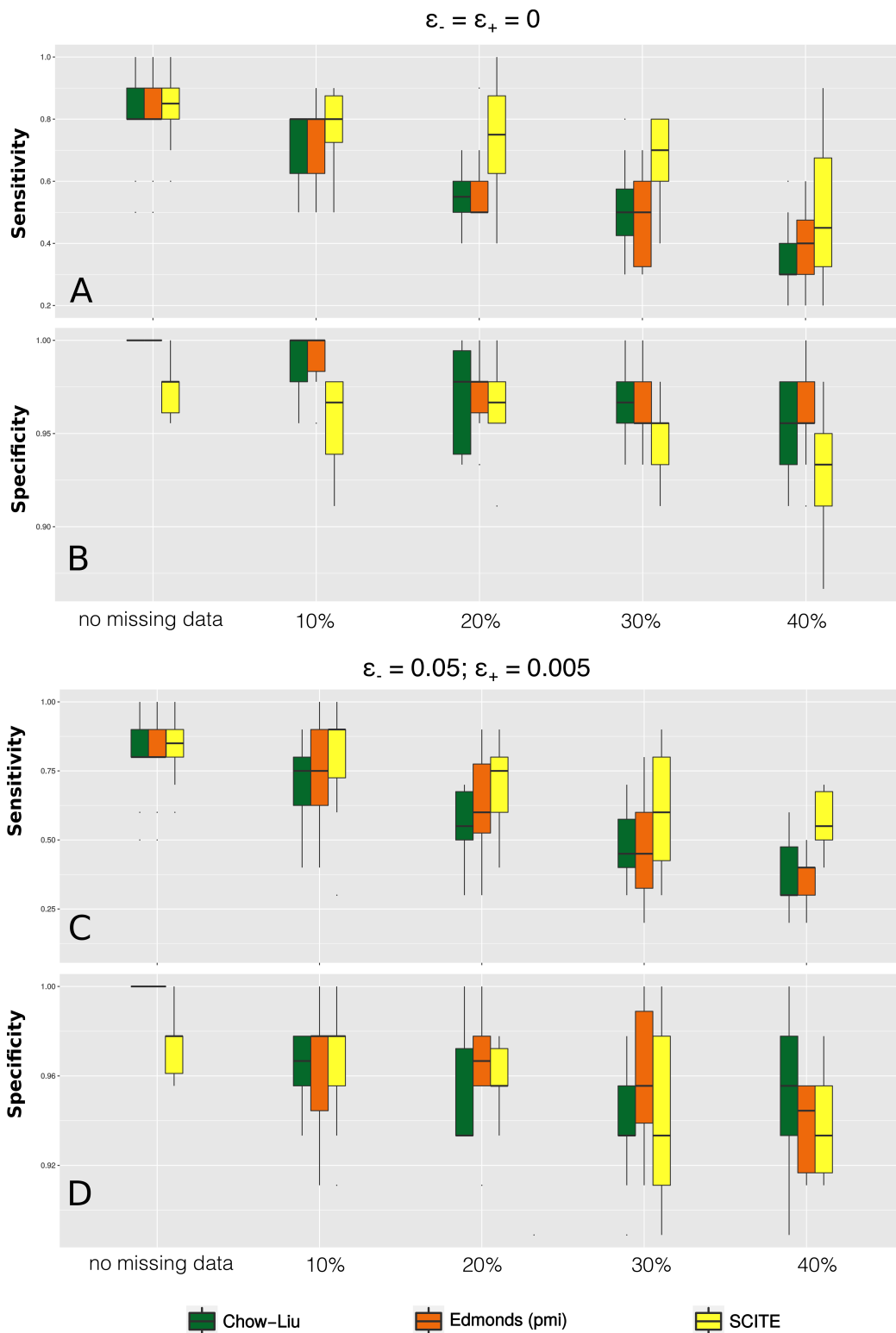
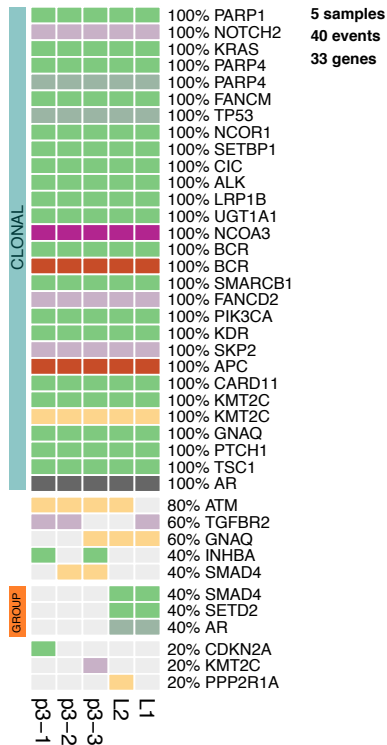


Figure 4: Sensitivity and specificity for different percentages  $r$  of missing entries, namely,  $r = (0, 0.1, 0.2, 0.3, 0.4)$  as a function of the number of variables in the data, and different levels of noise: (i)  $\epsilon_+ = \epsilon_- = 0$  and (ii)  $\epsilon_+ = 0.005$ ,  $\epsilon_- = 0.05$ . The original dataset is generated from a tree with  $n = 11$  nodes and  $m = 75$  samples (Supplementary Figure 7).

## A Colorectal cancer Multi-region P3 (Lu et al.)



### Mutations



## B TRaIT's model (Edmonds)

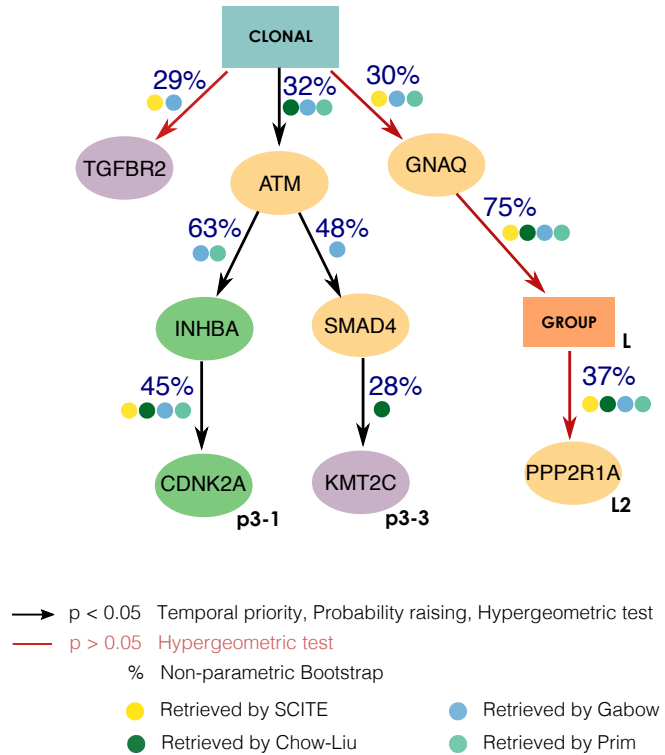


Figure 5: **A**. Multi-region sequencing data for a MSI-high colorectal cancer from [40], with three regions of the primary cancer: p3-1, p3-2 and p3-3, and two of one metastasis: L-1 and L-2. To use this data with TRaIT we merge mutations occur in the same samples, obtaining a clonal group of 34 mutations and a subclonal group. **B**. The model obtained by Edmonds including confidence measures, and the overlap in the predicted ordering obtained by SCITE, Chow-Liu, Gabow and Prim (Supplementary Figure S21). All edges, in all models, are statistically significant for conditions (1). Four of the predicted ordering relations are consistently found across all TRaIT's algorithm, which gives a high-confidence explanation for the formation of the L2 metastasis. This finding is also in agreement with predictions by SCITE (Supplementary Figure S22).

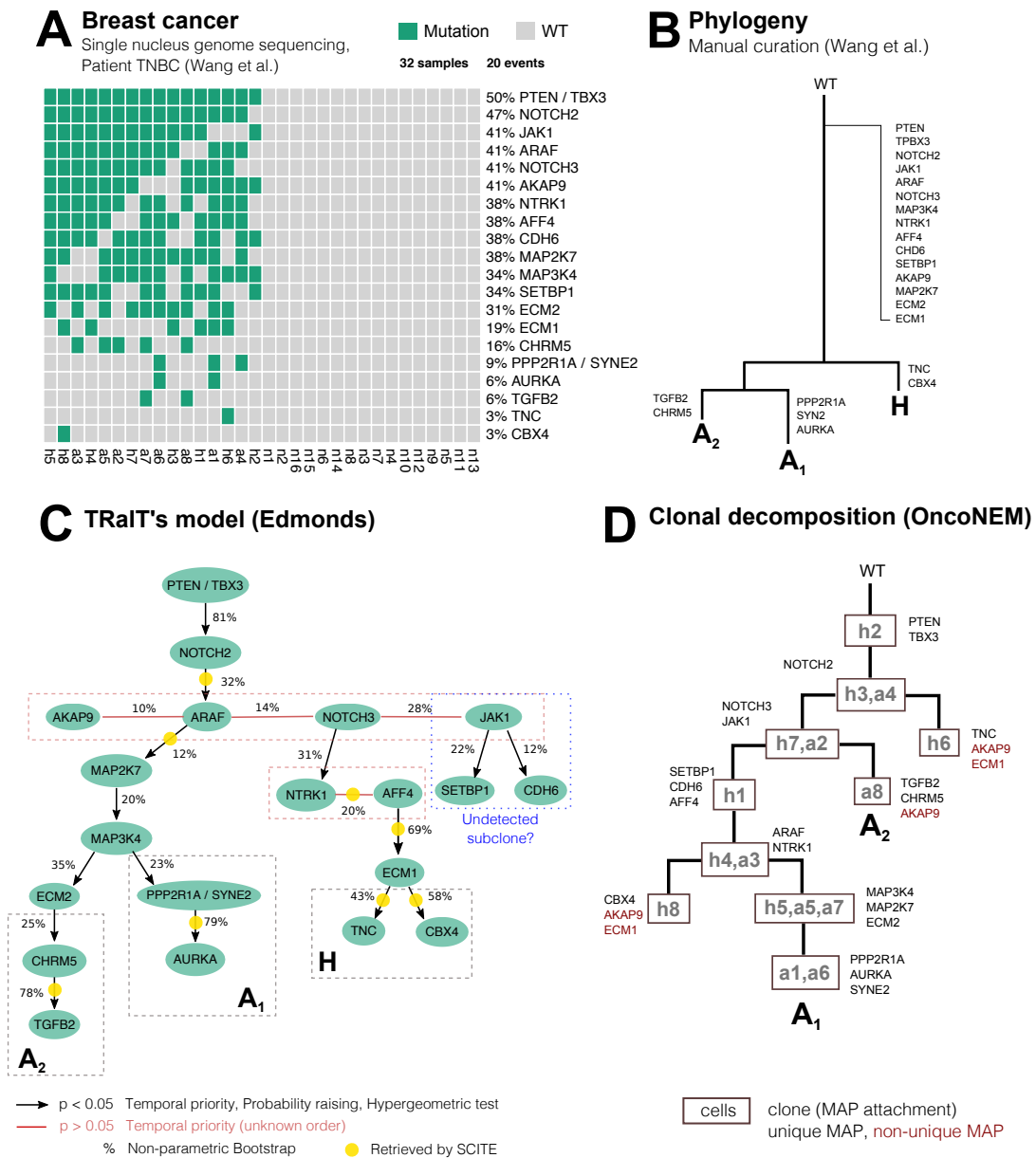


Figure 6: **A.** Input data from single-nucleus sequencing of 32 cells from a triple-negative breast cancer [34]. As the rate of missing values in the original data was around 1%, the authors set all missing data points equal to 0; in the dataset, allelic dropout is equal to  $9.73 \times 10^{-2}$ , and false discovery equal to  $1.24 \times 10^{-6}$ . **B** Phylogenetic tree manually curated in [34]. Mutations are annotated to the trunk if they are ubiquitous across cells and a bulk control sample. Subclonal mutations appearing only in more than one cell. **C.** Mutational graph obtained with Edmonds algorithm;  $p$ -values are obtained by 3 tests for conditions (1) and overlap (hypergeometric test), and edges annotated with a posteriori non-parametric bootstrap scores (100 estimates). For these data, all TRaIT's algorithms return trees (Supplementary Figure S17-18), consistently with the manually curated phylogeny (A). Most edges are highly confident ( $p < 0.05$ ), except for groups of variables with the same frequency which have unknown ordering (red edges). The ordering of mutations in subclones  $A_1$ ,  $A_2$  and tumour initiation has high bootstrap estimates ( $> 75\%$ ). Yellow circles mark the edges retrieved also by SCITE. **D.** We also performed clonal tree inference with OncoNEM, which predicts 10 clones. Mutations are assigned to clones via *maximum a posteriori* estimates. The mutational orderings of the early clonal expansion of the tumour and of most of the late subclonal events are consistent with TRaIT's prediction.



## References

- [1] Niko Beerenwinkel, Roland F Schwarz, Moritz Gerstung, and Florian Markowetz. Cancer evolution: mathematical models and computational inference. *Systematic biology*, 64(1):e1–e25, 2015.
- [2] Russell Schwartz and Alejandro A Schäffer. The evolution of tumour phylogenetics: principles and practice. *Nature Reviews Genetics*, 2017.
- [3] Giulio Caravagna, Ylenia Giarratano, Daniele Ramazzotti, Ian Tomlinson, Trevor A. Graham, Guido Sanguinetti, and Andrea Sottoriva. Detecting repeated cancer evolution from multi-region tumor sequencing data. *Nature Methods*, 15(9):707–714, 2018.
- [4] Alexander Davis and Nicholas E Navin. Computing tumor trees from single cells. *Genome biology*, 17(1):113, 2016.
- [5] Alexandros Stamatakis. Raxml version 8: a tool for phylogenetic analysis and post-analysis of large phylogenies. *Bioinformatics*, 30(9):1312–1313, 2014.
- [6] Ke Yuan, Thomas Sakoparnig, Florian Markowetz, and Niko Beerenwinkel. BitPhylogeny: a probabilistic framework for reconstructing intra-tumor phylogenies. *Genome biology*, 16(1):1, 2015.
- [7] Edith M Ross and Florian Markowetz. OncoNEM: inferring tumor evolution from single-cell sequencing data. *Genome biology*, 17(1):1, 2016.
- [8] Andrew Roth, Andrew McPherson, Emma Laks, Justina Biele, Damian Yap, Adrian Wan, Maia A Smith, Cydney B Nielsen, Jessica N McAlpine, Samuel Aparicio, Alexandre Bouchard-Côté, and Sohrab P Shah. Clonal genotype and population structure inference from single-cell tumor sequencing. *Nature methods*, 13(7):573–576, 2016.
- [9] Hamim Zafar, Anthony Tzen, Nicholas Navin, Ken Chen, and Luay Nakhleh. SiFit: inferring tumor trees from single-cell sequencing data under finite-sites models. *Genome Biology*, 18(1):178, 2017.
- [10] Kyung In Kim and Richard Simon. Using single cell sequencing data to model the evolutionary history of a tumor. *BMC bioinformatics*, 15(1):27, 2014.
- [11] Katharina Jahn, Jack Kuipers, and Niko Beerenwinkel. Tree inference for single-cell data. *Genome biology*, 17(1):1, 2016.
- [12] Sohrab Salehi, Adi Steif, Andrew Roth, Samuel Aparicio, Alexandre Bouchard-Côté, and Sohrab P Shah. ddClone: joint statistical inference of clonal populations from single cell and bulk tumour sequencing data. *Genome Biology*, 18(1):44, 2017.
- [13] Loes Olde Loohuis, Giulio Caravagna, Alex Graudenzi, Daniele Ramazzotti, Giancarlo Mauri, Marco Antoniotti, and Bud Mishra. Inferring tree causal models of cancer progression with probability raising. *PloS one*, 9(10):e108358, 2014.
- [14] Daniele Ramazzotti, Giulio Caravagna, Loes Olde Loohuis, Alex Graudenzi, Ilya Korsunsky, Giancarlo Mauri, Marco Antoniotti, and Bud Mishra. CAPRI: efficient inference of cancer progression models from cross-sectional data. *Bioinformatics*, 31(18):3016–3026, 2015.
- [15] G. Caravagna, A. Graudenzi, D. Ramazzotti, R. Sanz-Pamplona, L. De Sano, G. Mauri, V. Moreno, M. Antoniotti, and B. Mishra. Algorithmic methods to infer the evolutionary trajectories in cancer progression. *Proceedings of the National Academy of Sciences*, 113(28):E4025–E4034, 2016.

- [16] Daniele Ramazzotti. *A Model of Selective Advantage for the Efficient Inference of Cancer Clonal Evolution*. PhD thesis, Università degli Studi di Milano-Bicocca, 2017. arXiv preprint arXiv:1602.07614.
- [17] Daniele Ramazzotti, Marco S Nobile, Paolo Cazzaniga, Giancarlo Mauri, and Marco Antoniotti. Parallel implementation of efficient search schemes for the inference of cancer progression models. In *Computational Intelligence in Bioinformatics and Computational Biology (CIBCB), 2016 IEEE Conference on*, pages 1–6. IEEE, 2016.
- [18] Daniele Ramazzotti, Alex Graudenzi, Giulio Caravagna, and Marco Antoniotti. Modeling cumulative biological phenomena with suppes-bayes causal networks. *Evolutionary Bioinformatics*, 14:1176934318785167, 2018.
- [19] Marco Gerlinger, Andrew J Rowan, Stuart Horswell, James Larkin, David Endesfelder, Eva Gronroos, Pierre Martinez, Nicholas Matthews, Aengus Stewart, Patrick Tarpey, et al. Intratumor heterogeneity and branched evolution revealed by multiregion sequencing. *New England journal of medicine*, 366(10):883–892, 2012.
- [20] Elza C de Bruin, Nicholas McGranahan, Richard Mitter, Max Salm, David C Wedge, Lucy Yates, Mariam Jamal-Hanjani, Seema Shafi, Nirupa Murugaesu, Andrew J Rowan, et al. Spatial and temporal diversity in genomic instability processes defines lung cancer evolution. *Science*, 346(6206):251–256, 2014.
- [21] Jianjun Zhang, Junya Fujimoto, Jianhua Zhang, David C Wedge, Xingzhi Song, Jiexin Zhang, Sahil Seth, Chi-Wan Chow, Yu Cao, Curtis Gumbs, et al. Intratumor heterogeneity in localized lung adenocarcinomas delineated by multiregion sequencing. *Science*, 346(6206):256–259, 2014.
- [22] Lucy R Yates, Moritz Gerstung, Stian Knappskog, Christine Desmedt, Gunes Gundem, Peter Van Loo, Turid Aas, Ludmil B Alexandrov, Denis Larsimont, Helen Davies, et al. Subclonal diversification of primary breast cancer revealed by multiregion sequencing. *Nature medicine*, 21(7):751–759, 2015.
- [23] Mariam Jamal-Hanjani, Gareth A Wilson, Nicholas McGranahan, Nicolai J Birkbak, Thomas BK Watkins, Selvaraju Veeriah, Seema Shafi, Diana H Johnson, Richard Mitter, Rachel Rosenthal, et al. Tracking the evolution of non-small-cell lung cancer. *New England Journal of Medicine*, 376(22):2109–2121, 2017.
- [24] Layla Oesper, Ahmad Mahmoody, and Benjamin J Raphael. Inferring intra-tumor heterogeneity from high-throughput dna sequencing data. In *Annual International Conference on Research in Computational Molecular Biology*, pages 171–172. Springer, 2013.
- [25] Francesco Strino, Fabio Parisi, Mariann Micsinai, and Yuval Kluger. TrAp: a tree approach for fingerprinting subclonal tumor composition. *Nucleic acids research*, 41(17):e165–e165, 2013.
- [26] Andrew Roth, Jaswinder Khattra, Damian Yap, Adrian Wan, Emma Laks, Justina Biele, Gavin Ha, Samuel Aparicio, Alexandre Bouchard-Côté, and Sohrab P Shah. PyClone: statistical inference of clonal population structure in cancer. *Nature methods*, 11(4):396–398, 2014.
- [27] Wei Jiao, Shankar Vembu, Amit G Deshwar, Lincoln Stein, and Quaid Morris. Inferring clonal evolution of tumors from single nucleotide somatic mutations. *BMC bioinformatics*, 15(1):1, 2014.
- [28] Habil Zare, Junfeng Wang, Alex Hu, Kris Weber, Josh Smith, Debbie Nickerson, ChaoZhong Song, Daniela Witten, C Anthony Blau, and William Stafford Noble. Inferring clonal composition from multiple sections of a breast cancer. *PLoS Comput Biol*, 10(7):e1003703, 2014.

- [29] Amit G Deshwar, Shankar Vembu, Christina K Yung, Gun Ho Jang, Lincoln Stein, and Quaid Morris. PhyloWGS: reconstructing subclonal composition and evolution from whole-genome sequencing of tumors. *Genome biology*, 16(1):1, 2015.
- [30] Mohammed El-Kebir, Gryte Satas, Layla Oesper, and Benjamin J Raphael. Inferring the mutational history of a tumor using multi-state perfect phylogeny mixtures. *Cell Systems*, 3(1):43–53, 2016.
- [31] Zheng Hu and Christina Curtis. Inferring Tumor Phylogenies from Multi-region Sequencing. *Cell systems*, 3(1):12–14, 2016.
- [32] Nicholas Navin, Jude Kendall, Jennifer Troge, Peter Andrews, Linda Rodgers, Jeanne McIndoo, Kerry Cook, Asya Stepansky, Dan Levy, Diane Esposito, et al. Tumour evolution inferred by single-cell sequencing. *Nature*, 472(7341):90–94, 2011.
- [33] Charles Gawad, Winston Koh, and Stephen R Quake. Dissecting the clonal origins of childhood acute lymphoblastic leukemia by single-cell genomics. *Proceedings of the National Academy of Sciences*, 111(50):17947–17952, 2014.
- [34] Yong Wang, Jill Waters, Marco L Leung, Anna Unruh, Whijae Roh, Xiuqing Shi, Ken Chen, Paul Scheet, Selina Vattathil, Han Liang, et al. Clonal evolution in breast cancer revealed by single nucleus genome sequencing. *Nature*, 512(7513):155–160, 2014.
- [35] Nicholas E Navin. The first five years of single-cell cancer genomics and beyond. *Genome research*, 25(10):1499–1507, 2015.
- [36] Roland F Schwarz, Anne Trinh, Botond Sipos, James D Brenton, Nick Goldman, and Florian Markowetz. Phylogenetic quantification of intra-tumour heterogeneity. *PLoS computational biology*, 10(4):e1003535, 2014.
- [37] Nicholas E Navin and Ken Chen. Genotyping tumor clones from single-cell data. *Nature Methods*, 13(7):555–556, 2016.
- [38] Patrick Suppes. *A probabilistic theory of causality*. North-Holland Publishing Company Amsterdam, The Netherlands, 1970.
- [39] Barbara L Parsons. Many different tumor types have polyclonal tumor origin: evidence and implications. *Mutation Research/Reviews in Mutation Research*, 659(3):232–247, 2008.
- [40] You-Wang Lu, Hui-Feng Zhang, Rui Liang, Zhen-Rong Xie, Hua-You Luo, Yu-Jian Zeng, Yu Xu, La-Mei Wang, Xiang-Yang Kong, and Kun-Hua Wang. Colorectal cancer genetic heterogeneity delineated by multi-region sequencing. *PloS one*, 11(3):e0152673, 2016.
- [41] Chung-Young Kim, Dae Won Kim, Kevin Kim, Jonathan Curry, Carlos Torres-Cabala, and Sapna Patel. GNAQ mutation in a patient with metastatic mucosal melanoma. *BMC cancer*, 14(1):516, 2014.
- [42] Hafid Alazzouzi, Pia Alhopuro, Reijo Salovaara, Heli Sammalkorpi, Heikki Järvinen, Jukka-Pekka Mecklin, Akeseli Hemminki, Simo Schwartz, Lauri A Aaltonen, and Diego Arango. SMAD4 as a prognostic marker in colorectal cancer. *Clinical Cancer Research*, 11(7):2606–2611, 2005.
- [43] Xuemei Li, Baoquan Liu, Jianbing Xiao, Ying Yuan, Jing Ma, and Yafang Zhang. Roles of VEGF-C and SMAD4 in the lymphangiogenesis, lymphatic metastasis, and prognosis in colon cancer. *Journal of Gastrointestinal Surgery*, 15(11):2001, 2011.
- [44] Yuchao Jiang, Yu Qiu, Andy J Minn, and Nancy R Zhang. Assessing intratumor heterogeneity and tracking longitudinal and spatial clonal evolutionary history by next-generation sequencing. *Proceedings of the National Academy of Sciences*, 113(37):E5528–E5537, 2016.

- [45] Samra Turajlic, Hang Xu, Kevin Litchfield, Andrew Rowan, Stuart Horswell, Tim Chambers, Tim O'Brien, Jose I Lopez, Thomas BK Watkins, David Nicol, et al. Deterministic evolutionary trajectories influence primary tumor growth: Tracerx renal. *Cell*, 173(3):595–610, 2018.
- [46] Samra Turajlic, Hang Xu, Kevin Litchfield, Andrew Rowan, Tim Chambers, Jose I Lopez, David Nicol, Tim O'Brien, James Larkin, Stuart Horswell, et al. Tracking cancer evolution reveals constrained routes to metastases: Tracerx renal. *Cell*, 173(3):581–594, 2018.
- [47] Christopher Abbosh, Nicolai J Birkbak, Gareth A Wilson, Mariam Jamal-Hanjani, Tudor Constantin, Raheleh Salari, John Le Quesne, David A Moore, Selvaraju Veeriah, Rachel Rosenthal, et al. Phylogenetic ctDNA analysis depicts early-stage lung cancer evolution. *Nature*, 545(7655):446, 2017.
- [48] Serena Nik-Zainal, Peter Van Loo, David C Wedge, Ludmil B Alexandrov, Christopher D Greenman, King Wai Lau, Keiran Raine, David Jones, John Marshall, Manasa Ramakrishna, et al. The life history of 21 breast cancers. *Cell*, 149(5):994–1007, 2012.
- [49] Robert J Gillies, Daniel Verduzco, and Robert A Gatenby. Evolutionary dynamics of carcinogenesis and why targeted therapy does not work. *Nature Reviews Cancer*, 12(7):487–493, 2012.
- [50] Rebecca A Burrell, Nicholas McGranahan, Jiri Bartek, and Charles Swanton. The causes and consequences of genetic heterogeneity in cancer evolution. *Nature*, 501(7467):338–345, 2013.
- [51] Bert Vogelstein, Nickolas Papadopoulos, Victor E Velculescu, Shibin Zhou, Luis A Diaz, and Kenneth W Kinzler. Cancer genome landscapes. *science*, 339(6127):1546–1558, 2013.
- [52] Andrea Sottoriva, Immaculada Spiteri, Sara GM Piccirillo, Anestis Touloumis, V Peter Collins, John C Marioni, Christina Curtis, Colin Watts, and Simon Tavaré. Intratumor heterogeneity in human glioblastoma reflects cancer evolutionary dynamics. *Proceedings of the National Academy of Sciences*, 110(10):4009–4014, 2013.
- [53] Jack Edmonds. Optimum branchings. *Mathematics and the Decision Sciences, Part*, 1:335–345, 1968.
- [54] Mohammed El-Kebir, Layla Oesper, Hannah Acheson-Field, and Benjamin J Raphael. Reconstruction of clonal trees and tumor composition from multi-sample sequencing data. *Bioinformatics*, 31(12):i62–70, June 2015.
- [55] Victoria Popic, Raheleh Salari, Iman Hajirasouliha, Dorna Kashef-Haghighi, Robert B West, and Serafim Batzoglou. Fast and scalable inference of multi-sample cancer lineages. *Genome Biology*, 16(1):795–17, May 2015.
- [56] C Chow and Cong Liu. Approximating discrete probability distributions with dependence trees. *IEEE transactions on Information Theory*, 14(3):462–467, 1968.

# Learning mutational graphs of individual tumour evolution from single-cell and multi-region sequencing data

Supplementary Material

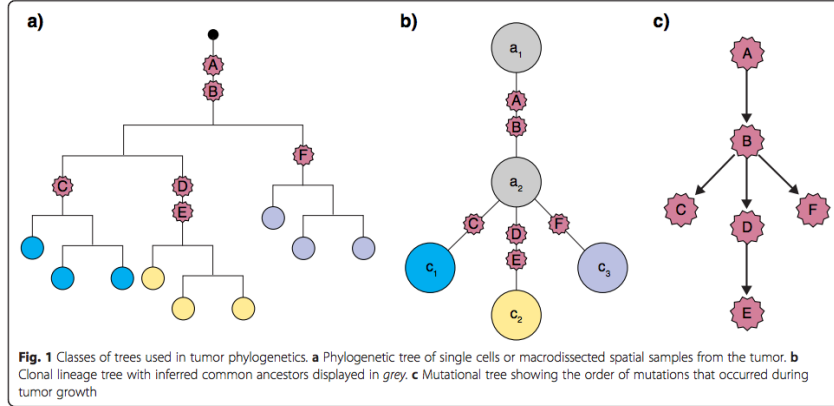
Daniele Ramazzotti, Alex Graudenzi, Luca De Sano, Marco Antoniotti, Giulio Caravagna

## Contents

<b>1</b>	<b>A framework based on probabilistic causation</b>	<b>3</b>
1.1	Preliminaries . . . . .	4
1.2	Weighted graphs with information theory . . . . .	5
1.3	Strategies for structure selection and parameters' learning . . . . .	6
<b>2</b>	<b>Testing the framework</b>	<b>9</b>
2.1	Synthetic data and performance measures . . . . .	9
2.2	Working scenarios . . . . .	11
<b>3</b>	<b>Preliminary tests</b>	<b>12</b>
3.1	Single-cell data . . . . .	12
3.2	Multi-region bulk sequencing data . . . . .	16
<b>4</b>	<b>Detailed tests with single-cell data</b>	<b>18</b>
4.1	Branching evolution . . . . .	19
4.2	Confounding Factors . . . . .	20
4.3	Multiple Independent Trajectories . . . . .	24
4.4	Inference with missing data . . . . .	24
<b>5</b>	<b>Detailed tests with multi-region bulk-sequencing data</b>	<b>26</b>
5.1	Branching evolution . . . . .	26
5.2	Confounding factors . . . . .	26
5.3	Multiple Independent Trajectories . . . . .	31
<b>6</b>	<b>Parameters settings, computation time and scalability</b>	<b>31</b>
6.1	Parameter Settings . . . . .	31
6.2	Computation time and scalability . . . . .	33
<b>7</b>	<b>Case studies</b>	<b>34</b>
<b>8</b>	<b>Noise model</b>	<b>34</b>
<b>9</b>	<b>Modeling back mutations</b>	<b>40</b>

## List of Figures

1	Three inference problem by Davis and Navin . . . . .	3
2	Cartoon of the algorithms . . . . .	7
3	Working scenarios . . . . .	13
4	Experiment I (SCS data) . . . . .	14
5	Statistical complications due to convergent trajectories . . . . .	15
6	Experiment I-MR (MR data) . . . . .	17
7	Fixed polyclonal trees . . . . .	19
8	Experiment II (branching evolution, fixed topologies, SCS data) . . . . .	21
9	Experiment III (branching evolution, random topologies, SCS data) . . . . .	22
10	Experiment V (confounding factors, fixed topologies, SCS data) . . . . .	23
11	Experiment VI (multiple independent trajectories, SCS data) . . . . .	25
12	Experiment VII (missing data, SCS data) . . . . .	27
13	Experiment II-MR (branching evolution, fixed topologies, MR data) . . . . .	28
14	Experiment III-MR (branching evolution, random topologies, MR data) . . . . .	29
15	Experiment V-MR (confounding factors, fixed topologies, MR data) . . . . .	30
16	Experiment VI-MR (multiple independent trajectories, MR data) . . . . .	32
17	Triple-negative breast cancer single-cell data: fits by CAPRI, CAPRESE and Edmond . . . . .	35
18	Triple-negative breast cancer single-cell data: fits by Gabow, Chow-Liu and PRIM . . . . .	36
19	Triple-negative breast cancer single-cell data: fits by SCITE . . . . .	37
20	Colorectal cancer multi-region data: fit with TRaIT's algorithms, CAPRI and CAPRESE . . . . .	38
21	Colorectal cancer multi-region data: fit with SCITE . . . . .	39
22	Back mutation scenario: toy example . . . . .	40



Supplementary Figure 1: The  $\star$ OP problems (image taken from [1]) as suggested by Davis and Navin, which define three ways to infer cancer progression from single-cell data. The POP (*phylogenetic ordering problem*), a classical phylogenetic inference problem where we display input cells as leaves of a phylogenetic tree. The COP (*clonal ordering problem*), where we identify a clonal lineage tree that models an ancestry-relation for a set of clones that we infer from data. The MOP (*mutational ordering problem*), where we find the order of mutations that accumulate during cancer progression. In this paper, we focus on the MOP problem.

## 1 A framework based on probabilistic causation

In Figure 1 of [1] Davis and Navin distinguish three different approaches to infer cancer progression models from data of individual patients. We summarize them in Supplementary Figure 1 and call them  $\star$ OP, mimicking the “ $\star$ -ordering problem”. Different versions of the  $\star$ OP provide insights on the evolutionary aspects of cancer progression. In particular:

- when  $\star = P$ , we solve a *classical phylogenetic inference problem* (PHY) and aim at displaying a set of input cells as leaves of a phylogenetic tree;
- when  $\star = C$ , we seek to identify a *clonal lineage tree* (CT) that models an ancestry-relation for a set of clones that we infer from data;
- when  $\star = M$ , we seek to find the order of mutations that accumulate during progression (MO).

Hopefully, results from these approaches can be somehow reconciled, as the same data type is used to approach the problem. For instance, we might argue that the order of accumulating mutations should be consistent with the clonal lineage tree, which in turn should be consistent with a phylogenetic tree of the corresponding cells that we sequence. The efforts to solve these problems are ongoing, with different techniques and tools that are becoming popular to solve the COP and the POP versions of the problem, see, e.g., [2–4]. We focus this paper on the mutational version of the problem, consistently with earlier works of us [5–10].

## 1.1 Preliminaries

We use Suppes’ framework of *probabilistic causation* as the core of our approach to cancer progression inference. We use it to derive algorithms that exploit optimal results from *minimum spanning tree reconstruction* and *Bayesian inference*. These axioms provide a *necessary but not sufficient* set of conditions to make causal claims [6–10]. In our earlier works [5–10] we considered data from multiple patients, i.e., multiple observations of the tumor progressions, to disentangle genuine from spurious causal relations. On the contrary, here we can quantify the statistical trends between mutations with Suppes’ conditions, but we need to clarify that we are observing multiple measurements from the same patient (not across different patients). Thus, our claims can not be of a general causal nature, and we have to restrict to the estimation of the temporal progression in the individual tumor. This is also reflected in the spanning tree assumption of our algorithms, which implies that one unique predecessor is assigned to every considered mutation. For these reasons, the depicted relations are valid temporal orderings, even if they might depict spurious causal relations.

### Input data

We consider a binary-valued dataset  $\mathbf{D}$  with  $n$  variables and  $m$  observations

$$\begin{matrix} & \mathbf{x}_1 & \mathbf{x}_2 & \cdots & \mathbf{x}_n \\ \mathbf{z}_1 & \left( \begin{matrix} x_{1,1} & x_{1,2} & \cdots & x_{1,n} \\ x_{2,1} & x_{2,2} & \cdots & x_{2,n} \\ \vdots & \vdots & \ddots & \vdots \\ x_{m,1} & x_{m,2} & \cdots & x_{m,n} \end{matrix} \right) & = & \mathbf{D} \end{matrix} \quad (1)$$

where the columns of  $\mathbf{D}$  are the  $n$  variables  $\mathcal{X} = \{\mathbf{x}_1, \dots, \mathbf{x}_n\}$ ,  $\mathbf{x}_i \in \{0, 1\}^m$ , and  $\mathbf{z}_1, \dots, \mathbf{z}_m$  are the  $m$  samples. Variables refer to genomic events detected by sequencing of cancer genomes (i.e., (epi)genomic alterations of various types such as, e.g., single nucleotide or structural variants, or copy number alterations). Value  $x_{i,j} = 1$  means that event  $\mathbf{x}_j$  is detected in sample  $\mathbf{z}_i$ .

*Assumptions.* We require each event  $\mathbf{x}_i$  to measure a *somatic alteration that is persistent* during tumor evolution, e.g., a mutation or a copy number variant. Epigenetic states of expression or methylation could be used only if they fulfil this condition; this is to be verified and assessed outside of our framework. A further technical assumption, not motivated by the phenomenon of cancer progression, is that no columns of  $\mathbf{D}$  are either all zeros, or ones, and that no two columns exist that are indistinguishable. For this reason in our implementation  $\mathbf{D}$  is reshaped appropriately before applying our algorithms, as we discuss in the Main Text.

### Output model

From  $\mathbf{D}$ , we want to estimate a *joint distribution*  $p(\cdot)$  over  $\mathcal{X}$  so that we can sample genotypes from our output model. In our formulation we use ideas from Bayesian Networks [11], a class of Graphical Models based on *directed acyclic graphs* augmented with parameters  $\theta$ .

A partially order set (poset) of a graph  $\mathcal{G}$  over  $\mathcal{X}$  is defined by a *partial ordering*  $\sqsubseteq$ : if  $\mathbf{x}_i \sqsubseteq \mathbf{x}_j$  than edge  $\mathbf{x}_i \rightarrow \mathbf{x}_j$  is in  $\mathcal{G}$ . For  $\mathcal{G}$  to be acyclic we also require the *transitive closure* of  $\sqsubseteq$  to have no path that start and end in the same  $\mathbf{x}_i$ . We turn  $\mathcal{G}$  into a generator for a *conditional probability*



distribution by defining the parameters

$$\boldsymbol{\theta}_{\mathbf{x}_j} = \hat{p}(\mathbf{x}_j \mid \{\mathbf{x}_i \mid \mathbf{x}_i \sqsubseteq \mathbf{x}_j\}) \quad (2)$$

where  $\hat{p}$  is a distribution conditioned to the incoming edges of  $\mathbf{x}_j$ , often called *conditional probability table* [11].  $|\boldsymbol{\theta}_{\mathbf{x}_j}|$  is exponential in the number of edges incoming to  $\mathbf{x}_j$ , if variables are binary.

When we infer a model of cancer progression for a patient, our output model will be the most likely *tree* (but in some cases it could be a *forest*, or a general graph), according to a measure of ti. A graph  $\mathcal{G}$  is a tree if (i) it has one *root node*  $\mathbf{x}_*$  with no incoming edges, and (ii) all other  $\mathbf{x}_j \neq \mathbf{x}_*$  have one incoming edge, i.e.,  $|\{\mathbf{x}_i \mid \mathbf{x}_i \sqsubseteq \mathbf{x}_j\}| = 1$ . Hence, for a tree, the parameters also simplify to  $\boldsymbol{\theta}_{\mathbf{x}_j} = \hat{p}(\mathbf{x}_j \mid \mathbf{x}_i)$ , i.e., they become linear in size. A graph  $\mathcal{G}$  is a *forest*, if it can be partitioned into a set of trees. Trees and forests are acyclic, by definition.

## 1.2 Weighted graphs with information theory

### Suppes' conditions as prior graph structure

We frame Suppes' *probabilistic causation* [12] within cancer progression [5, 6], to create a *partial ordering*  $\sqsubseteq_{\text{PF}}$  over  $\mathcal{X}$ . We dub it *prima facie*, and we will use it to create the final output model's structure  $\sqsubseteq$ . For any pair of variables  $\mathbf{x}_i$  and  $\mathbf{x}_j$ , we define

$$\mathbf{x}_i \sqsubseteq_{\text{PF}} \mathbf{x}_j \iff p(\mathbf{x}_i) > p(\mathbf{x}_j) \wedge p(\mathbf{x}_j \mid \mathbf{x}_i) > p(\mathbf{x}_j \mid \bar{\mathbf{x}}_i). \quad (3)$$

In general,  $\sqsubseteq_{\text{PF}}$  induces a *cyclic graph*. We interpret *prima facie* as a necessary condition for cancer progression, along the lines of [6]. So, we consider  $\sqsubseteq_{\text{PF}}$  to provide us with a superset of the edges that will appear in our output models; derivation of such edges is discussed in the next sections.

To include a pair of variables in  $\sqsubseteq_{\text{PF}}$ , we test two inequalities over distributions estimated from  $\mathbf{D}$ . A statistical model of those marginal and joint/ conditional distributions over  $\mathcal{X}$  can be created via *non-parametric bootstrap* [6]. Then, we can carry out a Mann-Whitney U test to compute a p-value for the alternative hypothesis that the distributions have different means:  $\mathbf{x}_i \sqsubseteq_{\text{PF}} \mathbf{x}_j$  when both inequalities have confidence below some desired p-value (e.g.,  $p < 0.05$ ). This testing/ bootstrap schema can support prior information of noise in the data. If we are informed that  $\mathbf{D}$  harbours *false positives and negatives* rates  $\epsilon_+$  and  $\epsilon_-$ , we can correct the marginal bootstrap estimates as

$$p(\mathbf{x}_i) = \frac{n_i - \epsilon_+}{1 - \epsilon_+ - \epsilon_-}, \quad (4)$$

where  $n_i = \frac{\sum_k x_{k,i}}{m}$ , and proceed similarly for the joint estimates as follows

$$p(\mathbf{x}_{i,j}) = \frac{n_{i,j} - \epsilon_+[n_i + n_j - \epsilon_+]}{(1 - \epsilon_+ - \epsilon_-)^2}, \quad (5)$$

where  $n_{i,j} = \frac{\sum_k x_{k,i}x_{k,j}}{m}$ . See Section 8 for the complete derivation of the error model.

### Information-theoretic measures for associations' detection

The ordering  $\sqsubseteq_{\text{PF}}$  is a super set of the ordering that we want to return as output; we thus need to subset  $\sqsubseteq_{\text{PF}}$ . To rank and select pairs in  $\sqsubseteq_{\text{PF}}$  we can use a score function. If we interpret each  $\mathbf{x}_i$  as a random variable with binary outcomes, we can compute information-theoretic measures for the detection of its degree of association to other variables [13]. For each  $\mathbf{x}_i \sqsubseteq_{\text{PF}} \mathbf{x}_j$ , we measure the *point-wise mutual-information* (**pmi**)

$$\text{pmi}(\mathbf{x}_i = x, \mathbf{x}_j = y) = \log \left[ \frac{p(\mathbf{x}_i = x, \mathbf{x}_j = y)}{p(\mathbf{x}_i = x)p(\mathbf{x}_j = y)} \right], \quad (6)$$

that quantifies the discrepancy between  $\mathbf{x}_i$  and  $\mathbf{x}_j$  for their outcomes  $x$  and  $y$ . Here, to detect the association between alterations that accumulate during progression, we set  $x = y = 1$ .

In some cases, we will also use the expected value of **pmi** over all the possible outcomes of  $\mathbf{x}_i$  and  $\mathbf{x}_j$ , which is the *mutual information* (**mi**)

$$\text{mi}(\mathbf{x}_i, \mathbf{x}_j) = \sum_{x,y} p(\mathbf{x}_i = x, \mathbf{x}_j = y) \text{pmi}(\mathbf{x}_i = x, \mathbf{x}_j = y). \quad (7)$$

These measures are standard [13], and could be used to derive alternative score functions (e.g., conditional pointwise or entropy). In this work, however, we limit our scope to **pmi** and **mi**.

### 1.3 Strategies for structure selection and parameters' learning

The prima facie ordering  $\sqsubseteq_{\text{PF}}$  induces a mapping to  $2^{|\sqsubseteq_{\text{PF}}|}$  potential models. Some of these are not trees or might model the distribution of the data poorly. The problem of picking a particular  $\sqsubseteq$  to build  $\mathcal{G}$  is hence non-trivial.

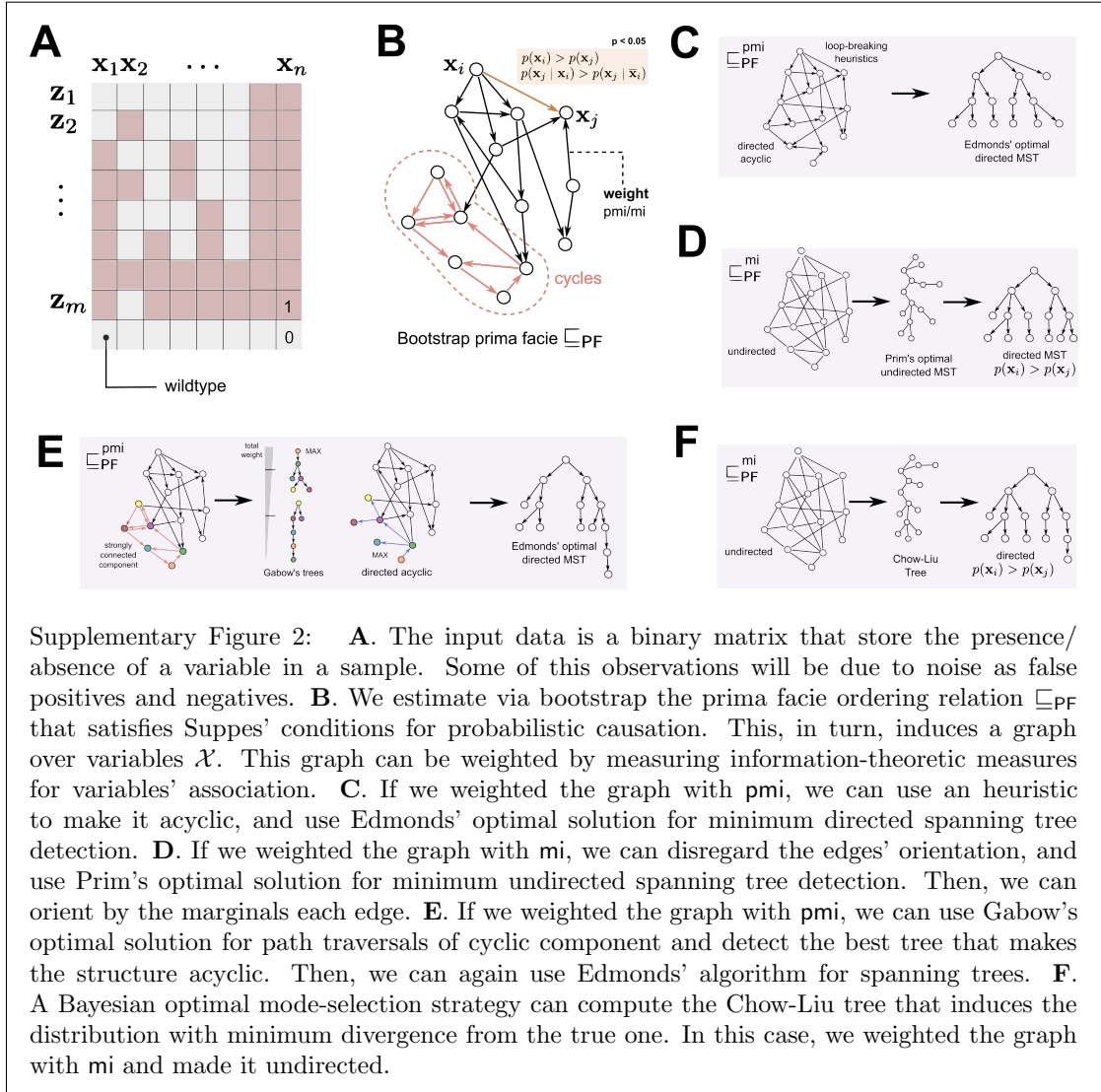
By combining  $\sqsubseteq_{\text{PF}}$  with a **pmi**/**mi** score we have obtained a *weighted graph*. Thus, we can exploit algorithms that extract trees (or other types of models) with certain properties, from the input graph. We denote with  $\sqsubseteq_{\text{PF}}^{\text{pmi}}$  and respectively with  $\sqsubseteq_{\text{PF}}^{\text{mi}}$  the graphs weighted with **pmi** or **mi**. We group a number of algorithms for structure selection into two classes: (*minimum*) *spanning tree algorithms* and *Bayesian model selection methods*.

#### Minimum spanning tree algorithms

These are a class of algorithms that aim at detecting the subset of pairs  $\sqsubseteq$  that (*i*) minimize the total output structure's weight, and that (*ii*) display as a tree. The total weight is defined as the summation of the weights of the pairs that are selected. This is a well-known problem in graph theory, and we can exploit optimal solutions from the literature. The approaches are different according to the graph that these algorithms are given as input.

We note that using "spanning tree" algorithms is a standard technique in the field [14,15]. Our approach is not different in spirit, while we reuse these algorithms with a different weight structure induced by Suppes' causal ordering  $\sqsubseteq_{\text{PF}}$ .

**Edmond:** Edmonds' optimum branching algorithm is a canonical solution to the task of inferring a spanning tree of minimum weight from a weighted directed graph, given a root node in input [16]. We use this algorithm with  $\sqsubseteq_{\text{PF}}^{\text{pmi}}$  as input, *provided that we make it acyclic*. Cycles/ loops breaking is a hard computational problem, and we resort on the heuristic that



Supplementary Figure 2: **A**. The input data is a binary matrix that store the presence/absence of a variable in a sample. Some of this observations will be due to noise as false positives and negatives. **B**. We estimate via bootstrap the prima facie ordering relation  $\sqsubseteq_{PF}$  that satisfies Suppes' conditions for probabilistic causation. This, in turn, induces a graph over variables  $\mathcal{X}$ . This graph can be weighted by measuring information-theoretic measures for variables' association. **C**. If we weighted the graph with pmi, we can use an heuristic to make it acyclic, and use Edmonds' optimal solution for minimum directed spanning tree detection. **D**. If we weighted the graph with mi, we can disregard the edges' orientation, and use Prim's optimal solution for minimum undirected spanning tree detection. Then, we can orient by the marginals each edge. **E**. If we weighted the graph with pmi, we can use Gabow's optimal solution for path traversals of cyclic component and detect the best tree that makes the structure acyclic. Then, we can again use Edmonds' algorithm for spanning trees. **F**. A Bayesian optimal mode-selection strategy can compute the Chow-Liu tree that induces the distribution with minimum divergence from the true one. In this case, we weighted the graph with mi and made it undirected.

is used by the CAPRI algorithm [6]. This heuristics breaks loops according their confidence, defined as the combination of  $p$ -values for Suppes' conditions: edges with small confidence (i.e., high p-values) are deleted first to break loops. When  $\sqsubseteq_{PF}^{pmi}$  is made acyclic, to use Edmonds' algorithm and maximize our pmi scores, we can change their sign. The running time of this algorithm is  $\mathcal{O}(|\mathcal{X}| \cdot |\sqsubseteq_{PF}^{pmi}|)$ , which can be optimized to  $\mathcal{O}(|\mathcal{X}| \log(|\sqsubseteq_{PF}^{pmi}|))$  for sparse<sup>1</sup>  $\sqsubseteq_{PF}^{pmi}$  [17].

<sup>1</sup>An ordering relation is sparse if its associated matrix over  $\{0, 1\}^{\mathcal{X} \times \mathcal{X}}$  is sparse.

**Prim:** Prim’s algorithm is the equivalent of Edmonds’ for undirected tree structures [18]. We can use Prim’s algorithms by disregarding the directionality of the edges in our prima facie ordering, i.e., if for every pair  $\mathbf{x}_i \sqsubseteq_{\text{PF}} \mathbf{x}_j$  we also force the inclusion of  $\mathbf{x}_j \sqsubseteq_{\text{PF}} \mathbf{x}_i$  no matter what the test statistics for Suppes’ conditions. If we want to use this search strategy, however, we will use  $\sqsubseteq_{\text{PF}}^{\text{mi}}$  as input, as we need to use a measure that is symmetric and defined over all the support of the random variables (i.e., pmi is not accounting for the cases  $\mathbf{x}_i = 1 - \mathbf{x}_j = 1$  and viceversa). The complexity of this algorithm, if it is implemented by using a binary heap and an adjacency list for  $\mathcal{G}$ , is the same as Edmonds’. The final tree returned by this strategy is undirected, and so we orient it according to the marginal frequencies of the events. That is, for every final pair  $\mathbf{x}_i \sqsubseteq_{\text{PF}} \mathbf{x}_j$  and  $\mathbf{x}_j \sqsubseteq_{\text{PF}} \mathbf{x}_i$  we select  $\mathbf{x}_i \rightarrow \mathbf{x}_j$  if  $p(\mathbf{x}_i) > p(\mathbf{x}_j)$ . For this reason, the final model could contain confluent structures such as  $\mathbf{x}_i \sqsubseteq_{\text{PF}} \mathbf{x}_j$  and  $\mathbf{x}_k \sqsubseteq_{\text{PF}} \mathbf{x}_j$  – i.e., a model with two edges confluent in  $\mathbf{x}_j$ :  $\mathbf{x}_i \rightarrow \mathbf{x}_j$  and  $\mathbf{x}_k \rightarrow \mathbf{x}_j$ . We observe that, when this happen, the final model is not a tree as  $\mathbf{x}_j$  has more than one parent, but a multi-rooted directed acyclic graph (DAG). The interpretation in terms of the induced distribution is still that of a Bayesian Network.

**Gabow:** Cycles in  $\sqsubseteq_{\text{PF}}^{\text{pmi}}$  can be handled in another search schema by exploiting Gabow’s algorithm [19], before using Edmond’s algorithm to maximize the weight of the final tree. Gabow’s algorithm is optimal to detect the *strongly connected components* of the directed graph  $\sqsubseteq_{\text{PF}}^{\text{pmi}}$  in time  $\mathcal{O}(|\mathcal{X}| + |\sqsubseteq_{\text{PF}}^{\text{pmi}}|)$  if the graph is represented as an adjacency list. If  $\sqsubseteq_{\text{PF}}^{\text{pmi}}$  has cycles, we thus create, for each strongly connected component, all the possible trees associated; then we select the tree at maximum weight for each such set of candidates. We can optimize this procedure by separating acyclic sub-graphs, if any, in the very beginning. This algorithm is optimal but more expensive than Edmond, and shall be seen as an alternative way to deal with loops in the prima facie structure.

### Bayesian model-selection strategies

**Chow-Liu:** This is an optimal method for constructing a *second-order product approximation* of the joint probability distribution over  $\mathcal{X}$  [20]. It is known that the resulting tree minimizes the Kullback-Leibler distance to the actual joint distribution, and can be interpreted as a Bayesian Network. For constructing the optimal tree, at each iteration the algorithm adds the maximum mi pair to the tree. This algorithm returns an undirected structure when we run it with  $\sqsubseteq_{\text{PF}}^{\text{mi}}$  as input; we transform it into a directed structure as we do with the Prim search strategy. The similarity between the two algorithms is evident, also in terms of complexity.

### Learning parameters $\theta$

Given a graph (or, as a special case a tree), we can fit its parameters using a standard technique in the Bayesian Networks approach, by maximum likelihood estimation from  $\mathbf{D}$  [11].

### Comparison with other algorithms

As motivated in the Main Text, SCITE and OncoNEM are at the state-of-the art for two orthogonal problems in single-cell phylogenetic inference (mutational vs clonal ordering). In our simulations we compared the different model search methods just listed against SCITE, since its mutational tree is directly comparable to our models.

We note that we were not able to test all the simulation scenarios we created with OncoNEM, as, at the time of testing, its performance scaled poorly to carry out our large scale test. See for instance Supplementary Supplementary Table 6 with some example timings to run these comparisons.

## 2 Testing the framework

### 2.1 Synthetic data and performance measures

Comparison among the algorithms is based on large synthetic tests for different combinations of model type, size, number of samples, noise etc. We describe here the details of the approach, and provide the user with its R implementation in the [TRONCO tool](#) which is available at

<https://sites.google.com/site/troncopackage>

and on Bioconductor.

We devised a testing framework to gather information about the relative performance of TRaIT in a number of different scenarios.

1. Sampling from *Single-cells* (SCs) sequencing data.
2. Sampling from *Multi-region bulk* sequencing data.

In each case we take care to explore the problems induced by the presence of noise in the data.

#### Sampling from Single-cell sequencing

Genotypes from single-cell sequencing are sampled by a phylogeny. We describe the simpler case of sampling from a single tree, more general cases are trivial extensions. A cartoon is shown in Supplementary Figure 3 that shows some possible single-cell genotypes.

The following recursive procedure visits a tree, starting from its root  $x_*$  (i.e., we set  $\mathbf{x}_* = 1$  in the genotype), and outputs a sampled genotype according to its structure and parameters.

- If we are visiting a leaf  $\mathbf{x}_l$  (i.e., a node without outgoing edges) with incoming edge  $\mathbf{x}_i \rightarrow \mathbf{x}_l$ , then we sample  $\mathbf{x}_l = 1$  (in the genotype) with probability  $\theta_{\mathbf{x}_l} = p(\mathbf{x}_l | \mathbf{x}_i)$ , and 0 otherwise.
- if we are visiting a branching node  $\mathbf{x}_i$  (i.e.,  $\mathbf{x}_i = 1$  in the genotype) with children  $\mathbf{x}_i \rightarrow \mathbf{x}_j$  and  $\mathbf{x}_i \rightarrow \mathbf{x}_k$  we either sample only one of the children and we proceed recursively, or we stop. Notice that we forbid to sample a genotype with both children<sup>2</sup>, i.e.,  $p(\mathbf{x}_j, \mathbf{x}_k | \mathbf{x}_i) = 0$ , so

$$\begin{aligned} p(\mathbf{x}_j | \mathbf{x}_i) &= p(\mathbf{x}_j, \bar{\mathbf{x}}_k | \mathbf{x}_i) + p(\mathbf{x}_j, \mathbf{x}_k | \mathbf{x}_i) = p(\mathbf{x}_j, \bar{\mathbf{x}}_k | \mathbf{x}_i) \\ p(\mathbf{x}_k | \mathbf{x}_i) &= p(\bar{\mathbf{x}}_j, \mathbf{x}_k | \mathbf{x}_i) + p(\mathbf{x}_j, \mathbf{x}_k | \mathbf{x}_i) = p(\bar{\mathbf{x}}_j, \mathbf{x}_k | \mathbf{x}_i). \end{aligned} \quad (8)$$

Thus, genotype with  $\mathbf{x}_i = \mathbf{x}_j = 1 - \mathbf{x}_k$  has probability  $\theta_{\mathbf{x}_j} = p(\mathbf{x}_j | \mathbf{x}_i)$ , while genotype with  $\mathbf{x}_i = \mathbf{x}_k = 1 - \mathbf{x}_j$  has probability  $\theta_{\mathbf{x}_k} = p(\mathbf{x}_k | \mathbf{x}_i)$  and genotype  $\mathbf{x}_i = 1 - \mathbf{x}_j = 1 - \mathbf{x}_k$  has probability  $1 - [p(\mathbf{x}_j | \mathbf{x}_i) + p(\mathbf{x}_k | \mathbf{x}_i)]$ . To have consistent cell genotypes for the whole model, when we recursively proceed with  $\mathbf{x}_j$  (resp.  $\mathbf{x}_k$ ) we set  $\mathbf{x}_k$  (resp.  $\mathbf{x}_j$ ) and all its descendants equal to 0.

---

<sup>2</sup>This is analogous of saying that, at the genotype level, every branching is interpreted as an *exclusive branch*. In this case the truth table for  $\mathbf{x}_i$ ,  $\mathbf{x}_k$  and  $\mathbf{x}_k$  resembles a xor-network when  $\mathbf{x}_i = 1$ .

Notice that, by construction, genotypes are consistent with the phylogeny of the generative model, as  $p(\mathbf{x}_j, \mathbf{x}_k | \bar{\mathbf{x}}_i) = p(\bar{\mathbf{x}}_j, \mathbf{x}_k | \bar{\mathbf{x}}_i) = p(\mathbf{x}_j, \bar{\mathbf{x}}_k | \bar{\mathbf{x}}_i) = 0$  for any branching structure.

We observe that: (i) we can easily generalize this procedure to an arbitrary amount of children per branching, and that (ii) this procedure generates only genotypes that correspond to cancer cells (because we start with  $\mathbf{x}_* = 1$ ). If required, we can a posteriori add wild-type genotypes to a dataset to account for contamination of normal cells.

### Sampling from Multi-region bulk sequencing

When we collect and sequence a bulk of tumor cells we get a signal that is a mixture of alterations found in different tumor sub-populations.

In terms of induced distribution and the branching structures described in single-cell sequencing sampling, this means that data will support  $p(\mathbf{x}_i = \mathbf{x}_j = \mathbf{x}_k) > 0$  as the sequenced samples will contain cells from both populations with signatures  $\mathbf{x}_i = \mathbf{x}_j = 1 - \mathbf{x}_k$  and  $\mathbf{x}_i = \mathbf{x}_k = 1 - \mathbf{x}_j$ . To create such a signal there are different ways. On one hand, one can change the effect of branchings on the induced distribution to account for  $p(\mathbf{x}_i = \mathbf{x}_j = \mathbf{x}_k) > 0$ , on the other one can emulate a mixed signal by mixing a number of individual signals. The former approach requires more parameters in the generative model to account for the conditional probabilities of both children, given a parent node. We adopt the latter approach and sample  $c$  genotypes from a single-cell sequencing experiment: let  $\mathbf{z}_1, \dots, \mathbf{z}_c$  be such samples, we create a sample

$$\mathbf{z}_* = \bigvee_i \mathbf{z}_i \tag{9}$$

where each component of  $\mathbf{z}_*$  is 1 if at least one  $\mathbf{z}_i$  is 1. Then, we repeat the procedure to produce as many samples as we need, according to the number of regions that we want to simulate.

This approach requires only one more parameter,  $c$ . If one interprets the  $c$  samples as  $c$  cells, one might be tempted to pick a very large  $c$  (e.g.,  $c \gg 10^6$ ). If one does so, however, all  $\mathbf{z}_*$  will be similar, as for large  $c$  the proportions of the sampled genotypes will converge to the true ones. Thus, our dataset would have small variance across samples, biasing the data. Thus, to have more variance, we set  $c$  to be small ( $c < n$ ) and interpret  $c$  as the probabilistic number of clones spread across the regions that we sequence.

### Adding noise to synthetic data

When we say that observed data are obtained by adding noise to sampled genotypes, we mean the usual introduction of *false positives and negatives* with rates  $\epsilon_+ \geq 0$  and  $\epsilon_- \geq 0$ , respectively [2,3,6]. Precisely, when we have sampled a dataset of samples  $D$  according either to (8) or (9), we apply to  $D$  an independent point-wise process that flips the matrix's entries according to the rates  $\epsilon_+/\epsilon_-$ .

To investigate the ideal performance of the algorithms we sometimes use *noise-free* data, that is  $\epsilon_+ = \epsilon_- = 0$ . In more realistic setting, we use different models of noise according to the type of simulate sequencing. Sequencing of single cells is characterized by distinct errors, which usually take place in the DNA amplification phase: (i) *allelic dropouts* and (ii) *false alleles*, the former occurring at a significantly higher rate, thus leading to higher rates of false negatives. Accordingly, in the generation of noisy single-cell data we expect highly asymmetric noise parameters  $\epsilon_+ \ll \epsilon_-$ , that we simulate by assuming one-order of magnitude in their difference. Multi-region bulk sequencing data instead harbour more balanced noise effects, in that case we set  $\epsilon_+ = \epsilon_-$ .

## Performance measured

We want to measure the tendency to overfit or underfit of every algorithm, in particular circumstances of sample size, noise etc. Thus, the performances measured in each experiment are:

- the rate at which *true model edges are inferred*

$$\textit{sensitivity} \quad \frac{\text{TP}}{\text{TP}+\text{FN}};$$

- the rate at which *false model edges are discarded*

$$\textit{specificity} \quad \frac{\text{TN}}{\text{TN}+\text{FP}};$$

where TP, TN, FP, FN are the number of true (T)/ false (F) positives (P) and negatives (N).

## Algorithms' implementation

We used the official release of each tool.

- CAPRI, CAPRESE and the algorithms that we describe in this paper are available in [TRONCO](#).
- SCITE was downloaded from its [Github repository](#).
- OncoNEM was downloaded from its [Bitbucket repository](#).

## 2.2 Working scenarios

We define four possible working scenarios, which represent distinct cancer evolution *modes* and related phenomena (Supplementary Supplementary Figure 3).

### Branching evolution

In this case different cancer subclones (with distinct lineages) diverge from a common ancestor and are characterized by distinct accumulating alteration. This can be modelled via trees with distinct branches describing the subclonal trajectories. Particular instances of this scenario is *linear evolution*, in which alterations accumulate along a linear path, with no branches.

### Confounding factors

In this case the generative models are phylogenetic trees, as above, but the observed data also include *uncorrelated random events*. This is a handle to account for possible *confounding factors*, i.e., (epi)genomic alterations that have no functional role in the progression, and that we do not know a priori.

### Multiple independent trajectories

In this case the generative topology are multiple independent trees, grouped as a *forest*. This is a way to model tumors that originate from two or more cells, a phenomenon also known as *polyclonal tumor origin* [21], or the possible presence of *hidden* events triggering tumor development, but not annotated in the available data (e.g., methylations).

According these working scenarios, we perform a simple non-exhaustive test of the performance of the algorithms, with single-cell and multi-region data.

### 3 Preliminary tests

These tests are rather simple in size and variability of settings, and more detailed tests are carried out in the next sections. However, they still give a general idea of the general performance trend.

#### 3.1 Single-cell data

##### Experiment I.

We test a set of fixed topologies according to the scenarios in Supplementary Figure 3: (i) a tree with  $n = 11$  nodes (*Branching evolution*), (ii) which we then augment with the addition of 2 disconnected nodes (*Confounding factors*), (iii) a forest with two distinct trees that account for  $n = 7$  nodes (*Multiple independent trajectories*). For each single test we generated 100 single-cell datasets with  $m = 75$  samples and a mild noise setting,  $\epsilon_+ = 0.005$   $\epsilon_- = 0.05$ .

##### Results: (Supplementary Figures 4, 5; Supplementary Tables 1, 2,

###### 1. *Branching evolution*

The performances of all the algorithms are consistently similar and very good. Yet, **Gabow** and **Edmond** with **pmi** reach highest performance, while **SCITE** displays a larger dispersion. All algorithm but **CAPRI** have similar median sensitivity, suggesting a comparable capability of inferring the true relations from data. Specificity scores, instead, suggest that **SCITE** tends to overfit more than other approaches (i.e., lower true negative rate). **CAPRI** displays a very high specificity, but that is possibly due its “regularization” approach that tends to return sparse models (thus, trading specificity for sensitivity)<sup>3</sup>.

###### 2. *Confounding factors*

A similar trend is observed also in this scenario, with **SCITE** displaying a very good sensitivity, but also the lowest specificity among all. We can observe that the best algorithm in this case seems to be **Prim**, as it displays the same sensitivity of **SCITE**, but higher specificity. **CAPRI**’s very high specificity is still due to the regularization terms. We finally show in Supplementary Table 1 that our approach is capable to model these progressions, with the confounding factor consistently presenting a much lower trend of significance, compared to all the other events.

###### 3. *Multiple independent trajectories*

In this case **Gabow**, **Edmond** and **SCITE** present an identical performance with median values of both specificity and sensitivity equal to 100%, slightly outperforming the other algorithms. In particular, by looking at Supplementary Table 2 one can notice that all the techniques are able to retrieve the two distinct roots of the progression, with the exception of **PRIM** and **CAPRESE** in a few cases.

---

<sup>3</sup>This is a general trend of this algorithm that we expect to observe in all the experiments. Thus, we omit from commenting it any further.

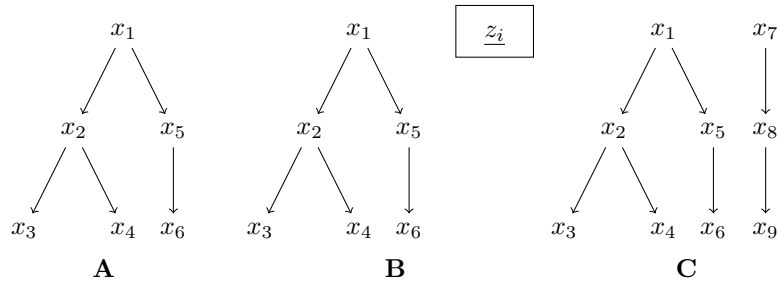


Example genotypes sampled from the models below

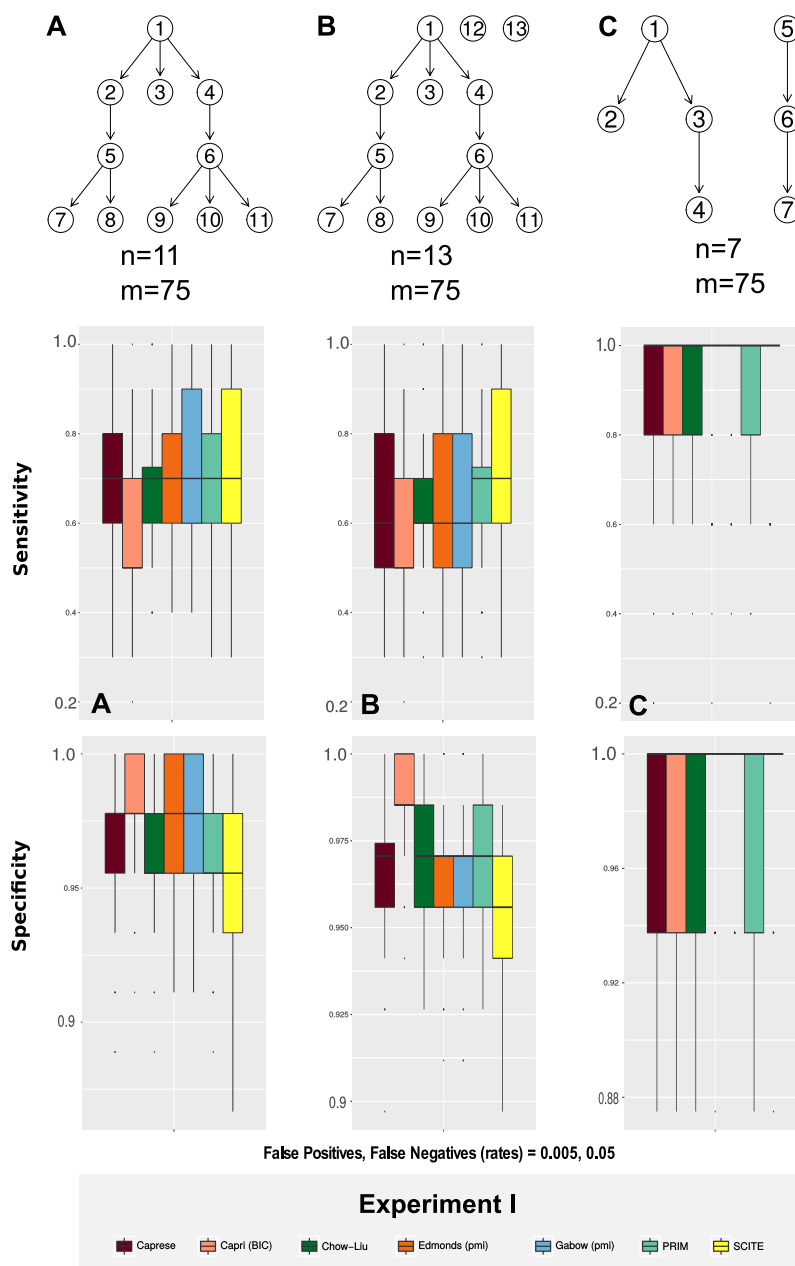
- A** *single-cell*:  $x_1x_2x_3, x_1x_5, x_1x_5x_6$   
*multi-region*:  $x_1x_2x_3, x_1x_2x_5$  (e.g.,  $x_1x_2/x_1x_5$ ),  $x_1x_5x_6x_2x_4$  (e.g.,  $x_1x_2x_4/x_1x_5x_6$ )
- B** *single-cell*:  $x_1x_2x_3z_1z_2, x_1x_5z_2, x_1x_5x_6$   
*multi-region*:  $x_1x_2x_5z_1z_2$  (e.g.,  $x_1x_2z_1/x_1x_5z_2$  or  $x_1x_2z_1z_2/x_1x_5$  or ...)
- C** *single-cell*:  $x_1x_2x_3, x_7x_8, x_1, x_7x_8x_9$   
*multi-region*:  $x_1x_2x_5$  (e.g.,  $x_1x_2/x_1x_5$ ),  $x_1x_2x_5x_7x_8$  (e.g.,  $x_1x_2/x_1x_5/x_7x_8$ )

Observed data obtained by applying noise to genotypes

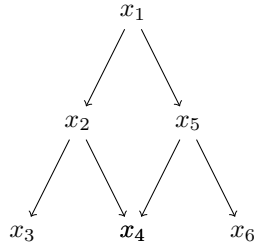
In **A**, the single-cell genotype  $x_1x_2x_3$  might be observed as  $x_1x_3$ , when  $x_2$  is not detected (false negative), or as  $x_1x_2x_3x_4$  when  $x_4$  is wrongly detected (false positive).



Supplementary Figure 3: **A**. Branching evolution. This phylogenetic tree has 6 nodes (one for each alteration  $x_i$ ), and a unique variant/cell of origin,  $x_1$ . This is the most common case in which inference is carried out. **B**. Confounding factors. A phylogenetic model can be extended with spurious variables  $z_i$  that confound the inference problem. The inference is hindered because we have to detect the spuriousness of the association between any  $z_i$  and the true variants  $x_i$ . **C**. Multiple independent trajectories. A forest of phylogenetic models can describe the presence of multiple independent progressions that start from different variants ( $x_1$  and  $x_7$ ), as it might happen with tumors that start from different cells of origin, or with hidden/ not-annotated events triggering tumor development.



Supplementary Figure 4: Experiment I.(SCS data). We test the CAPRESE ( $\lambda = 0.5$ ), CAPRI (with BIC regularization) and SCITE (default parameters) against our new algorithms, for model inference from single-cell data with noise  $\epsilon_+/\epsilon_- = 0.005/0.05$ . We use Gabow and Edmond with pointwise mutual information (pmi). The boxplots present sensitivity and specificity scores for 100 distinct datasets representing the working scenarios discussed in Section 2.2. Results are discussed in Section 2.2. Parameters are reported in Section 6. **A.** Branching evolution. **B.** Confounding factors. **C.** Multiple independent trajectories.



Supplementary Figure 5: **Statistical complications due to convergent trajectories.** Example of evolution in a single patient with convergent trajectories; this model does not fulfill the Infinite Sites Assumption (ISA) model. This specific case shows possible statistical issues complicating the inference, and limitations of our approach. Specifically, let us focus on a subset of 6 possible genotypes derived from the generative model above:  $x_1x_2$ ,  $x_1x_2x_3$ ,  $x_1x_2x_4$ ,  $x_1x_5$ ,  $x_1x_5x_4$  and  $x_1x_5x_6$ . We now focus on the nodes presenting confluent trajectories, i.e.,  $x_2 \rightarrow x_4$  and  $x_5 \rightarrow x_4$ , and consider the probabilities involved in estimating the prior graph structure for these relations. Consider a fictitious dataset with 10 samples and assume that: (i) genotypes  $x_1x_2x_3$  and  $x_1x_5x_6$  are very rare and never observed in our dataset, (i.e., with probability 0); (ii) genotypes  $x_1x_2x_4$  and  $x_1x_5x_4$  have 4 times the probability of being observed than genotypes  $x_1x_2$  and  $x_1x_5$ , (i.e., the former with probability 0.4 and the latter 0.1). We compute the marginal and joint probabilities for all the variables of interest:  $p(x_2) = p(x_5) = 0.5$ ,  $p(x_4) = 0.8$ ,  $p(x_2, x_4) = p(x_4, x_5) = 0.4$ . We observe that in this scenario Suppes' temporal priority is reverted; in fact, being  $p(x_4) = 0.8 > 0.5 = p(x_2) = p(x_5)$ ,  $x_4$  is estimated to be earlier in time than  $x_2$  and  $x_5$ . At the same time, the 3 events present perfect independence – in fact,  $p(x_2, x_4) = p(x_4, x_5) = p(x_2) \cdot p(x_4) = p(x_4) \cdot p(x_5) = 0.4$  – and for this reason also the probability raising condition would be violated. Although what shown here is a pretty rare and unfortunate configuration, we still point out that convergent trajectories especially in the case of hard exclusivity among the parents (such as this one), may further complicate the inference.

	p-value poset	p-value (Edmond)	Edges (Edmond)
Node 1	0.05	1.20e-04	1.00
Node 2	0.09	1.00e-02	2.00
Node 3	0.12	5.06e-07	2.00
Node 4	0.13	2.37e-06	1.17
Node 5	0.11	2.00e-02	1.00
Node 6	0.12	5.25e-06	1.01
Node 7 (confounding)	<b>0.44</b>	<b>4.00e-01</b>	<b>0.77</b>

Supplementary Table 1: Experiment I (confounding factors.) Mean p-values for probability raising, for each in/out-coming arcs in each node of Suppes’ poset, and in the topology inferred by Edmond, for which we show the average number of arcs per node. The statistics are averaged over 100 SCS datasets generated from the low polyclonal tree topology with 1 confounding factor and  $n = 7$  nodes (Supplementary Figure 7). We used a noise-free configuration and 100 samples.

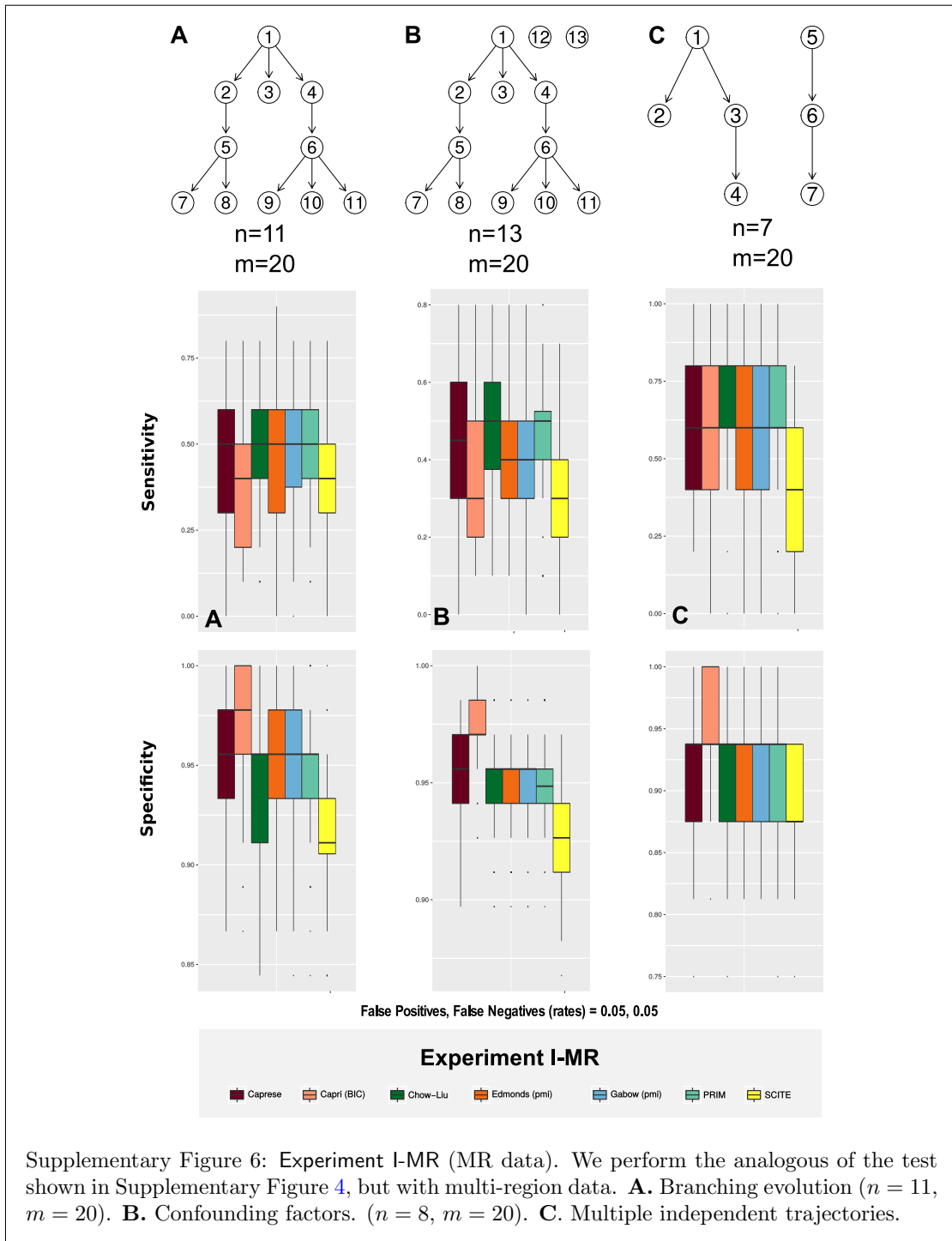
## 3.2 Multi-region bulk sequencing data

### Experiment I-MR

We reproduce Experiment I with multi-region data sampled from the same generative topologies of Supplementary Figure 4. The parameters are identical to Experiment I, with the exception of the number of samples (here biopsies, rather than cells), which is set to  $m = 20$ .

### Results: (Supplementary Figure 6, Supplementary Tables 3)

1. *Branching evolution.* All the algorithms but CAPRI and SCITE display identical median values of sensitivity and specificity, with Gabow slightly outperforming other techniques. However, all the algorithms struggle in retrieving a large number of true relations, as the median sensitivity ranges around 50% for most techniques. In this case, SCITE is the least accurate algorithm, showing a poor efficacy in retrieving both true positives and true negatives, whereas CAPRI displays high specificity and low sensitivity.
2. *Confounding factors.* The overall performance slightly worsens with confounders. In particular, the average sensitivity values are lower because the confounders introduces spurious correlations. The general trend is however preserved, with Gabow and SCITE being the most and least accurate algorithms.
3. *Multiple independent trajectories.* CAPRI, Prim and Chow-Liu show a slightly better trade-off between sensitivity and specificity, while SCITE is less accurate with this mixed signal. More in detail, most algorithms are unable to infer the two distinct roots of the progression, with the exception of CAPRESE and CAPRI which succeed in around half of the cases (Supplementary Table 3). Edmond and Gabow display a slightly better performance than the remaining techniques, yet remarkably worse than the SCS case.



	Roots		
	1	2	3
CAPRESE	0	98	2
CAPRI	0	100	0
CHOW-LIU	0	100	0
PRIM	0	83	17
GABOW	0	100	0
EDMONDS	0	100	0
SCITE	0	100	0

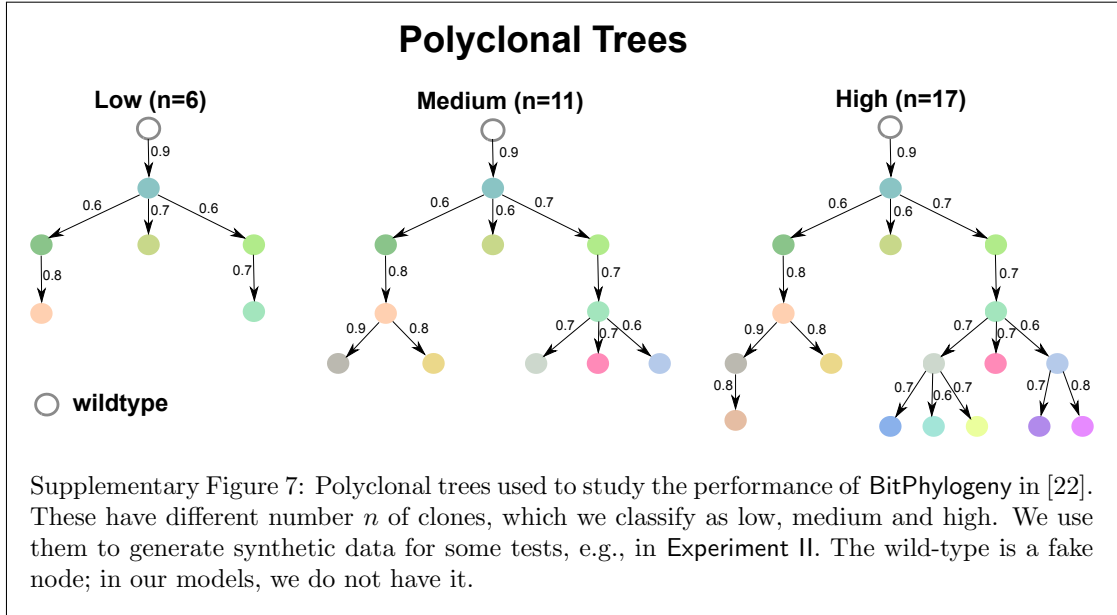
Supplementary Table 2: Experiment I (multiple independent trajectories). Number of inferred models with 1, 2 or 3 distinct roots, from 100 different SCS as in Supplementary Figure 4C.

	Roots				
	1	2	3	4	6
CAPRESE	34	51	11	4	0
CAPRI	7	43	35	12	3
CHOW-LIU	96	2	1	1	0
PRIM	96	2	1	1	0
GABOW	81	16	2	1	0
EDMONDS	82	15	2	1	0
SCITE	98	2	0	0	0

Supplementary Table 3: Experiment I-MR. (multiple independent trajectories). Number of inferred models with 1 to 6 roots, from 100 different multi-region datasets generated from a forest with 2 roots. Input models have  $n = 7$  nodes, see Supplementary Figure 6C.

## 4 Detailed tests with single-cell data

We present results from a large-scale test with single-cell data generated (*i*) from biologically plausible phylogenetic models, and (*ii*) from a large number of randomly generated topologies. We consider three scenarios (branching evolution, confounding factors, and multiple independent trajectories).



## 4.1 Branching evolution

### Experiment II

We consider polyclonal tumors originating from a unique cell, in a single-cell sequencing experiment. To generate data we fix the phylogenetic trees in Supplementary Figure 7 [22]. These trees have variable number of clones ( $n = 6, 11, 17$ ); we use them to sample different number of sequenced cells ( $m = 10, 50, 100$ ). Besides one ideal noise-free setting, we perturb data with plausible medium and high asymmetric noise rates ( $\epsilon_+/\epsilon_-$ ), in order to mimic characteristic errors in sampling cells and calling mutations. We compare the performance with over 4000 independent tests.

### Results (Supplementary Figure 8).

Reasonably, the overall performance of each algorithm is higher with lower levels of noise and larger datasets. In the ideal cases of noise-free data and 100 sampled cells, for instance, all algorithms converge to the true generative model. Noteworthy, in many realistic cases, median sensitivity and specificity measures are above 90%. The overall performance trend depends on model size ( $n$ ), the smaller models being easier to infer as one might expect. For all algorithms, the ability to detect true relations (sensitivity) clearly drops for pathological settings (e.g., we infer 20% of the true edges for the 17-clones model, when we sequence 10 cells).

Gabow, Edmond and SCITE, display a similar superior ability to infer the true relations (i.e., high sensitivity). However, SCITE seems to overfit (i.e., with a 10% loss of specificity for the 17-clones model, when we sequence 100 cells). This is particularly evident with small datasets and models. It also persists with larger models, most likely because of the larger search space for its MCMC heuristics. CAPRI, as expected, shows very high specificity but low sensitivity, due to BIC

regularization.

**Experiment III.** *We generalize Experiment II to 100 randomly sampled topologies with variable number of nodes ( $n = 5, 10, 20$ ). This shall avoid any bias induced by holding fixed the polyclonal topologies in Supplementary Figure 7.*

**Results (Supplementary Figure 9):** In general, the results partially reflect those of Experiment II. All the algorithms display very good performances in most settings, in many cases converging to the generative topologies (especially with small models, i.e., with  $n = 5, 10$  nodes). A very similar and optimal overall performance is that obtained by Gabow, Edmond, CAPRESE and SCITE, with minor differences in the different parameter settings, yet with an evident tendency of SCITE in inferring denser models with more false positives (i.e., highlighting a lower specificity). Also in this case CAPRI show a very good specificity because of the regularization, but fails in capturing many true positives.

**Experiment IV.** *In order to assess the robustness of the inference with respect to different rates of false positives and false negatives rates provided as input to the algorithms, we investigated the variation of the performance of two selected algorithms, namely Gabow and SCITE, on a dataset generated from the Medium phylogenetic tree in Supplementary Figure 7, with  $n = 11$  nodes and  $m = 75$  samples,  $\epsilon_+ = 5 \times 10^{-3}$  and  $\epsilon_- = 5 \times 10^{-2}$ , for the 25 possible combinations of input  $\epsilon_+$  and  $\epsilon_-$  in the following ranges:  $\epsilon_+ = (3, 4, 5, 6, 7) \times 10^{-3}$  and  $\epsilon_- = (3, 4, 5, 6, 7) \times 10^{-2}$ .*

**Results (Supplementary Table 4 and Supplementary Table 5):** By looking at the performance with respect to the different combinations of  $\epsilon_+$  and  $\epsilon_-$  provided as input to the algorithms, we unexpectedly do not observe noteworthy variations, for both the algorithms. This result indicates that, if the value of noise provided as input to the algorithms is close to the real value (i.e., within a reasonable range), the inference accuracy is not remarkably perturbed. As a consequence, one might question about the usefulness of the usually computationally expensive techniques used for the inference of noise models, as done, for instance, by SCITE. We leave some further comments on this topic to the main text.

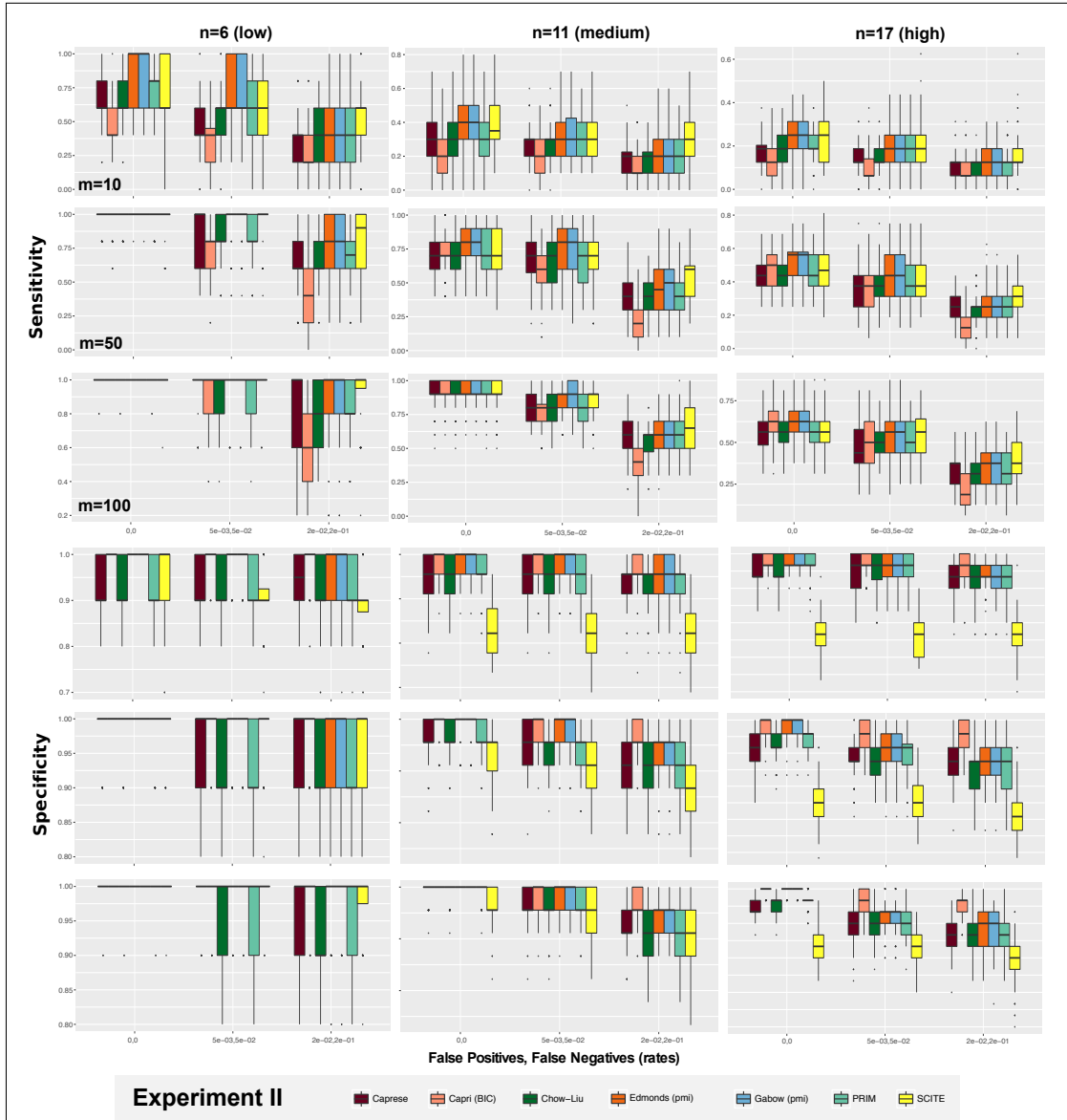
## 4.2 Confounding Factors

Here true variables are mixed to random 0/1 variables, totally unrelated to the progression. This could be a simple model of uncertainty in the calling, where we over-call variants that are not true related to the progression at a certain error rate.

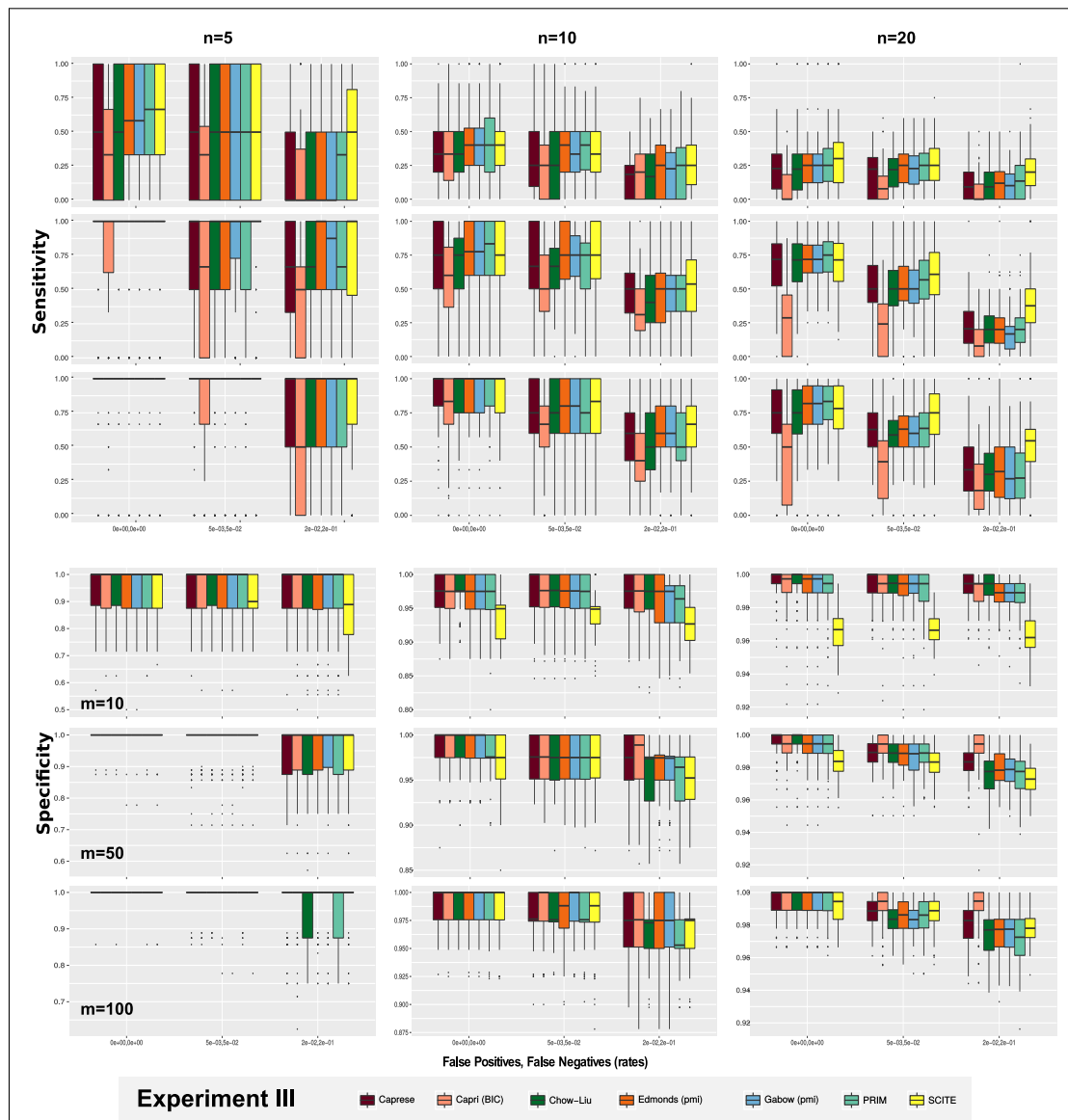
**Experiment V.** *We use data from Experiment II; to each dataset we add random binary columns. A column is a repeated sampling of a biased coin, with bias uniformly sampled among the marginals of all events.  $n \times 10\%$  random columns are inserted per dataset, where  $n$  is the true model size.*

**Results (Supplementary Figure 10):** Surprisingly, the results of this experiment reflects those of Experiment II, with minor differences in the performance of the various algorithms in the different settings. The overall performance is good, at least with sufficiently large datasets and sufficiently small levels of noise. Also in this case, SCITE tends to overfit, especially with larger models and small datasets.

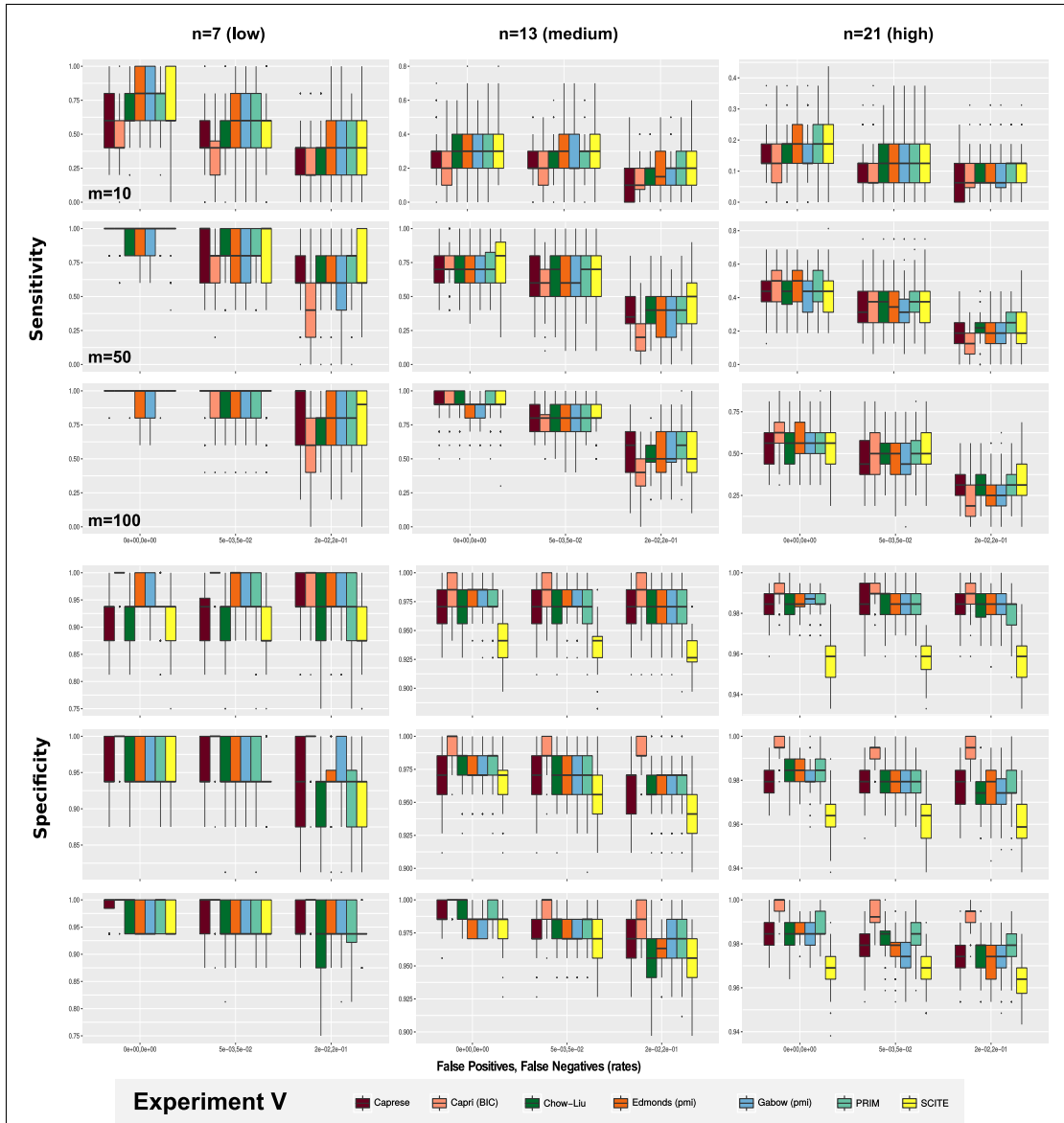




Supplementary Figure 8: Experiment II, (branching evolution, fixed topologies, SCS data). All the algorithms are tested on datasets generated from the phylogenetic trees shown in Supplementary Figure 7. Three incremental level of unbalanced noise in the data are assumed:  $\epsilon_+ = \epsilon_- = 0$  (noise-free),  $\epsilon_+ = 5 \cdot 10^{-3}$ ,  $\epsilon_- = 5 \cdot 10^{-2}$  and  $\epsilon_+ = 2 \cdot 10^{-2}$ ,  $\epsilon_- = 2 \cdot 10^{-1}$ . We test distinct sample set sizes ( $n = 10, 50, 100$ ) and 100 distinct datasets for each case, reporting the distributions of sensitivity and specificity.



Supplementary Figure 9: Experiment III. (branching evolution, random topologies, SCS data). The algorithms are tested on SCS data generated from 100 random tree topologies, with  $n = 5, 10, 20$  clones. As in Experiment II, three levels of noise ( $\epsilon_+$ ,  $\epsilon_-$ ) and three sample sizes ( $m$ ) are tested.



Supplementary Figure 10: Experiment V. (confounding factors, fixed topologies, SCS data). We add  $n \times 10\%$  random (0/1) columns to the SCS data generated from the trees in Supplementary Figure 7. We test three levels of noise ( $\epsilon_+ = \epsilon_- = 0$ ,  $\epsilon_+ = 5 \cdot 10^{-3}$ ,  $\epsilon_- = 5 \cdot 10^{-2}$ ,  $\epsilon_+ = 2 \cdot 10^{-2}$ ,  $\epsilon_- = 2 \cdot 10^{-1}$ ), and three sample sizes ( $m = 10, 50, 100$ ).

### 4.3 Multiple Independent Trajectories

In this case the signal that we detect in the data is composed from different true signals, one per population of cells. So, we need to infer a forest with a number of trees equal to the number of different progressions, which it seems reasonable to assume to be low, e.g., below 5.

**Experiment VI.** *We extend the sampling strategy in Experiment III to account for forests with fixed total number of nodes, i.e.,  $n = 20$ . We perform the same procedure of that experiment.*

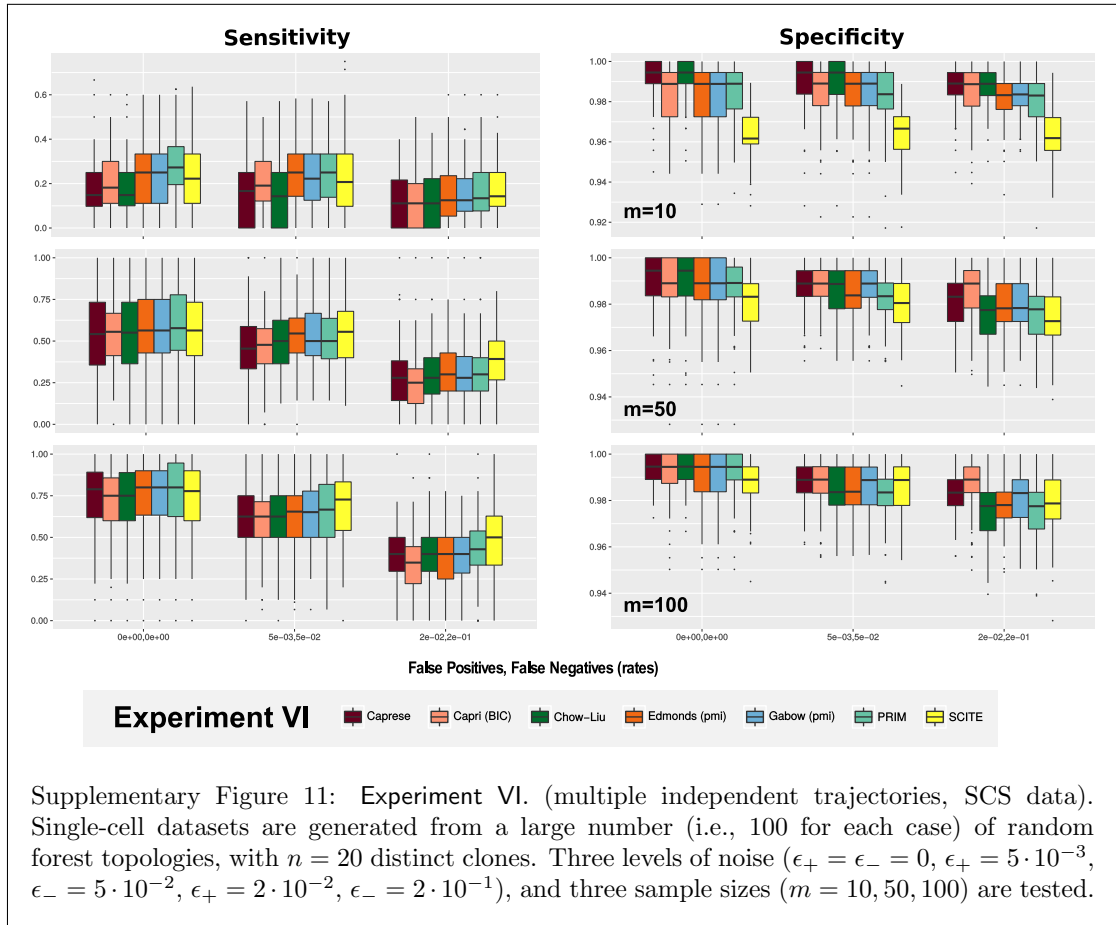
**Results (Supplementary Figure 11):** All the algorithms display a very low sensitivity with small datasets (with 20% median value with  $m = 10$  samples), remarkably increasing the performance with larger datasets (median values around 75% with  $m = 100$  samples in the noise-free case). Gabow, Edmond and CAPRESE show a good tradeoff between sensitivity and specificity, displaying a good and similar performance, whereas SCITE confirms the tendency to overfit for small datasets, yet being the most robust algorithm against noise in the data.

### 4.4 Inference with missing data

In addition to the false positives/negatives introduced in the data via allelic dropouts and false alleles, unobserved or missing data points represent another major problem when dealing with single-cell sequencing data. In the early works, around 60% of the data were missing due to the low quality of the sequencing technique. Even though the technology has remarkably improved during the last few years, leading to more reliable and usable data, we here investigate the influence of missing data on the inference, with respect to the considered algorithms. In particular, we performed simulated experiments with a specific generative topology and with different amounts of missing data, ranging from 10% to 40%, analyzing the variation in the inference accuracy.

**Experiment VII** *In order to evaluate the impact of missing data on the inference accuracy, we chose 20 benchmark single-cell datasets generated from the Medium phylogenetic tree in Supplementary Figure 7, with  $n = 11$  nodes and  $m = 75$  samples. 10 of these datasets were generated with  $\epsilon_+ = \epsilon_- = 0$ , and the remaining 10 datasets with (ii)  $\epsilon_+ = 0.005$ ,  $\epsilon_- = 0.05$ . For each of the 20 datasets we generated 5 further datasets, with the following ratio of randomly included missing entries:  $r = (0, 0.1, 0.2, 0.3, 0.4)$ , for a total of 100 distinct datasets. As SCITE naturally deals with datasets with missing data, we performed the inference with no further parameters. Instead, in order to perform the reconstruction with the remaining algorithms, we followed this procedure. For each one of the 80 datasets with missing data (we did not consider the case with  $r = 100$ ), we filled the missing entries via a classical Expectation Maximization (EM) algorithm, and we repeated this step to create 100 complete datasets (for each incomplete datasets). We then performed the inference with all the algorithms on all the 100 datasets in each case, selecting the model with the best likelihood score, which was then used in the performance assessment.*

**Results (Supplementary Figure 12):** As one can see in Supplementary Figure 12, the performance of all the algorithms is profoundly affected by the presence of missing data, both in the noisy and in the noise-free cases. SCITE displays an overall more robust sensitivity than the other techniques, yet in spite of a worse specificity, which would point at a tendency toward overfitting also in this



scenario. As expected, the performance of all the techniques is significantly better in the noise-free case and, in general, is maintained at acceptable levels up to values of missing data around 20%/30% according to the cases.

## 5 Detailed tests with multi-region bulk-sequencing data

As we did for SCS data, we here present the results of detailed comparative tests of with multi-region sequencing data. The analyses are organized as for SCS data.

### 5.1 Branching evolution

**Experiment II-MR** *Here we reproduce Experiment II in the case of multi-region data, and sample the polyclonal topologies shown in Supplementary Figure 7, with symmetric noise rates ( $\epsilon_- = \epsilon_+$ ). We compare the boxplot performance from 100 tests.*

**Results (Supplementary Figure 13):** The accuracy of most algorithms is good in all the scenarios. They all reach high values of specificity, whereas satisfactory values of sensitivity are observed only with combination of sufficiently large datasets and sufficiently low noise. As expected, the overall performance worsens with larger and more complex generative models.

In this case **Gabow** and **Edmond** display the best efficiency in retrieving both the true positives and negatives, **Edmond** being slightly better in a certain number of parameter settings. Conversely, **SCITE** shows the worst performance, especially with small datasets and low levels of noise, yet proving a certain robustness to the increase in the noise level. **CAPRI** displays very good values of specificity even with these data type, yet most likely due to its regularization.

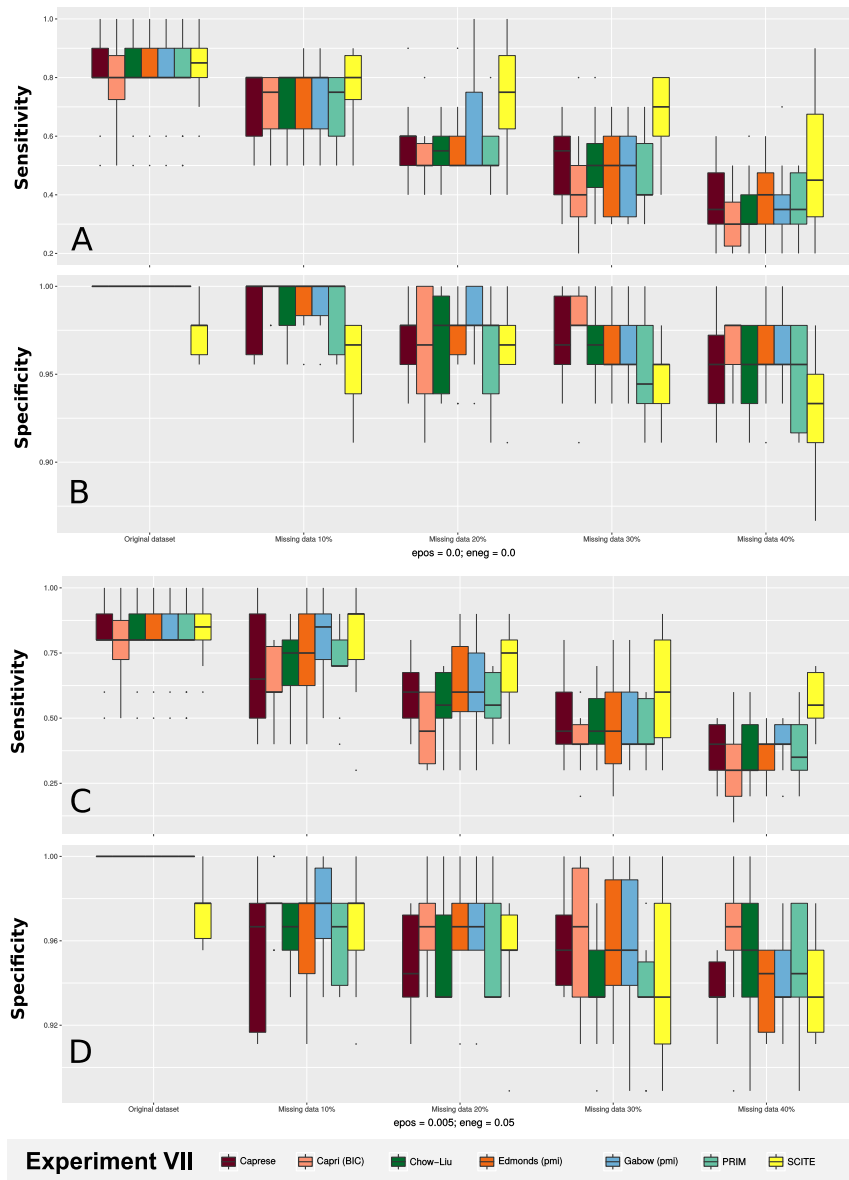
**Experiment III-MR** *This experiment reproduces Experiment III with multi-region data, hence sampling the datasets from 100 randomly generated topologies with variable number of nodes.*

**Results (Supplementary Figure 14):** The results of this experiment resemble Experiment III: overall good performance is observed, yet with low sensitivity with small datasets and noisy data. **Gabow** and **Edmond** consistently display optimal and very similar trends, with **Edmond** showing a better performance in a slightly larger number of settings. **SCITE** confirms to be less accurate with multi-region data, especially with small datasets, even when the level of noise is low. We remark that we did not include an experiment analogous to **Experiment IV** because with symmetrical noise rates we do not expect significant differences in accuracy.

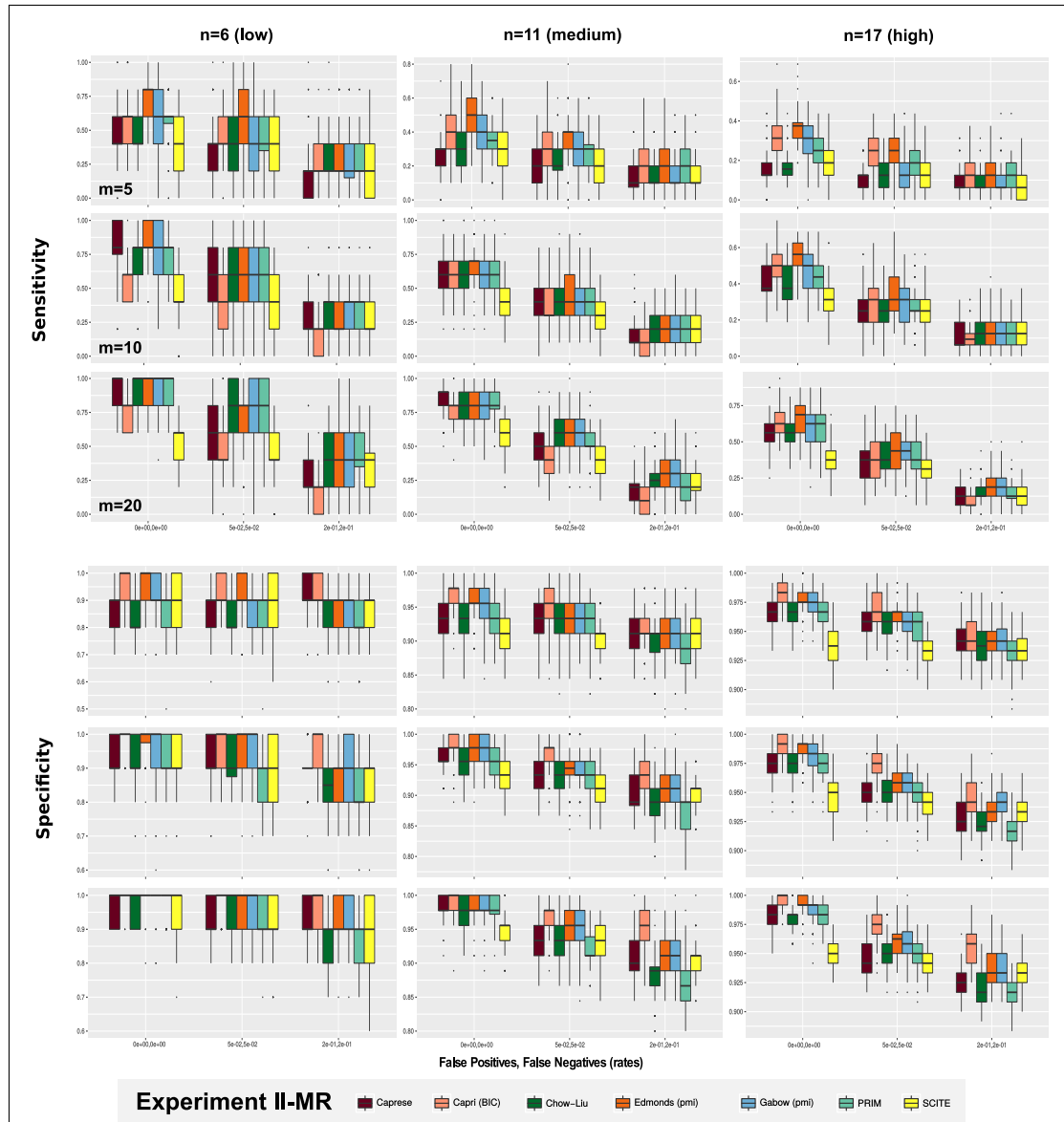
### 5.2 Confounding factors

**Experiment V-MR** *We reproduce Experiment V with multi-region data augmented with  $n \times 10\%$  random columns. We use the three topologies shown in Supplementary Figure 7.*

**Results (Supplementary Figure 15):** The results are in accordance with those of the analogous SCS experiment, with an expected overall decrease of accuracy due to the introduction of spuriously correlated events. **Edmond** is the most accurate algorithm, slightly improving over **Gabow**; **SCITE** seems less efficient in retrieving both the true and the false relations, especially with small datasets and/ or low noise levels.

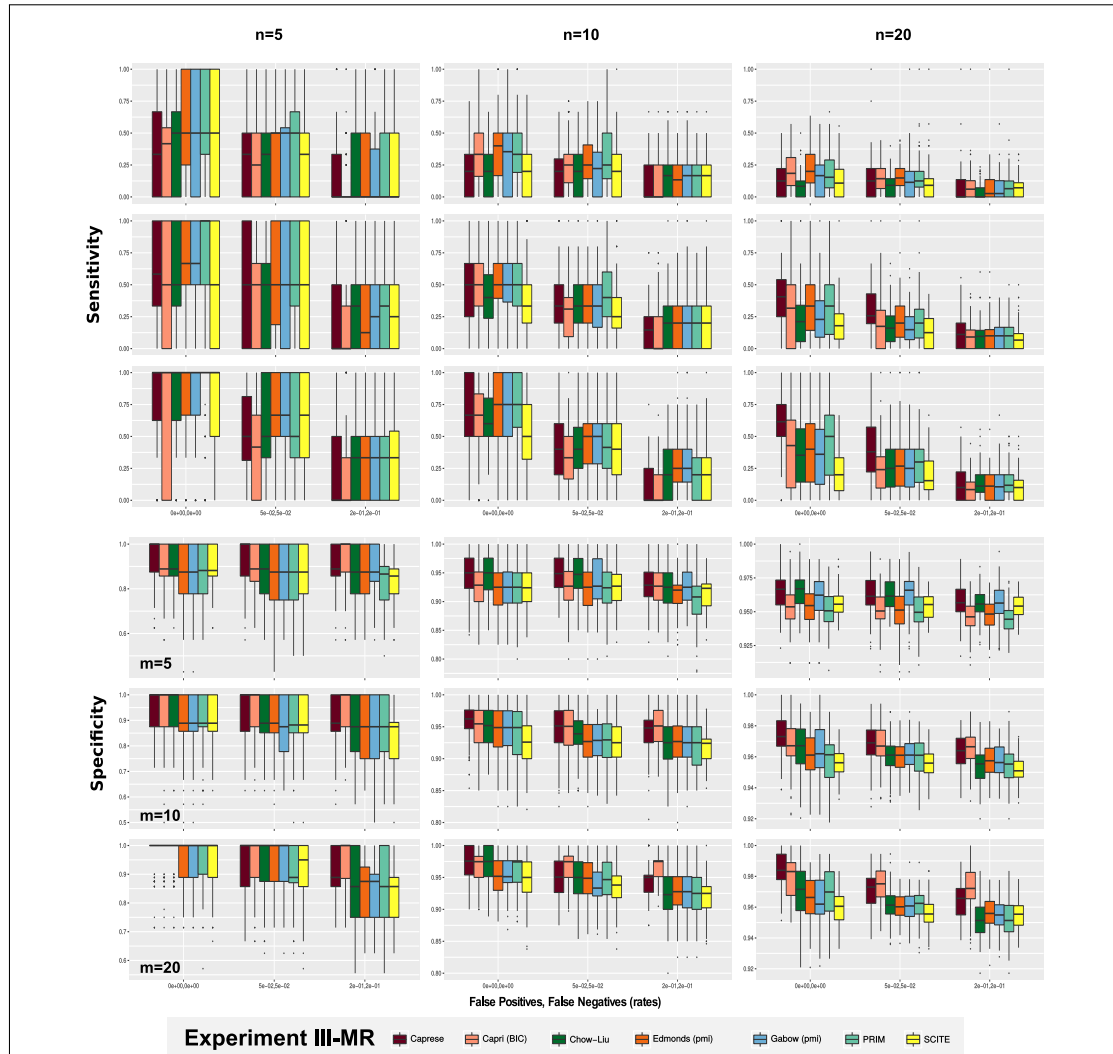


Supplementary Figure 12: Experiment VII. (missing data, SCS data). Sensitivity and specificity for with different proportions of missing entries, i.e.,  $r = (0, 0.1, 0.2, 0.3, 0.4)$ , and different levels of noise: (i)  $\epsilon_+ = \epsilon_- = 0$  and (ii)  $\epsilon_+ = 0.005$ ,  $\epsilon_- = 0.05$ . The original dataset is generated from the medium tree in Supplementary Figure 7, with  $n = 11$  nodes and  $m = 75$  samples.

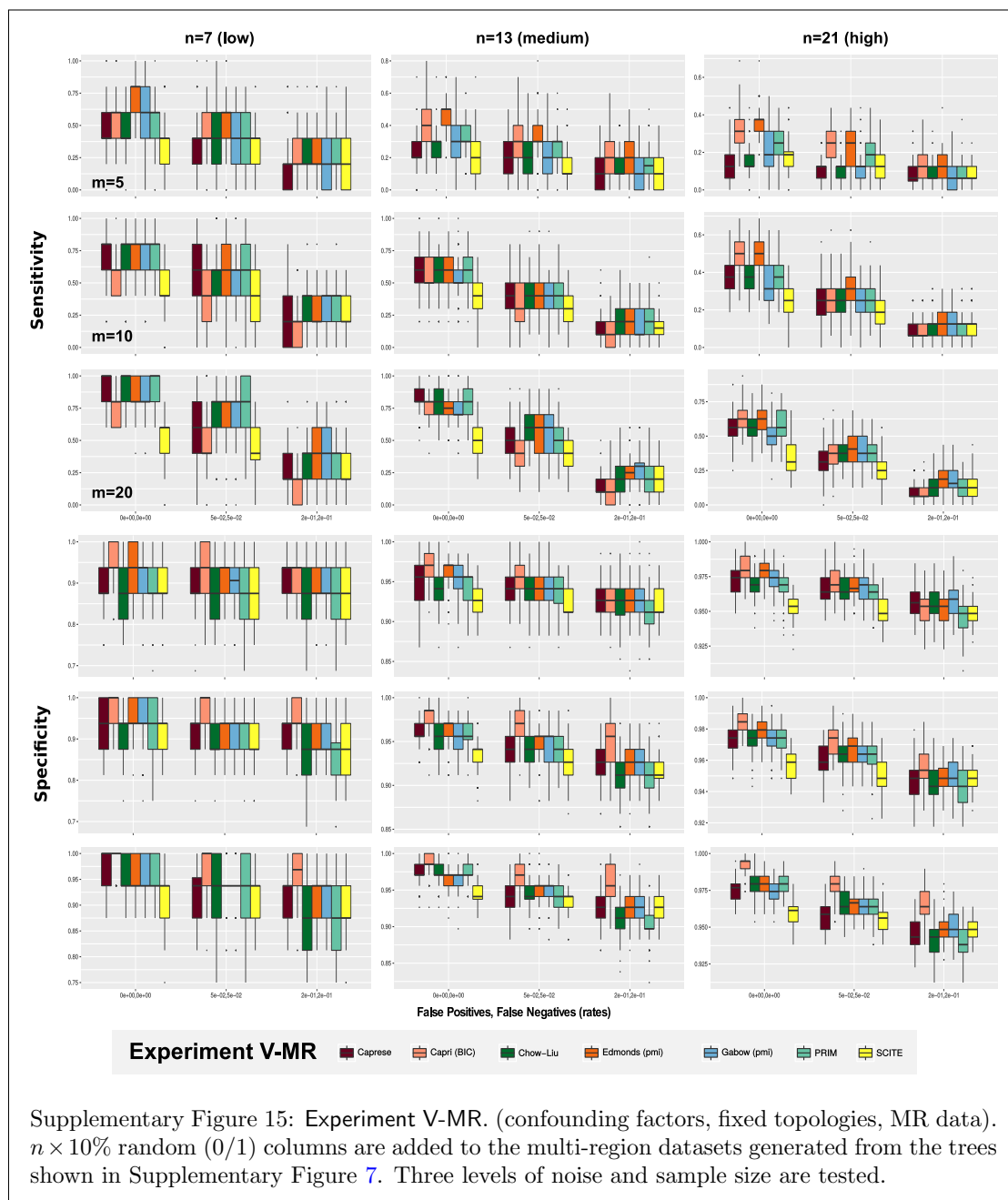


Supplementary Figure 13: Experiment II-MR. (branching evolution, fixed topologies, MR data). All algorithms are tested on datasets generated from the phylogenetic trees shown in Supplementary Figure 7, where we simulate multi-region data. Three levels of noise ( $\epsilon_+ = \epsilon_- = 0.0, 0.05, 0.2$ ), and three sample sizes ( $m = 5, 10, 20$ ) are tested.





Supplementary Figure 14: Experiment III-MR (branching evolution, random topologies, MR data). The algorithms are tested on multi-region datasets generated from a number of random tree topologies, with  $n = 5, 10, 20$  clones (100 distinct topologies for each case). Three levels of noise ( $\epsilon_+ = \epsilon_- = 0.0, 0.05, 0.2$ ), and three sample sizes ( $m = 5, 10, 20$ ) are tested.



Supplementary Figure 15: Experiment V-MR. (confounding factors, fixed topologies, MR data).  $n \times 10\%$  random (0/1) columns are added to the multi-region datasets generated from the trees shown in Supplementary Figure 7. Three levels of noise and sample size are tested.

### 5.3 Multiple Independent Trajectories

**Experiment VI-MR** *We reproduce Experiment VI with multi-region data, and with datasets sampled from random forests (see Supplementary Figure 3).*

**Results (Supplementary Figure 16):** Gabow, Edmond and CAPRESE appear to be the most accurate algorithms in this scenario. The former achieves the best sensitivity and specificity in most settings. Prim is very efficient in retrieving the true relations in many cases, especially with low levels of noise, yet presenting a certain tendency toward overfitting. SCITE seems less accurate in most settings.

## 6 Parameters settings, computation time and scalability

### 6.1 Parameter Settings

$n$  : **number of nodes** (i.e, genomic alterations/ clones).

We use

$$n = 5, 10, 15, 20$$

when we sample random models. In random tests, 100 trees are generated for each configuration of  $n$  and  $m$  (see below), and one dataset per tree is sampled. In some tests, we fix  $n$  to 6, 11 and 17 (Supplementary Figure 7); we specify in the experiment description if that is the case.

$m$  : **number of samples** (i.e., cells, or regions sequenced).

When we perform a single-cell sampling, we scan the values

$$m = 10, 25, 50, 75, 100 .$$

When we perform a multi-region sampling, we scan values in line with a reasonable number of biopsies that could be extracted from a solid tumor

$$m = 5, 7, 10, 20, 50 .$$

$c$  : **number of signals from single-clones in a multi-region experiment.**

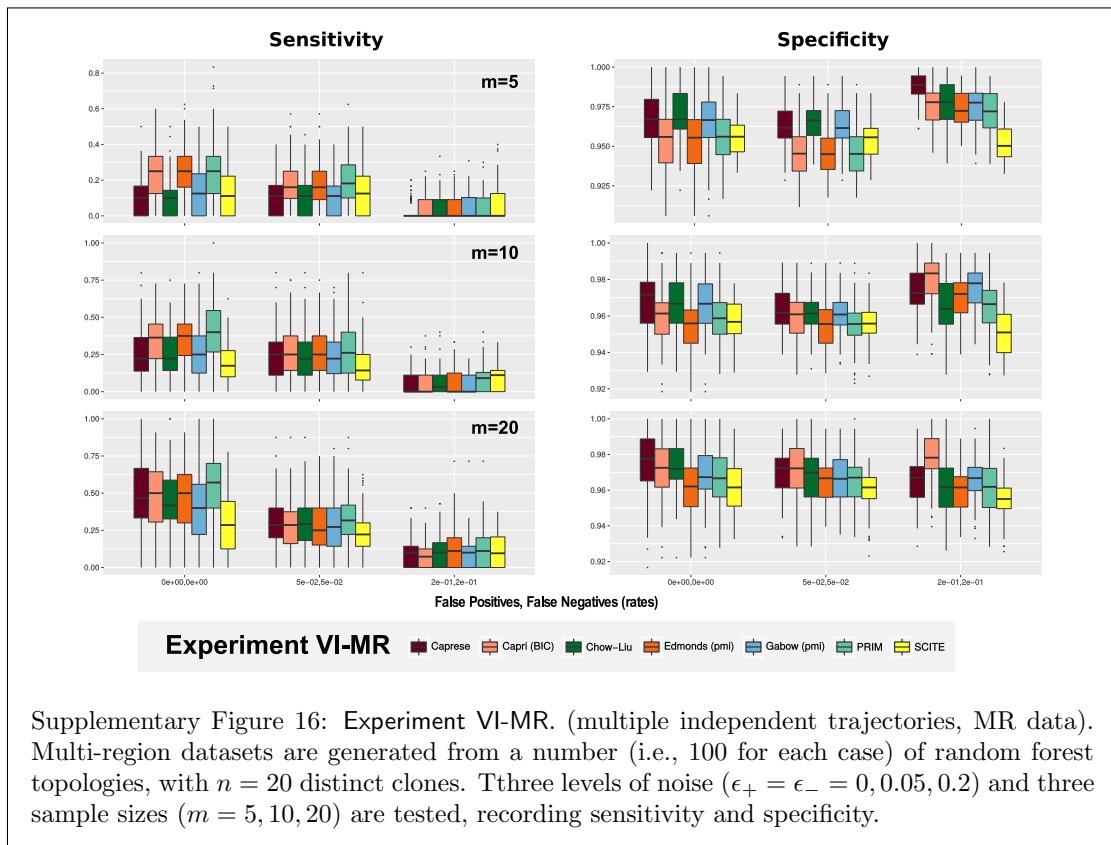
When we perform a multi-region sampling, we set the values

$$c = 3, 5, 8 .$$

for the fixed topologies in Supplementary Figure 7, and

$$c = \frac{n}{2}$$

otherwise.



$\epsilon_+/\epsilon_-$  : **rates of FPs/FNs in data**, for the observed genotypes.

In single-cell sequencing we assume these to be

$$(\epsilon_+, \epsilon_-) = (0, 5, 10, 15, 20, 25, 30, 35) \times (10^{-3}, 10^{-2}).$$

This corresponds to pairs of equal value that differ for an order of magnitude, e.g., ( $\epsilon_+ = 0.015, \epsilon_- = 0.15$ ), consistently with the observation that false negative rates in single-cell data are much higher than false positives ones. Such values correspond to an overall error rate that is  $2 \times \epsilon_+$  and  $2 \times \epsilon_-$ . For multi-region sequencing, these errors are symmetric

$$(\epsilon_+, \epsilon_-) = (0, 5, 10, 15, 20, 25, 30, 35) \times (10^{-2}, 10^{-2}).$$

*topology* : **model structure** used according to the working scenarios (Supplementary Figure 3).

This is either a tree, a forest or a DAG.

*probabilities* : **conditional probability tables** (CPTs), and **marginals** of a model.

When these are sampled at random we impose the constraint that for any pair of variables  $X$  and  $Y$  it holds

$$p(X | Y) \in [0.6, 0.9],$$

and for any marginal  $p(X) > 0.001$ . These values seem reasonable to avoid the introduction of biases in the sampling process. In some cases we assigned fixed values to the CPTs, which we report in the corresponding figures (e.g., in Supplementary Figure 7).

$p_\star = 0.05$  :  **$\alpha$ -level of the Mann-Whitney test** (p-value).

## 6.2 Computation time and scalability

To assess and compare the computation time of the distinct techniques we used the Medium phylogenetic tree in Supplementary Figure 7 as generative topology, with  $n = 11$  nodes,  $m = 75$  samples,  $\epsilon_+ = 0.005$ ,  $\epsilon_- = 0.05$ , and we repeated the inference for 100 distinct experiments, on a single core of a Lenovo Thinkpad t430s with an Intel i7 3520M 4-core 2.90GHz and 16Gb Ram.

In Supplementary Table 6 we see that CAPRESE is the fastest algorithm, because it does not bootstrap the data. It is followed by Prim, Gabow, Edmond, CAPRI and Chow-Liu, with almost identical running time ( $7\times$  slower than CAPRESE). SCITE is remarkably slower (i.e.,  $25\times$  slower than CAPRESE and more than  $3\times$  slower than the group of PRIM), whereas OncoNEM has the worst performance (i.e.,  $300\times$  slower than CAPRESE, around  $40\times$  slower than CAPRI, and  $12\times$  slower than SCITE). For these reasons, we could not include also OncoNEM in more extensive experiments.

In order to assess TRAIT's scalability with increasingly larger single-cell datasets, we generated 100 random branching evolution topologies (as in Experiment III and Supplementary Figure 9), with  $n = 20$  nodes,  $\epsilon_+ = 0.005$ ,  $\epsilon_- = 0.05$  and different values of sample size:  $m \in (100, 500, 1000, 5000, 10000, 15000, 20000)$ . We then timed both EDMONDS and CHOW-LIU, and evaluated performance. In Supplementary Table 7 we show median values and standard deviation for each distinct experimental settings. Simulations were performed on a Quad Core pc with Intel i7 - 8 thread 3.5 GHz and 16Gb Ram. As one can see from the table, CHOW-LIU displays better median sensitivity with smaller sample size than EDMONDS, which in turn shows better median specificity. Both the algorithms display an approximately linear increase of the computational time with respect to the number of samples, and even for extremely large datasets (i.e., 20000 single cells) the median execution time is around 22 seconds per experiment.

## 7 Case studies

In addition to the Main Text, we show in Supplementary Figures 17 and 18 the inference from the triple-negative breast cancer SCS data, and in Supplementary Figure 20 the same for the colorectal cancer data. In Supplementary Figure 21 we show the fit with SCITE .

## 8 Noise model

Derivation of the noise model for both marginal and joint probabilities.

### Marginal Probabilities

Let us call  $\epsilon_+$  the probability of observing 1 when we had 0 (false positive) and  $\epsilon_-$  the other way around (false negative). We remark that we assume these probability to be strictly in  $[0, 0.5)$  with value 0.5 representing totally random entries. Then, for any event  $\mathbf{x}_i$ , we can write the expectation of the probability of observing it (here with the notation  $n_i$ ), given its theoretical probability  $p(\mathbf{x}_i)$  as follow.

$$n_i = p(\mathbf{x}_i) \cdot [1 - \epsilon_-] + [1 - p(\mathbf{x}_i)] \cdot \epsilon_+ ,$$

and with some rearrangements,

$$\begin{aligned} n_i &= p(\mathbf{x}_i) - p(\mathbf{x}_i) \cdot \epsilon_- + \epsilon_+ - p(\mathbf{x}_i) \cdot \epsilon_+ , \\ n_i &= p(\mathbf{x}_i) \cdot [1 - \epsilon_+ - \epsilon_-] + \epsilon_+ , \end{aligned}$$

from which, with  $(\epsilon_+, \epsilon_-) \in [0, 0.5)$ ,

$$p(\mathbf{x}_i) = \frac{n_i - \epsilon_+}{1 - \epsilon_+ - \epsilon_-} .$$

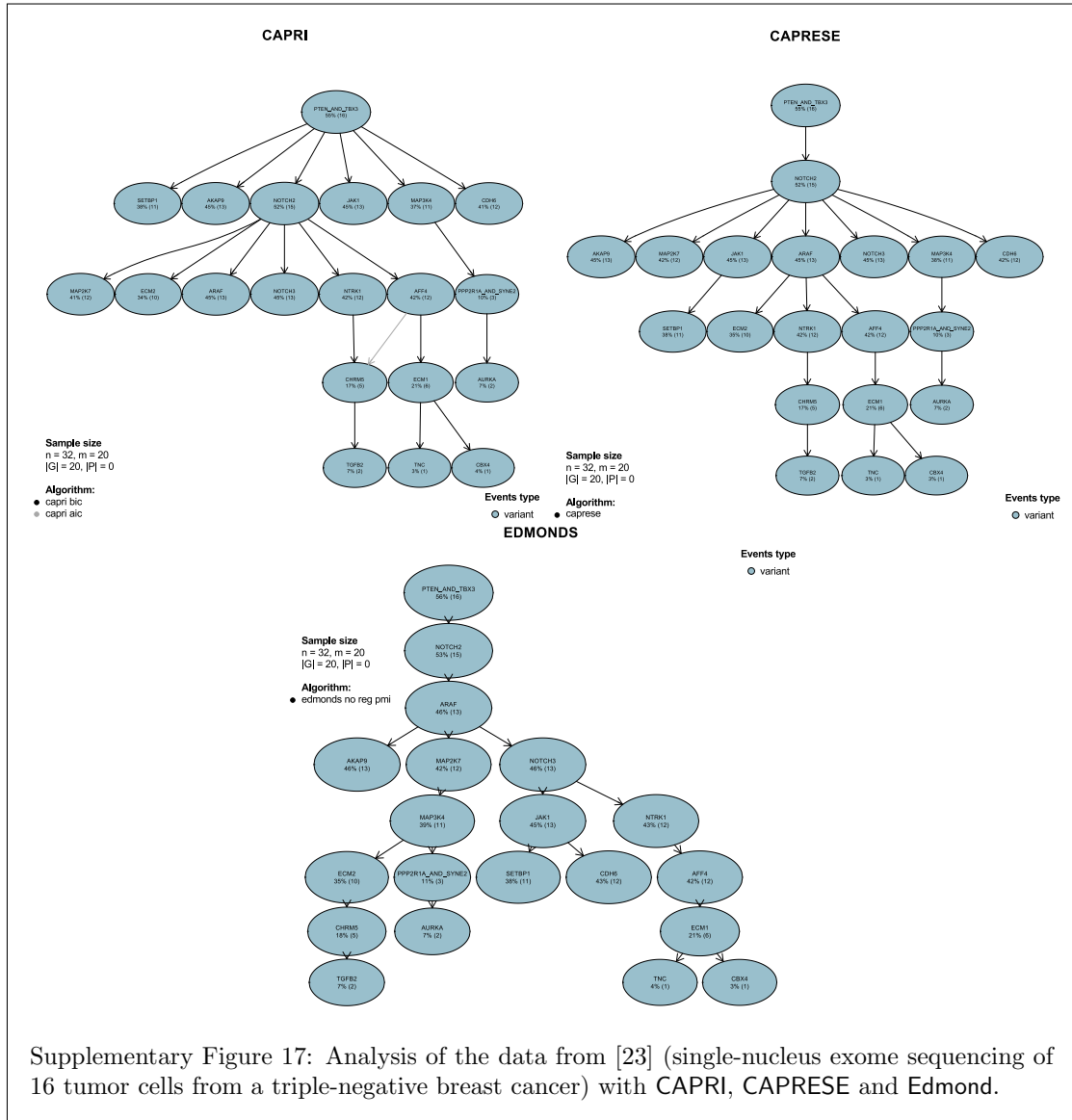
### Joint probabilities

Let us now consider the theoretical joint probability  $p(\mathbf{x}_{i,j})$  (in what follow also called  $p(\mathbf{x}_i, \mathbf{x}_j)$  to make the elements of the probability explicit) of any two pair of events and the respective observed marginal and joint probabilities  $n_i$ ,  $n_j$  and  $n_{i,j}$ . Then, the expectation of  $n_{i,j}$  can be written as follow.

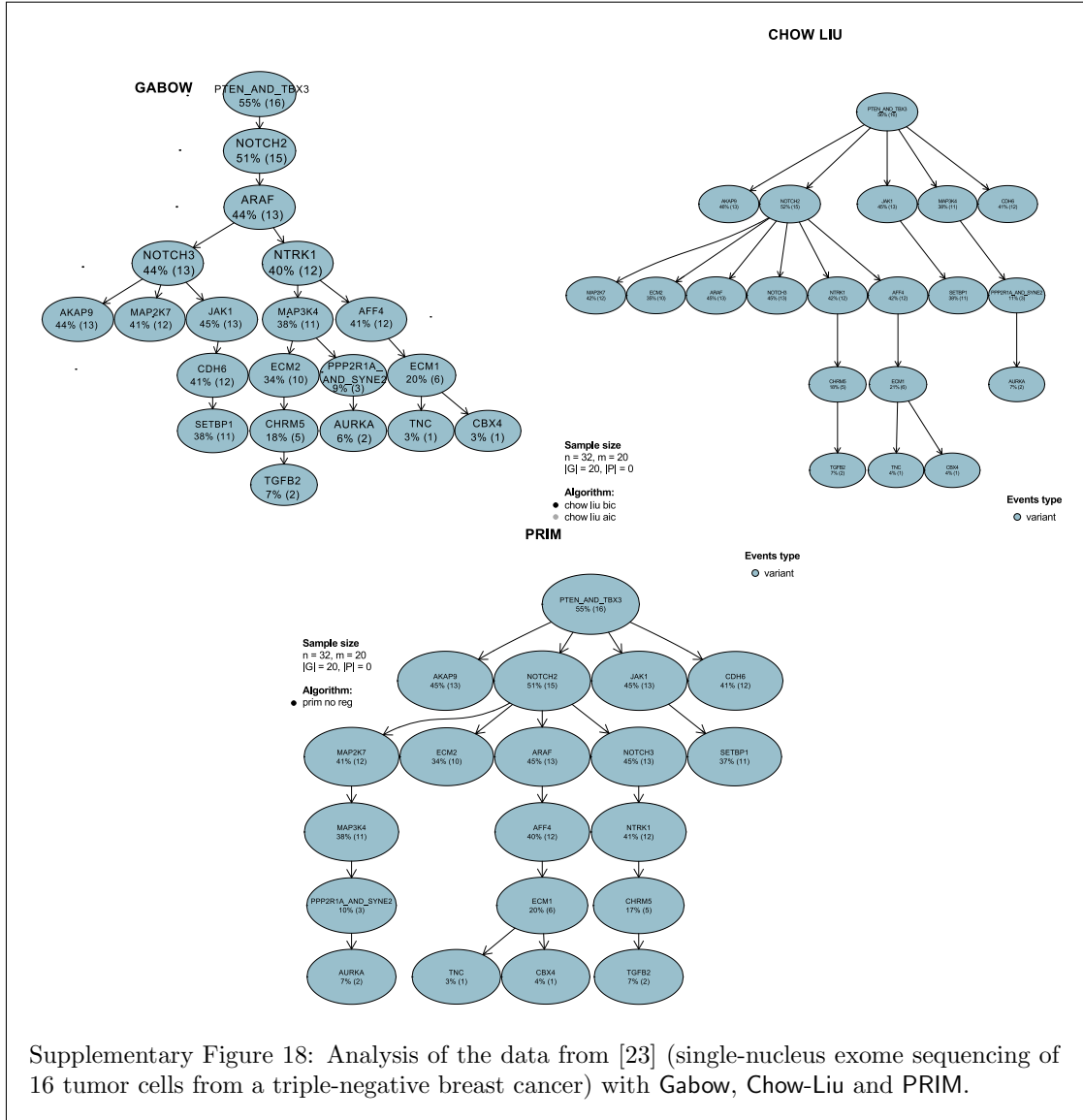
$$\begin{aligned} n_{i,j} &= p(\mathbf{x}_i, \mathbf{x}_j) \cdot [1 - \epsilon_-] \cdot [1 - \epsilon_-] \\ &\quad + p(\mathbf{x}_i, \overline{\mathbf{x}}_j) \cdot [1 - \epsilon_-] \cdot \epsilon_+ \\ &\quad + p(\overline{\mathbf{x}}_i, \mathbf{x}_j) \cdot \epsilon_+ \cdot [1 - \epsilon_-] \\ &\quad + p(\overline{\mathbf{x}}_i, \overline{\mathbf{x}}_j) \cdot \epsilon_+ \cdot \epsilon_+ , \end{aligned}$$

and being,

$$\begin{aligned} p(\mathbf{x}_i, \overline{\mathbf{x}}_j) &= p(\mathbf{x}_i) - p(\mathbf{x}_i, \mathbf{x}_j) , \\ p(\overline{\mathbf{x}}_i, \mathbf{x}_j) &= p(\mathbf{x}_j) - p(\mathbf{x}_i, \mathbf{x}_j) , \\ p(\overline{\mathbf{x}}_i, \overline{\mathbf{x}}_j) &= 1 - p(\mathbf{x}_i) - p(\mathbf{x}_j) + p(\mathbf{x}_i, \mathbf{x}_j) , \end{aligned}$$



Supplementary Figure 17: Analysis of the data from [23] (single-nucleus exome sequencing of 16 tumor cells from a triple-negative breast cancer) with CAPRI, CAPRESE and Edmond.



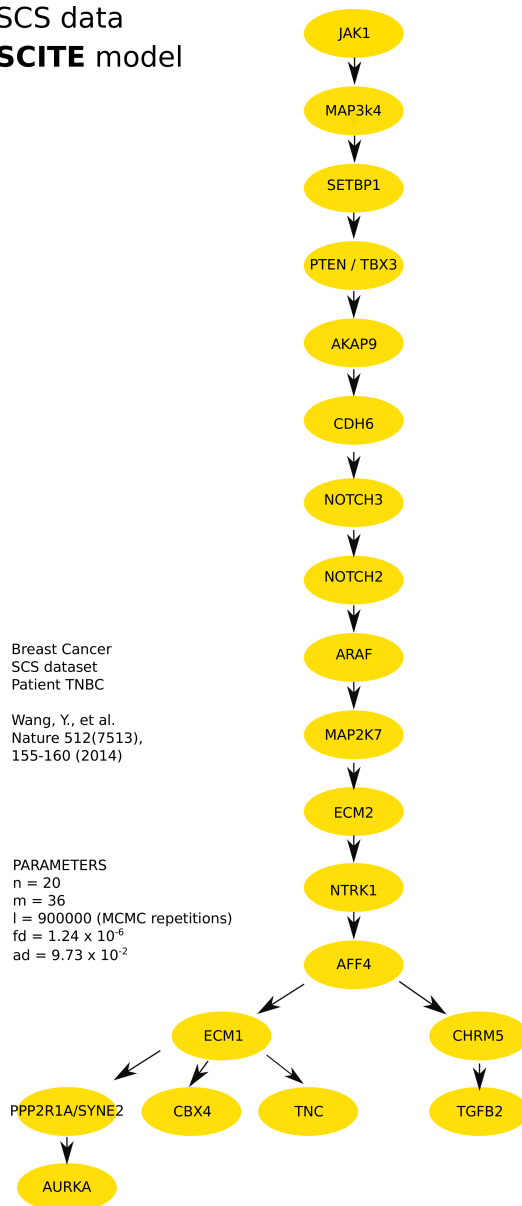
Supplementary Figure 18: Analysis of the data from [23] (single-nucleus exome sequencing of 16 tumor cells from a triple-negative breast cancer) with Gabow, Chow-Liu and PRIM.

with some rearrangements,

$$\begin{aligned}
 n_{i,j} &= p(\mathbf{x}_i, \mathbf{x}_j) \cdot (1 + \epsilon_+^2 + \epsilon_-^2 + 2 \cdot \epsilon_+ \cdot \epsilon_- - 2 \cdot \epsilon_+ - 2 \cdot \epsilon_-) \\
 &\quad + [p(\mathbf{x}_i) + p(\mathbf{x}_j)] \cdot \epsilon_+ \cdot [1 - \epsilon_+ - \epsilon_-] + \epsilon_+^2, \\
 n_{i,j} &= p(\mathbf{x}_i, \mathbf{x}_j) \cdot (1 - \epsilon_+ - \epsilon_-)^2 + [p(\mathbf{x}_i) + p(\mathbf{x}_j)] \cdot \epsilon_+ \cdot [1 - \epsilon_+ - \epsilon_-] + \epsilon_+^2, \\
 n_{i,j} &= p(\mathbf{x}_i, \mathbf{x}_j) \cdot (1 - \epsilon_+ - \epsilon_-)^2 + \frac{n_i + n_j - 2 \cdot \epsilon_+}{1 - \epsilon_+ - \epsilon_-} \cdot \epsilon_+ \cdot [1 - \epsilon_+ - \epsilon_-] + \epsilon_+^2, \\
 n_{i,j} &= p(\mathbf{x}_i, \mathbf{x}_j) \cdot (1 - \epsilon_+ - \epsilon_-)^2 + (n_i + n_j) \cdot \epsilon_+ - 2 \cdot \epsilon_+^2 + \epsilon_+^2,
 \end{aligned}$$



SCS data  
SCITE model

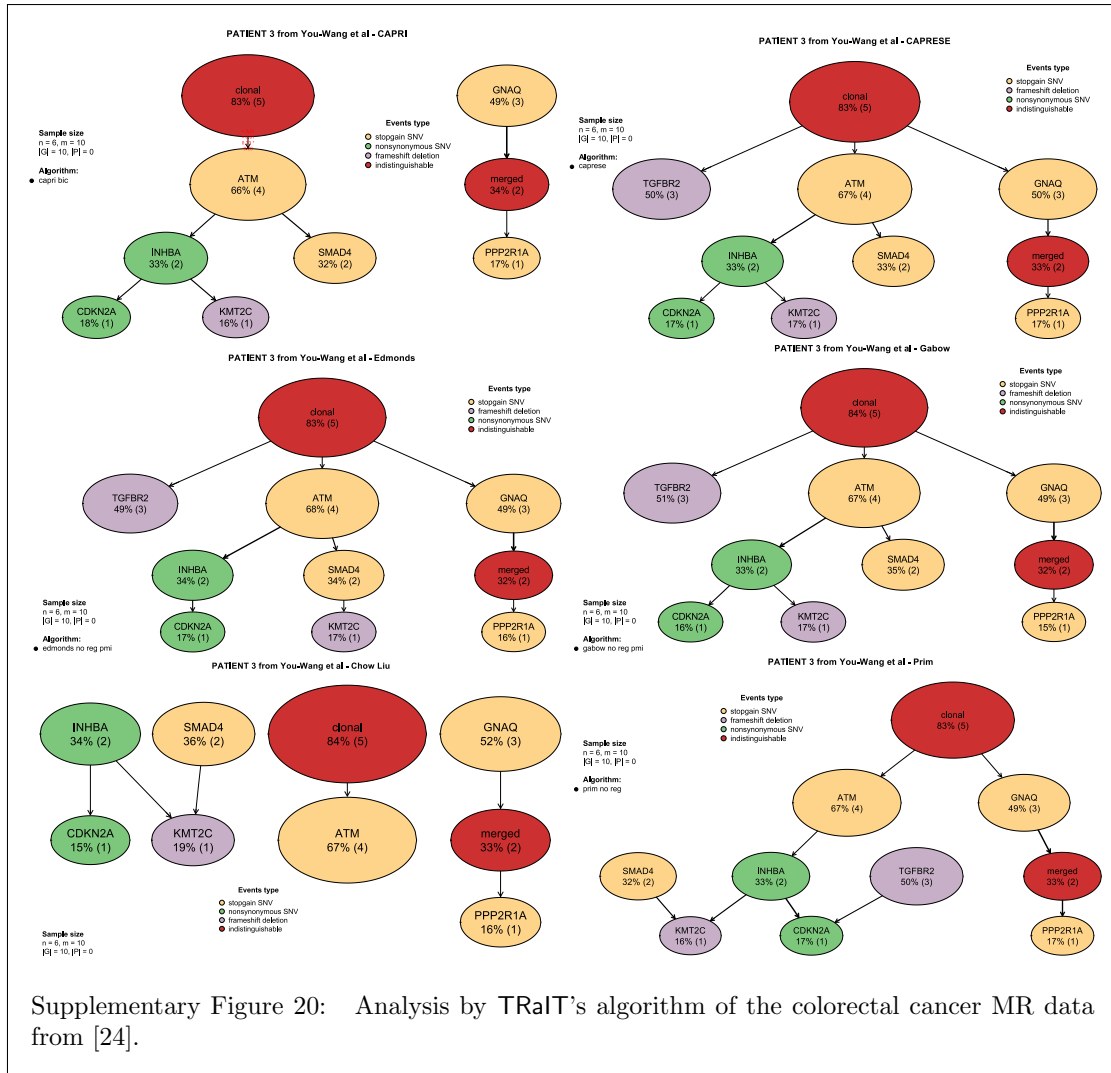


Breast Cancer  
SCS dataset  
Patient TNBC

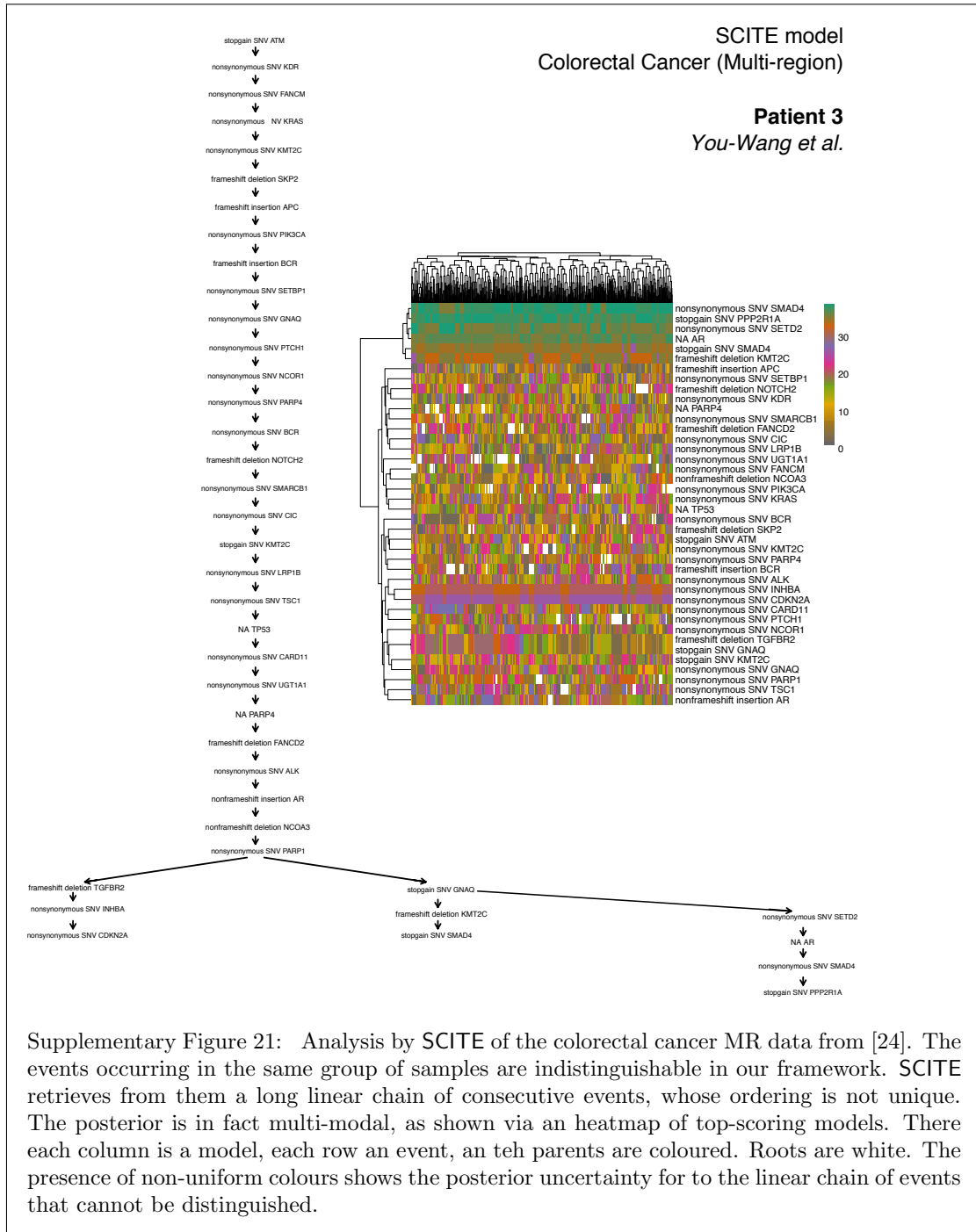
Wang, Y., et al.  
Nature 512(7513),  
155-160 (2014)

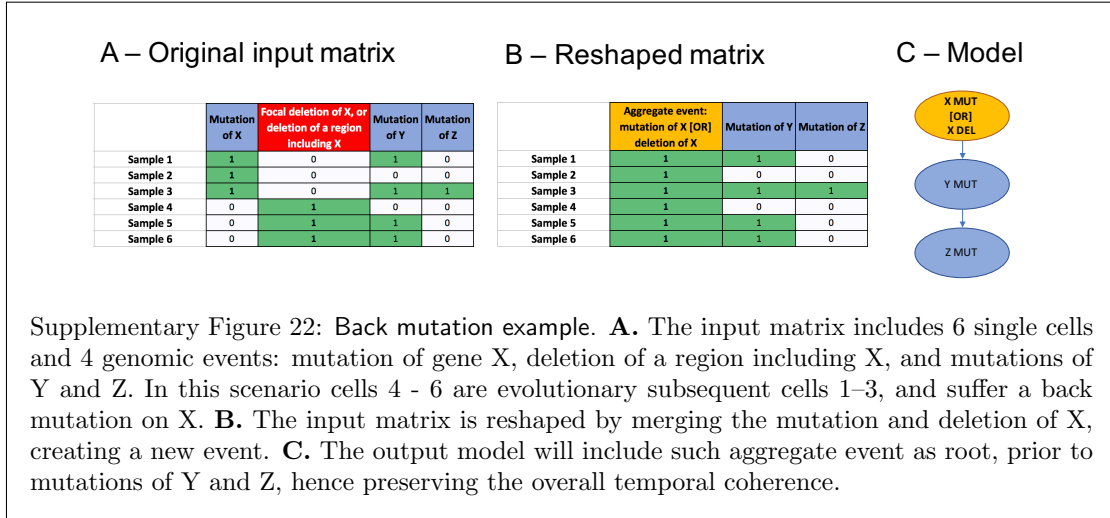
PARAMETERS  
n = 20  
m = 36  
l = 900000 (MCMC repetitions)  
fd =  $1.24 \times 10^{-6}$   
ad =  $9.73 \times 10^{-2}$

Supplementary Figure 19: Analysis of the data from [23] (single-nucleus exome sequencing of 16 tumor cells from a triple-negative breast cancer) with SCITE. False discovery rate of  $1.26 \times 10^{-6}$  and allelic dropout of  $9.73 \times 10^{-2}$  are provided as input parameters. Posterior estimates are computed with 900.000 Montecarlo steps, and 10000 equivalent-scoring trees returned. Here we show one of the top-scoring.



Supplementary Figure 20: Analysis by TRaIT's algorithm of the colorectal cancer MR data from [24].





from which, with  $(\epsilon_+, \epsilon_-) \in [0, 0.5)$ ,

$$p(\mathbf{x}_i, \mathbf{x}_j) = \frac{n_{i,j} - \epsilon_+ \cdot (n_i + n_j - \epsilon_+)}{(1 - \epsilon_+ - \epsilon_-)^2}.$$

## 9 Modeling back mutations

Our framework does not explicitly account for *back mutations*. These confound the inference when a previously acquired genomic alteration is lost during the evolutionary history of a tumor, due, e.g., to loss of heterozygosity or general chromosomal deletions. In phylogenetic jargon this is a violation of the no-back mutation assumption, and cannot be handled in general cases.

However, when both SNVs and CNAs data are provided, one can attempt at merging the events in a pre-processing phase. Consider for instance a mutation on a gene X acting as a tumour suppressor, and a chromosomal deletion spanning through the mutated gene (or a wider chromosomal region including it). If one can phase the deletion to the strand where X is mutated, a single-cell dataset could look as in Supplementary Figure 22. If there is a lineage relation between cells (samples 1–3 are ancestral to 4–6, which we do not know), and we merge the two distinct events before performing the inference, then we can retrieve a progression model where we time the event “inactivation of X”. In more general scenarios of aneuploidy, or when cells are siblings and the events are not phased, creating a merged events is not a solution to the back-mutation problem.

## References

- [1] Alexander Davis and Nicholas E Navin. Computing tumor trees from single cells. *Genome biology*, 17(1):113, 2016.

- [2] Katharina Jahn, Jack Kuipers, and Niko Beerenwinkel. Tree inference for single-cell data. *Genome biology*, 17(1):86, 2016.
- [3] Edith M Ross and Florian Markowetz. Onconem: inferring tumor evolution from single-cell sequencing data. *Genome biology*, 17(1):69, 2016.
- [4] Andrew Roth, Andrew McPherson, Emma Laks, Justina Biele, Damian Yap, Adrian Wan, Maia A Smith, Cydney B Nielsen, Jessica N McAlpine, Samuel Aparicio, et al. Clonal genotype and population structure inference from single-cell tumor sequencing. *Nature methods*, 13(7):573–576, 2016.
- [5] Loes Olde Loohuis, Giulio Caravagna, Alex Graudenzi, Daniele Ramazzotti, Giancarlo Mauri, Marco Antoniotti, and Bud Mishra. Inferring tree causal models of cancer progression with probability raising. *PloS one*, 9(10):e108358, 2014.
- [6] Daniele Ramazzotti, Giulio Caravagna, Loes Olde Loohuis, Alex Graudenzi, Ilya Korsunsky, Giancarlo Mauri, Marco Antoniotti, and Bud Mishra. Capri: efficient inference of cancer progression models from cross-sectional data. *Bioinformatics*, 31(18):3016–3026, 2015.
- [7] Giulio Caravagna, Alex Graudenzi, Daniele Ramazzotti, Rebeca Sanz-Pamplona, Luca De Sano, Giancarlo Mauri, Victor Moreno, Marco Antoniotti, and Bud Mishra. Algorithmic methods to infer the evolutionary trajectories in cancer progression. *Proceedings of the National Academy of Sciences*, page 201520213, 2016.
- [8] Daniele Ramazzotti. *A Model of Selective Advantage for the Efficient Inference of Cancer Clonal Evolution*. PhD thesis, arXiv preprint arXiv:1602.07614, 2017.
- [9] Daniele Ramazzotti, Marco S Nobile, Paolo Cazzaniga, Giancarlo Mauri, and Marco Antoniotti. Parallel implementation of efficient search schemes for the inference of cancer progression models. In *Computational Intelligence in Bioinformatics and Computational Biology (CIBCB), 2016 IEEE Conference on*, pages 1–6. IEEE, 2016.
- [10] Daniele Ramazzotti, Alex Graudenzi, Giulio Caravagna, and Marco Antoniotti. Modeling cumulative biological phenomena with suppes-bayes causal networks. *Evolutionary Bioinformatics*, 14:1176934318785167, 2018.
- [11] Daphne Koller and Nir Friedman. *Probabilistic graphical models: principles and techniques*. MIT press, 2009.
- [12] Patrick Suppes. *A probabilistic theory of causality*. North-Holland Publishing Company Amsterdam, 1970.
- [13] David JC MacKay. *Information theory, inference and learning algorithms*. Cambridge university press, 2003.
- [14] Mohammed El-Kebir, Layla Oesper, Hannah Acheson-Field, and Benjamin J Raphael. Reconstruction of clonal trees and tumor composition from multi-sample sequencing data. *Bioinformatics*, 31(12):i62–70, June 2015.
- [15] Victoria Popic, Raheleh Salari, Iman Hajirasouliha, Dorna Kashef-Haghighi, Robert B West, and Serafim Batzoglou. Fast and scalable inference of multi-sample cancer lineages. *Genome Biology*, 16(1):795–17, May 2015.

- [16] Jack Edmonds. Optimum branchings. *Journal of Research of the National Bureau of Standards B*, 71(4):233–240, 1967.
- [17] Robert Endre Tarjan. Finding optimum branchings. *Networks*, 7(1):25–35, 1977.
- [18] Robert Clay Prim. Shortest connection networks and some generalizations. *Bell Labs Technical Journal*, 36(6):1389–1401, 1957.
- [19] Harold N Gabow. Path-based depth-first search for strong and biconnected components. *Information Processing Letters*, 74(3-4):107–114, 2000.
- [20] C Chow and Cong Liu. Approximating discrete probability distributions with dependence trees. *IEEE transactions on Information Theory*, 14(3):462–467, 1968.
- [21] Barbara L Parsons. Many different tumor types have polyclonal tumor origin: evidence and implications. *Mutation Research/Reviews in Mutation Research*, 659(3):232–247, 2008.
- [22] Ke Yuan, Thomas Sakoparnig, Florian Markowetz, and Niko Beerenwinkel. Bitphylogeny: a probabilistic framework for reconstructing intra-tumor phylogenies. *Genome biology*, 16(1):36, 2015.
- [23] Yong Wang, Jill Waters, Marco L Leung, Anna Unruh, Whijae Roh, Xiuqing Shi, Ken Chen, Paul Scheet, Selina Vattathil, Han Liang, et al. Clonal evolution in breast cancer revealed by single nucleus genome sequencing. *Nature*, 512(7513):155–160, 2014.
- [24] You-Wang Lu, Hui-Feng Zhang, Rui Liang, Zhen-Rong Xie, Hua-You Luo, Yu-Jian Zeng, Yu Xu, La-Mei Wang, Xiang-Yang Kong, and Kun-Hua Wang. Colorectal cancer genetic heterogeneity delineated by multi-region sequencing. *PloS one*, 11(3):e0152673, 2016.

Error Rates		Specificity		Sensitivity	
$\epsilon_+$	$\epsilon_-$	Average	SD	Average	SD
0.003	0.07	0.984	0.020	0.729	0.172
0.004	0.07	0.984	0.020	0.725	0.179
0.005	0.07	0.985	0.020	0.730	0.176
0.006	0.07	0.984	0.020	0.723	0.179
0.007	0.07	0.984	0.020	0.724	0.175
0.003	0.06	0.984	0.020	0.729	0.172
0.004	0.06	0.984	0.020	0.725	0.179
0.005	0.06	0.985	0.020	0.730	0.176
0.006	0.06	0.984	0.020	0.725	0.178
0.007	0.06	0.984	0.020	0.726	0.175
0.003	0.05	0.984	0.020	0.729	0.172
0.004	0.05	0.984	0.020	0.725	0.179
0.005	0.05	0.985	0.020	0.730	0.176
0.006	0.05	0.985	0.020	0.727	0.178
0.007	0.05	0.984	0.020	0.726	0.175
0.003	0.04	0.984	0.020	0.729	0.172
0.004	0.04	0.984	0.020	0.726	0.178
0.005	0.04	0.985	0.020	0.730	0.176
0.006	0.04	0.985	0.020	0.727	0.178
0.007	0.04	0.984	0.020	0.726	0.175
0.003	0.03	0.984	0.020	0.729	0.172
0.004	0.03	0.984	0.020	0.726	0.178
0.005	0.03	0.985	0.020	0.730	0.176
0.006	0.03	0.985	0.020	0.727	0.178
0.007	0.03	0.984	0.020	0.726	0.175

Supplementary Table 4: Experiment IV. (noise-robustness). Average sensitivity and specificity (and standard deviation) of Gabow on datasets generated from the medium phylogenetic tree in Supplementary Figure 7, with  $\epsilon_+ = 5 \times 10^{-3}$  and  $\epsilon_- = 5 \times 10^{-2}$ . We test combinations of input for  $\epsilon_+$  and  $\epsilon_-$  in the following ranges:  $\epsilon_+ = (3, 4, 5, 6, 7) \times 10^{-3}$  and  $\epsilon_- = (3, 4, 5, 6, 7) \times 10^{-2}$ .

Error Rates		Specificity		Sensitivity	
$\epsilon_+$	$\epsilon_-$	Average	SD	Average	SD
0.003	0.07	0.959	0.030	0.708	0.181
0.004	0.07	0.958	0.032	0.696	0.202
0.005	0.07	0.960	0.029	0.702	0.188
0.006	0.07	0.962	0.027	0.709	0.175
0.007	0.07	0.958	0.031	0.693	0.197
0.003	0.06	0.959	0.030	0.699	0.180
0.004	0.06	0.957	0.032	0.692	0.203
0.005	0.06	0.962	0.028	0.707	0.182
0.006	0.06	0.959	0.030	0.696	0.190
0.007	0.06	0.958	0.030	0.691	0.198
0.003	0.05	0.957	0.029	0.696	0.174
0.004	0.05	0.955	0.032	0.686	0.201
0.005	0.05	0.962	0.027	0.710	0.181
0.006	0.05	0.960	0.029	0.698	0.183
0.007	0.05	0.958	0.031	0.682	0.207
0.003	0.04	0.956	0.029	0.698	0.183
0.004	0.04	0.954	0.031	0.680	0.203
0.005	0.04	0.962	0.027	0.718	0.177
0.006	0.04	0.960	0.030	0.701	0.187
0.007	0.04	0.958	0.030	0.684	0.194
0.003	0.03	0.956	0.029	0.691	0.195
0.004	0.03	0.956	0.030	0.693	0.192
0.005	0.03	0.960	0.027	0.703	0.184
0.006	0.03	0.961	0.028	0.703	0.179
0.007	0.03	0.956	0.031	0.672	0.195

Supplementary Table 5: Experiment IV. (noise-robustness). Average sensitivity and specificity (and standard deviation) of SCITE on datasets generated from the medium phylogenetic tree in Supplementary Figure 7, with  $\epsilon_+ = 5 \times 10^{-3}$  and  $\epsilon_- = 5 \times 10^{-2}$ . We test combinations of input for  $\epsilon_+$  and  $\epsilon_-$  in the following ranges:  $\epsilon_+ = (3, 4, 5, 6, 7) \times 10^{-3}$  and  $\epsilon_- = (3, 4, 5, 6, 7) \times 10^{-2}$ .



	Average execution time	Total execution time (100 experiments)
<b>CAPRESE</b>	0.03s	19.67s
<b>PRIM</b>	1.35s	150.12s
<b>GABOW</b>	1.36s	151.56s
<b>EDMONDS</b>	1.36s	152.30s
<b>CAPRI</b>	1.36s	153.70s
<b>CHOW-LIU</b>	1.39s	154.34s
<b>SCITE</b>	4.43s	505.70s
<b>OncoNEM</b>	59.23s	6037.22s

Supplementary Table 6: Average and total execution times for 100 distinct experiments, with the parameters described in Section 6.

<b>Sensitivity</b>				
<b>Sample Size (<math>m</math>)</b>	<b>CHOW-LIU</b>		<b>EDMONDS</b>	
	Median	St. Dev.	Median	St. Dev.
100	0.78	0.27	0.6	0.2
500	1	0.16	0.74	0.25
1000	1	0.07	0.89	0.15
5000	1	0.17	1	0.18
10000	1	0.14	1	0.14
15000	1	0.17	1	0.17
20000	1	0.22	1	0.22

<b>Specificity</b>				
<b>Sample Size (<math>m</math>)</b>	<b>CHOW-LIU</b>		<b>EDMONDS</b>	
	Median	St. Dev.	Median	St. Dev.
100	0.97	0.04	0.98	0.01
500	0.95	0.12	0.99	0.01
1000	0.96	0.12	0.99	0.01
5000	0.97	0.17	1	0
10000	0.98	0.13	1	0
15000	0.99	0.15	1	0
20000	0.98	0.14	1	0

<b>Computation time (sec)</b>				
<b>Sample Size (<math>m</math>)</b>	<b>CHOW-LIU</b>		<b>EDMONDS</b>	
	Median	St. Dev.	Median	St. Dev.
100	2.35	0.42	2.29	0.41
500	1.89	0.68	1.85	0.59
1000	2.21	1.34	2.19	0.82
5000	6.76	2.78	6.78	0.59
10000	12.22	2.54	12.43	0.94
15000	16.79	2.45	16.94	0.17
20000	22.08	2.61	22.24	0.21

Supplementary Table 7: Median sensitivity, specificity and computation time, along with the corresponding standard deviation, for CHOW-LIU and EDMONDS. We used 100 distinct experiments of SCS data, with the following parameter settings:  $n = 20$  nodes,  $\epsilon_+ = 0.005$ ,  $\epsilon_- = 0.05$ ,  $m \in (100, 500, 1000, 5000, 10000, 15000, 20000)$ .